

Electronic Thesis and Dissertation Repository

4-16-2014 12:00 AM

Biomechanical Modeling and Inverse Problem Based Elasticity Imaging for Prostate Cancer Diagnosis

Seyed Reza Mousavi, *The University of Western Ontario*

Supervisor: Dr. Abbas Samani, *The University of Western Ontario*

A thesis submitted in partial fulfillment of the requirements for the Doctor of Philosophy degree in Electrical and Computer Engineering

© Seyed Reza Mousavi 2014

Follow this and additional works at: <https://ir.lib.uwo.ca/etd>



Part of the [Biomedical Commons](#)

Recommended Citation

Mousavi, Seyed Reza, "Biomechanical Modeling and Inverse Problem Based Elasticity Imaging for Prostate Cancer Diagnosis" (2014). *Electronic Thesis and Dissertation Repository*. 1968.
<https://ir.lib.uwo.ca/etd/1968>

This Dissertation/Thesis is brought to you for free and open access by Scholarship@Western. It has been accepted for inclusion in Electronic Thesis and Dissertation Repository by an authorized administrator of Scholarship@Western. For more information, please contact wlsadmin@uwo.ca.

BIOMECHANICAL MODELING AND INVERSE PROBLEM BASED ELASTICITY IMAGING FOR PROSTATE CANCER DIAGNOSIS

(Thesis format: Integrated Article)

by

Seyed Reza Mousavi

Graduate Program
in
Electrical and Computer Engineering

A thesis submitted in partial fulfillment
of the requirements for the degree of
Doctor of Philosophy

The School of Graduate and Postdoctoral Studies
The University of Western Ontario
London, Ontario, Canada

© Seyed Reza Mousavi, 2014

Abstract

Early detection of prostate cancer plays an important role in successful prostate cancer treatment. This requires screening the prostate periodically after the age of 50. If screening tests lead to prostate cancer suspicion, prostate needle biopsy is administered which is still considered as the clinical gold standard for prostate cancer diagnosis. Given that needle biopsy is invasive and is associated with issues including discomfort and infection, it is desirable to develop a prostate cancer diagnosis system that has high sensitivity and specificity for early detection with a potential to improve needle biopsy outcome. Given the complexity and variability of prostate cancer pathologies, many research groups have been pursuing multi-parametric imaging approach as no single modality imaging technique has proven to be adequate. While imaging additional tissue properties increases the chance of reliable prostate cancer detection and diagnosis, selecting an additional property needs to be done carefully by considering clinical acceptability and cost. Clinical acceptability entails ease with respect to both operating by the radiologist and patient comfort. In this work, effective tissue biomechanics based diagnostic techniques are proposed for prostate cancer assessment with the aim of early detection and minimizing the number of prostate biopsies. The techniques take advantage of the low cost, widely available and well established Transrectal Ultrasonography (TRUS). The proposed techniques include novel elastography methods which were formulated based on an inverse finite element frame work. Conventional finite element analysis is known to have high computational complexity, hence computation time demanding. This renders the proposed elastography methods not suitable for real-time applications. To address this issue, an accelerated finite element method was proposed which proved to be suitable for prostate elasticity reconstruction. In this method, accurate finite element analysis of a large number of prostates undergoing TRUS probe loadings was performed. Geometry input and displacement and stress fields output obtained from the analysis were used to train a neural network mapping function to be used for elastography imaging of prostate cancer patients. The last part of the research presented in this thesis addresses an issue with the current 3D TRUS prostate needle biopsy. Current 3D TRUS prostate needle biopsy systems require registering preoperative 3D TRUS to intra-operative 2D TRUS images. Such image registration is time-consuming while its real-time implementation is yet to be developed. To bypass this registration step, a robotic system was

proposed which can reliably determine the preoperative TRUS probe position relative to the prostate to place at the same position relative to the prostate intra-operatively. For this purpose, a contact pressure feedback system is proposed to ensure similar prostate deformation during 3D and 2D image acquisition in order to bypass the registration step.

Keywords

Prostate Cancer, Early Detection, Diagnosis, Transrectal Ultrasonography, Elastography, Full Inversion, Finite Element Modeling, Iterative Method, Statistical Finite Element Modeling, Prostate Needle Biopsy, Ultrasound Image Registration, Pressure Sensor, Pressure Feedback, Optimization

Co-Authorship Statement

This thesis has been written by Seyed Reza Mousavi under supervision of Dr. Abbas Samani. Parts of the material presented in this thesis have been published in peer-reviewed journal papers as listed below. The research presented in each publication has been conducted by the principal author and guided/supported by or in collaboration with the underlined authors who are the research supervisor or members of the collaborative research projects.

The material presented in Chapter 2 has been submitted to: S. R. Mousavi, H. Wang and A. Samani, “A Fast Shape-Similarity-Based Ultrasound Elastography Technique for Prostate Cancer Assessment,” *Computer Methods in Biomechanics and Biomedical Engineering*.

The material presented in Chapter 3 has been published in: S. R. Mousavi, A. Sadeghi Naini, G. Czarnota and A. Samani, “Towards Clinical Prostate Ultrasound Elastography Using Full Inversion Approach,” *Journal of Medical Physics*, vol. 41, no. 3, 033501, 2014.

The material presented in Chapter 4 has been published in: S. R. Mousavi, I. Khalaji , A. Sadeghi Naini, K. Raahemifar and A. Samani., “Statistical finite element method for real-time tissue mechanics analysis,” *Computer Methods in Biomechanics and Biomedical Engineering*, vol.15, issue 6, pp. 595-608, 2011.

The material presented in Chapter 5 has been published in: S. R. Mousavi, K. Raahemifar, S. Pautler and A. Samani, “Towards ultrasound probe positioning optimization during prostate needle biopsy using pressure feedback,” *International Journal of Computer Assisted Radiology and Surgery*, vol. 8, issue 6, pp. 1053-1061, 2013.

Dedication

**This thesis is dedicated to my loving wife, parents and my sister
and brother**

for their endless love, support and encouragement

Acknowledgments

I would like to gratefully appreciate my supervisor Dr. Abbas Samani for his guidance, support criticisms, and dedication to research. He has been my mentor both in research and in life.

I would also like to thank Dr. Aaron Fenster, Dr. Aaron Ward, Dr. Hanif Ladak and Dr. Stephen Pautler for being supportive during my research.

Finally, I would like to thank my colleagues at Dr. Samani's Lab for helping me with my work and providing a friendly atmosphere to work in during past years.

Funding for this work was provided by the University of Western Ontario, Natural Sciences and Engineering Research Council of Canada and by Ontario Graduate Scholarship (OGS).

Table of Contents

Abstract	ii
Co-Authorship Statement	iv
Dedication	v
Acknowledgments	vi
Table of Contents	vii
List of Tables	x
List of Figures	xiii
List of Acronyms and Abbreviations	xvii
List of Appendices	xviii
Chapter 1	1
1 Introduction	1
1.1 Background and Motivation	1
1.1.1 Prostate Cancer	1
1.1.2 Prostate Cancer Detection.....	1
1.1.3 Prostate Cancer Treatment.....	3
1.2 Literature Review.....	3
1.2.1 Transrectal Ultrasonography (TRUS).....	4
1.2.2 Magnetic Resonance (MR) Imaging.....	4
1.2.3 Positron Emission Tomography (PET).....	5
1.2.4 Elastography	6
1.3 Objectives	7
1.4 Thesis Outline	8
1.4.1 Chapter 2.....	8
1.4.2 Chapter 3.....	9
1.4.3 Chapter 4.....	9
1.4.4 Chapter 5.....	10
1.4.5 Chapter 6.....	10
References	10
Chapter 2	15
2 A Fast Shape-Similarity-Based Ultrasound Elastography Technique for Prostate Cancer Diagnosis	15
2.1 Introduction.....	15
2.2 Method	18
2.2.1 <i>In Silico</i> Phantom Study.....	19
2.2.2 Tissue Mimicking Phantom Study.....	21
2.2.3 Finite Element Modeling	22
2.2.4 Young's Modulus Reconstruction.....	23
2.3 Results.....	25
2.3.1 <i>In Silico</i> Phantom Study.....	25

2.3.2 Tissue Mimicking Phantom Study.....	31
2.4 Discussion and Conclusions	32
References	35
Chapter 3	38
3 Towards Clinical Prostate Ultrasound Elastography Using Full Inversion Approach	38
3.1 Introduction.....	38
3.2 Methodology.....	42
3.2.1 Unconstrained Modulus Reconstruction Algorithm	42
3.2.2 Strain Measurement	45
3.2.3 Finite Element Modeling	46
3.2.4 <i>In Silico</i> Phantom Study.....	48
3.2.5 Tissue Mimicking Phantom Study.....	49
3.2.6 Clinical Study.....	50
3.3 Results.....	51
3.3.1 <i>In Silico</i> Phantom Study.....	51
3.3.2 Tissue Mimicking Phantom Study.....	52
3.3.3 Patient Study	55
3.4 Discussion and Conclusions	58
Appendix	61
References	63
Chapter 4	67
4 Statistical Finite Element Method for Real-Time Tissue Mechanics Analysis	67
4.1 Introduction.....	67
4.2 Methodology.....	70
4.2.1 Prostate Model	70
4.2.2 Statistical Shape Model.....	71
4.2.3 Statistical Finite Element Model.....	73
4.2.4 Formulation.....	73
4.2.5 Procedure	76
4.2.6 Fitting Function Approaches.....	77
4.3 Results.....	79
4.3.1 Dataset.....	80
4.3.2 SFEM Evaluation.....	80
4.4 Discussion and Conclusions	89
References	92
Chapter 5	95
5 Towards Ultrasound Probe Positioning Optimization During Prostate Needle Biopsy Using Pressure Feedback	95
5.1 Introduction.....	95
5.2 Methods.....	98
5.2.1 Modeling.....	99

5.2.2	Pressure Pattern Extraction	100
5.2.3	Optimization	102
5.3	Results	103
5.4	Discussion and Conclusions	109
	References	111
	Chapter 6	113
6	Conclusions and Future Work	113
6.1	Conclusions	113
6.1.1	Chapter 2: A Fast Shape-Similarity-Based Ultrasound Elastography Technique for Prostate Cancer Assessment	114
6.1.2	Chapter 3: Towards Clinical Prostate Ultrasound Elastography Using Full Inversion Approach	114
6.1.3	Chapter 4: Statistical finite element method for real-time tissue mechanics analysis	115
6.1.4	Chapter 5: Towards ultrasound probe positioning optimization during prostate needle biopsy using pressure feedback	116
6.2	Future Directions	117
6.3	Closing Remarks	119
	Appendices	120
7	Curriculum Vitae	123

List of Tables

Table 2-1: Reconstruction results of the phantom study using FEM where segmentation errors are not considered.	26
Table 2-2: Reconstruction results of the phantom study using FEM where segmentation errors are considered.	26
Table 2-3: Reconstruction results of the phantom study using SFEM where segmentation errors are not considered.	27
Table 2-4: Reconstruction results of the phantom study using SFEM where segmentation errors are considered.	28
Table 2-5: Reconstruction results of the proposed phantom study using SFEM for different weight factors where segmentation errors are not considered.	29
Table 2-6: Reconstruction results of the proposed phantom study using SFEM for different weight factors where segmentation errors are considered.	30
Table 2-7: Elasticity ratios and errors for shape similarity-based elastography method	33
Table 3-1: Amounts of different materials used for constructing different regions of the unifocal phantom.	50
Table 3-2: Amounts of different materials used for constructing different regions of the bifocal phantom.	50
Table 3-3: Reconstructed YM ratio values of the <i>in silico</i> phantom (noise free case).	51
Table 3-4: YM ratio values of the <i>in silico</i> phantom reconstructed from strain data with SNR of 10 dB.....	52
Table 3-5: Reconstructed YM ratio values of unifocal tissue mimicking phantom	53
Table 3-6: Reconstructed YM ratio values of bifocal tissue mimicking phantom	55

Table App-1: Reconstructed YM ratio values of unifocal tissue mimicking phantom for different probe compression values.	61
Table App-2: Reconstructed YM ratio values of bifocal tissue mimicking phantom for different probe compression values.	62
Table App-3: Reconstructed YM ratio values of clinical study # 1 for different probe compression values.	62
Table App-4: Reconstructed YM ratio values of clinical study # 2 for different probe compression values.	62
Table 4-1: Mean and max average of values of u_x errors per node for 100 shape evaluation data.	82
Table 4-2: Mean and max average of values of u_y errors per node for 100 shape evaluation data.	83
Table 4-3: Mean and max average of values of σ_{xx} errors per node for 100 shape evaluation data.	83
Table 4-4: Mean and max average of values of σ_{yy} errors per node for 100 shape evaluation data.	84
Table 4-5: The ratio of the processing time of ABAQUS to the processing time of SFEM. .	89
Table 5-1: Results of the proposed method for case 1 of the second experiments set where the phantom was moved 5mm along y direction.	105
Table 5-2: Results of the proposed method for case 2 of the second experiments set where the phantom was moved 5 mm along z direction.	106
Table 5-3: Results of the proposed method for case 3 of the second experiments set where the phantom was rotated 5° around the x axis.	107

Table 5-4: Results of the proposed method for case 4 of the second experiments where the phantom was moved 5mm along both the y and z directions and rotated 5° around the x axis.
..... 108

List of Figures

Figure 2-1: Flow chart of the proposed elastography method which requires the prostate B-mode images acquired at two states of pre- and post-compression as input for the elasticity reconstruction.....	19
Figure 2-2: Four phantom cases with simulated segmentation errors. The dashed lines represent the true outlines and the solid lines indicate the ones with segmentation errors. ...	20
Figure 2-3: Pre-compression (left) and post-compression (right) cancerous prostate FE model. White arrow shows the direction of the US probe contact loading (E_s , E_p and E_t represent YM values assigned to the surrounding tissue, the prostate and the tumor respectively. Also, d_l and θ represent displacement amount and its direction)	22
Figure 2-4: A typical optimization trend of the elastography reconstruction method with conventional FEM.....	24
Figure 2-5: Segmented prostate (blue) and tumor (red) outlines of pre-compression (left) and post-compression (right) prostate 2D TRUS images (The depth of the fan in the images is 7 cm).	31
Figure 3-1: Typical B-mode image of a prostate cancer patient (the hypo-echoic area shows the tumor) (a), finite element model used for constrained elastography (b), and uniform meshing with 5×5 elements processing windows used for unconstrained iterative elastography (c). A 5×5 window is magnified and shown separately.	44
Figure 3-2: Flow chart illustrating the unconstrained iterative procedure for YM reconstruction.....	45
Figure 3-3: Anatomical transverse view of the prostate restricted anteriorly by the pubic bone (taken from [33]) (a) and finite element model with radially restricted points on top boundary (b).....	47
Figure 3-4: <i>In silico</i> prostate-tumor phantom (a) and corresponding FE mesh created to generate strain image data (b).	48

Figure 3-5: Tissue mimicking unifocal (left) and bifocal (right) phantoms consisting of prostate, tumor (indicated with white arrows), and surrounding tissues. 49

Figure 3-6: Reconstructed Young’s modulus image using data with no noise (a) and reconstructed elasticity image using strain field with SNR of 10 dB (b) (The size of the rectangle is 10×8 cm)..... 52

Figure 3-7: B-mode ultrasound image of the tissue mimicking phantom (top), corresponding strain image (middle), and reconstructed elasticity image using the proposed elastography technique (bottom). The tumor area has been roughly segmented based on the B-mode image on the strain and YM images. (The depth of the fan in all images is 7 cm) 53

Figure 3-8: B-mode ultrasound image of the bifocal tissue mimicking phantom (top), corresponding strain image (middle), and elasticity image reconstructed using the proposed elastography technique (bottom). The tumor areas have been roughly segmented based on the B-mode image on the strain and YM images. (The depth of the fan in all images is 5 cm) .. 54

Figure 3-9: Macroscopic image of the whole-mount histopathology section of the prostatectomy specimen acquired from patient 1 (a), demonstrating the cancerous areas contoured by a pathologist. The scale bar is ~ 1 cm. B-mode ultrasound image (b), clinical strain image (c), calculated strain image (d), and reconstructed YM image corresponding to patient 1 (e). Prostate cancer is visible as a hypo-intensity area in the reconstructed strain image and as two nodules in the reconstructed YM image (contoured in white). (The depth of the fan in all images is 4 cm) 56

Figure 3-10: Macroscopic image of the whole-mount histopathology section of the prostatectomy specimen acquired from patient 2 (a), demonstrating the cancerous area contoured by a pathologist. The scale bar is ~ 1 cm. B-mode ultrasound image (b), clinical strain image (c), calculated strain image (d) and reconstructed YM image (e) corresponding to patient 2. The hypo-intensity area in the reconstructed strain image shows a single outlined tumor region. A distinct suspicious outlined area is visible in the reconstructed YM image that fits the cancerous region of the histology image. (The depth of the fan is 5cm in B-mode image and 6 cm in clinical and calculated strain images and the reconstructed YM image) . 57

Figure 4-1: Prostate 2D TRUS images (a) before compression and (b) after compression and (c) corresponding FE model of the prostate with contact loading of US probe and fixed boundary conditions. Outline boundaries far enough from the US probe are idealized as fixed boundary conditions.....	71
Figure 4-2: Displacements average errors of 100 shape evaluation data-sets (using 400 training set) corresponding to FE results of (a) u_x for type A, (b) u_x for type D, (c) u_y for type A and (d) u_y for type D (errors are in %).	81
Figure 4-3: Stress average error of 100 shape evaluation data-sets (using 400 training sets) corresponding to FE results of (a) σ_{xx} for type A, (b) σ_{xx} for type D, (c) σ_{yy} for type A and (d) σ_{yy} for type D (errors are in %)..	82
Figure 4-4: u_x field of FEM, NN and PCA and their differences for analysis type D (values of color bar are in mm).....	85
Figure 4-5: u_y field of FEM, NN and PCA and their differences for analysis type D (values of color bar are in mm).....	86
Figure 4-6: σ_{xx} field of FEM, NN and PCA and their differences for analysis type D (values of color bar are in kPa).....	87
Figure 4-7: σ_{yy} field of FEM, NN and PCA and their differences for analysis type D (values of color bar are in kPa).....	88
Figure 5-1: An array of tactile sensors is placed around the surface area of the US transducer array for pressure feedback acquisition (a design study).....	98
Figure 5-2: Flow chart of the proposed method: optimization of TRUS probe orientation during needle biopsy using pressure robotic feedback.	99
Figure 5-3: Segmented prostate border in a radial slice of 3D prostate MR image (a), fitted surface obtained by segmenting 12 radial slices of the prostate (b), and 3D slicer point expression of the prostate fitted surface (c).	100

Figure 5-4: Different views of the prostate finite element model mimicking the prostate TRUS imaging: the whole model (a), the model in wireframe view in which the prostate is shown in red (b), and the model without the surrounding tissue (block) to show the prostate embedded in the block behind the rectal wall (c). 101

Figure 5-5: Pressure on the rectal wall resulting from probe stimulation with the area in contact with tactile sensors of the US probe (red box) containing 27×12 elements (a), and the pressure pattern from concatenating the pressure values of the tactile sensor elements around the US 2D array (74 elements within black boxes starting from black dot) (b). 102

Figure 5-6: Pressure patterns resulting from US probe displacements of 0.5, 1, 1.5, and 2 mm in the P-A direction. 104

Figure 5-7: Case 1 displacement difference of the prostate surface nodes before prostate motion compensation (dotted blue line) and after prostate motion compensation (solid red line). 106

Figure 5-8: Case 2 displacement difference of the prostate surface nodes before prostate motion compensation (dotted blue line) and after prostate motion compensation (solid red line). 107

Figure 5-9: Case 3 displacement difference of the prostate surface nodes before prostate motion compensation (dotted blue line) and after prostate motion compensation (solid red line). 108

Figure 5-10: Case 4 displacement difference of the prostate surface nodes before prostate motion compensation (dotted blue line) and after prostate motion compensation (solid red line). 109

List of Acronyms and Abbreviations

AAPM	Association of Physicists in Medicine
ANN	Artificial Neural Network
BPH	Benign Prostatic Hyperplasia
CEUS	Contrast-Enhanced Ultrasound
DCE	Dynamic Contrast-Enhanced
DDC	Discrete Dynamic Contour
DRE	Digital Rectal Examination
DWI	Diffusion-Weighted Imaging
FEM	Finite Element Modeling (Method)
GPU	Graphics Processing Unit
HIFU	High Intensity Focused Ultrasound
LSE	Least Squares Error
MRI	Magnetic Resonance Imaging
MRSI	Magnetic Resonance Spectroscopy Imaging
MS	Mass-Spring
PCA	Principal Component Analysis
PSA	Prostate Specific Antigen
RF	Radio Frequency
RB	Reduced Basis
SFEM	Statistical FEM
SSM	Statistical Shape Model
STD	Standard Deviation
TFI	Transfinite Interpolation
TRUS	Transrectal Ultrasonography
US	Ultrasound
VR	Virtual Reality

List of Appendices

Appendix 1: Permission to reproduce paper, which has been published under AAMP copyright, in this thesis.	120
Appendix 2: Permission to reproduce paper, which has been published under the Taylor & Francis copyright, in this thesis.	121
Appendix 3: Permission to reproduce paper, which has been published under the Springer copyright, in this thesis.	122

Chapter 1

Introduction

1.1 Background and Motivation

1.1.1 Prostate Cancer

Prostate cancer is the most frequently diagnosed cancer in Canadian males, and is the third most common cause of death due to cancer in men (after lung and colorectal cancer) [1]. 25% of all new cancer cases in Canadian men are prostate cancer cases (an estimate of 23,600 men in 2013) and 10% of all cancer deaths are because of prostate cancer (approximately 3,900 men in 2013). On average, 65 Canadian men will be diagnosed with prostate cancer every day and 11 will die from prostate cancer every day [1]. Similar to other types of cancer, early detection plays a vital role in successful prostate cancer treatment. Studies have shown that the 5-year survival rate of prostate cancer associated with early diagnosis is almost 99% while this rate falls sharply to less than 28% for patients with late diagnosis [2].

1.1.2 Prostate Cancer Detection

Early detection of prostate cancer requires screening the prostate periodically after the age of 50. Hence, a low cost and accurate screening method is highly desirable. The two conventional prostate cancer screening and detection techniques which are the earliest and least invasive tests for prostate cancer detection are Prostate-Specific Antigen (PSA)

blood test and Digital Rectal Examination (DRE). If significant elevation of PSA level is detected or the DRE test is deemed positive, prostate cancer is suspected and the patient is usually sent for needle biopsy where definitive diagnosis of prostate cancer is made. While the PSA blood test has a fairly high sensitivity of ~80%, nearly 70% of findings are false positives [3-7]. The low specificity of the PSA test is because a number of other conditions can cause a man's PSA level to rise such as prostatitis (inflammation of the prostate), urinary tract infection and benign prostatic hyperplasia (BPH) (enlargement of the prostate). Compared to PSA, the DRE test has a considerable higher specificity of ~80% but a low sensitivity of ~50% [4-8]. The low sensitivity of DRE test is mostly because it is a qualitative test. In some cases the tumor is too far from the palpating finger to be sensed and in some cases malignant tumors are not much stiffer than the surrounding tissue. Furthermore, this method suffers from another drawback, which is inter-observer and intra-observer variability. Results of a DRE performed on a patient may differ from one physician to another. The two methods have very low positive predictive value of ~20% [3-8]. Although the two methods are low-cost but they are not accurate enough.

The prostate needle biopsy is considered as the current clinical gold standard for prostate cancer diagnosis. Prostate needle biopsy is administered if the PSA and or DRE tests lead to prostate cancer suspicion [9]. It involves removing representative samples of the gland to determine the degree and extent of prostate cancer [10]. Transrectal Ultrasound (TRUS) which is the most commonly used urologic imaging modality is currently utilized for needle guidance during prostate biopsy. Although TRUS-guided prostate biopsy is a real-time, relatively low cost and easy to use procedure, it only provides limited amount of information to the physician for accurately guiding the needles to suspicious locations within the prostate capsule, leading to low sensitivity of ~60% and very low positive predictive value of only ~25% [11]. This issue leads to excessive number of biopsies that is undesirable since prostate biopsies are associated with discomfort in addition to a number of side effects such as hematuria (blood in urine), hematospermia (blood in semen), rectal bleeding, and infection. Therefore, reducing the number of biopsies is of great interest which requires better localization of the tumors and more accurate conducting the needle biopsy.

1.1.3 Prostate Cancer Treatment

Prostate cancer staging plays an important role in the selection of an optimal approach to treatment. For instance, preferred treatment for organ-confined prostate cancer is different from the one for the cancer spread outside the prostate. Also, in some situations, expectant management is the preferred choice which is an option for patients with small-volume and low-risk prostate cancer [12]. The most common systematic staging system is known as the TNM system developed by the American Joint Committee on Cancer. It is based on the evaluation of the size of the tumor (T), the extent of involved lymph nodes (N), any metastasis or distant spread (M) and also cancer grading. Prostate cancer grading is done using the Gleason Grading System in which a Gleason score is given to prostate cancer based on the microscopic pattern of biopsy samples. Cancers with a higher Gleason score are more aggressive and have a worse prognosis. Prostate cancer cases are grouped into four overall stages using grade information in conjunction with TNM status. Once again, accurate detection and localization of the prostate cancer is essential for a successful staging that is a prerequisite for optimal clinical management and therapy selection.

Based on diagnosis and staging results, there are several treatment methods for prostate cancer. Radical treatments (such as prostatectomy and chemotherapy) are suggested for the advanced extra-prostatic cases (Stages III and IV) and there are local and minimally invasive treatment options for organ-confined disease (Stages I and II) including cryoablation, brachytherapy and high-intensity focused ultrasound (HIFU) [13]. These local therapies however require exact localization of the cancer.

1.2 Literature Review

Anatomic, functional, and molecular imaging modalities allow for improved detection and characterization of prostate cancer. Based on the challenges mentioned in the previous sections, imaging might be able to contribute to improving diagnostic accuracy, improving biopsy representation of underlying disease, accurately determining staging and better focal therapy. Imaging can also be used for monitoring purposes, either monitoring disease progression or assessing the response to therapy [14]. In this section,

we will review the more established imaging techniques and briefly discuss the pros and cons of each.

1.2.1 Transrectal Ultrasonography (TRUS)

Since, ultrasound images in real-time, TRUS is the most commonly used modality for guiding needle biopsy. But its ability to detect and localize prostate cancer is limited. Although, prostate cancers typically appear hypoechoic on TRUS, most hypoechoic lesions found on TRUS are not cancer and many cancer cases are not hypoechoic [15, 16]. In an attempt to increase the sensitivity and specificity of TRUS, contrast-enhanced TRUS (CEUS) has been developed. CEUS is a method of measuring the vascularisation using micro-bubbles as the contrast agent. Recent studies in correlating CEUS and histopathological prostate images showed that CEUS is a promising technique for tumor localization [17]. However, the sensitivity and specificity of CEUS are still not high enough to replace prostate biopsies. Another new method based on TRUS is Computer-Aided TRUS or the so-called HistoScanning method. It is based on extracting the texture information of the TRUS image for prostate cancer detection. Although developers believe it is an inexpensive method for localizing tumors and also identifying multifocality, bilaterality, and extraprostatic extension, the method is not well validated clinically [18].

In summary, TRUS improves the accuracy of prostate cancer detection in comparison to the conventional methods and is a widely available and low cost imaging system. But it still does not have enough accuracy for localization and staging purposes.

1.2.2 Magnetic Resonance (MR) Imaging

MR is an evolving modality in prostate cancer assessment. The most established MR imaging is the standard T2-weighted MR imaging and there is ongoing research to identify its potential in prostate cancer detection, staging and conducting needle biopsy. T2-weighted MRI has a good sensitivity but low specificity [19-21] and the method is not capable of detecting cancer in the transitional zone of the prostate accurately. Also the method suffers from significant intra-observer variability for detecting prostate cancer. For staging purposes, although T2-weighted MRI is one of the most accurate imaging

modalities for detecting metastases, it has low sensitivity in detecting extra-capsular extension [22, 23]. Detection and staging performance of MR imaging was improved in part by developments in technology. Development of endorectal coils has improved the accuracy for local staging by improving signal-to-noise ratio and quality of the MR images. Other advances in MR imaging achieved by the development of functional and physiologic MR imaging techniques. Usually, these new techniques are used together in a multi-parametric approach [24]. Among these new techniques, MR spectroscopy imaging (MRSI), Dynamic Contrast-Enhanced MRI (DCE-MRI) and Diffusion-weighted imaging (DWI) are the most commonly used ones. MRSI analyzes the metabolic profile of each region within the prostate or more specifically reveals the concentration of biochemical disease marker in tissues (such as choline increase and citrate decrease) [25]. DCE-MRI on the other hand detects the alterations in the microvasculature resulting from tumor angiogenesis by monitoring the uptake of intravenously-administered gadolinium-based contrast agents [26]. In DWI, the diffusion of water in intracellular space as well as the extracellular matrix is measured which in return gives information about membrane permeability and cellular density, which may be altered in cancerous tissue [27]. Using all of these images in the framework of multi-parametric MRI (mp-MRI) improves tumor detection (especially in the transitional zone), localization and specification.

The use of MRI to conduct prostate needle biopsies is also under investigation and development [28, 29]. Although being conducted successfully, MRI-guided prostate biopsy is reported to be time-consuming, susceptible to prostate movement and moreover requiring specific equipment [28].

In conclusion, mp-MR imaging potentially provides the highest accuracy in the diagnosis and staging of prostate cancer. However more clinical trials should be done to make it clinically acceptable and to reach unified clinical protocols. Moreover, MR imaging is costly and not widely accessible the entire world.

1.2.3 Positron Emission Tomography (PET)

Another imaging modality that is recently used for prostate cancer assessment is positron emission tomography (PET). Since prostate cancer has a high metabolic rate that

consumes more glucose than normal cells, it can be detected by tracking glucose consumption. PET uses a radio-labeled glucose as a tracer to measure the metabolic rate in order to identify cancerous regions within the prostate. Earlier studies showed that PET has limited sensitivity and specificity for prostate cancer detection [30, 31]. However, PET is reported to be potentially useful for staging of prostate cancer by predicting nodal metastases and detecting recurring disease after primary therapy for prostate cancer [32, 33].

Capabilities of PET in prostate cancer assessment are still under investigation and several groups are examining new tracers to improve its accuracy for prostate cancer detection. Image resolution of PET images is still poor (> 5 mm) and it is suggested PET to be used in combination to other image modalities.

1.2.4 Elastography

Elastography or elasticity imaging is an imaging method utilizes local tissue stiffening as a contrast mechanism. The method has being used clinically for diagnosis purposes noting the fact that tissue stiffness alteration is associated with pathology [34, 35]. In case of prostate, cancer alters the stiffness of the prostate tissue in different ways. Containing too much DNA, nucleus of a cancerous cell is much larger and denser than nucleus of a normal cell [36]. Besides the cancerous cell itself, tumor stroma is also different than the stroma in normal tissue. This alteration is because of the reaction of normal stromal to cancerous cells in a process similar to the general wound repair pathway. In response, a new stromal environment is created which facilitates growth of cancerous cells by supporting cancer cell survival, proliferation and migration, and by inducing angiogenesis [37]. Changes in the components of the stroma (more collagen fibres and fibroblasts switching to myofibroblasts), extracellular matrix reorientation and elevated angiogenesis manifest as stiffer tissue [37]. The correlation between cancer and stiffness was also demonstrated by stiffness measurement studies of *ex vivo* prostate tissues [38, 39].

As such, elastography techniques were developed where tissue elasticity modulus are reconstructed and displayed. Several groups used the elastography concept to develop elasticity imaging techniques for prostate cancer detection and staging ([40], [41], [42])

and for conducting targeted prostate biopsy [43, 44]. Elastography is however based on strain imaging where tissue strain images are generated to approximate the tissue elastic modulus distribution. While strain images can be generated in real-time, they lack the necessary sensitivity and specificity. They are also not suitable for tumor localization. To improve strain imaging, full inversion based elastography techniques were proposed [45]. These techniques provide a better elasticity map for tumor localization and the fact that they are quantitative images can potentially help for prostate cancer staging. One of the reasons that full inversion elastography techniques have not been routinely used in the clinic is that often these algorithms are time-consuming and cannot provide real-time images similar to strain imaging. Any attempt to accelerate these techniques to make them at least near real-time may help them be clinically more acceptable. The other reason is the lack of clinical validation studies. To our knowledge, very few full inversion-based prostate elastography techniques have been applied *in vivo* before.

As a conclusion, elastography can improve prostate cancer early detection and classification as a low cost, widely available technique. However, more clinical validation studies are required to have elastography routinely used in the clinic.

1.3 Objectives

The objective of this work is to develop effective biomechanical methods for prostate cancer assessment with the aim of prostate cancer early detection and minimizing the numbers of prostate biopsy. As described earlier, based on a single detection method or imaging technique alone, the best clinical management of prostate cancer cannot be achieved. Each technique reveals certain aspects of the disease and it would be ideal to use as many techniques as possible to be able to decide about the best prostate cancer treatment strategy. However, reasonably inexpensive techniques and those do not disrupt the clinical flow appreciably are more desirable to contribute then. By clinically acceptable we mean the method does not require very complex peripheral devices that are not convenient for both physicians and patients. Towards this goal, we developed techniques that take advantage of the low cost, widely available and well established TRUS imaging method to improve patient income without introducing additional complexity and inconveniency.

The first part of the work includes two full inversion based elastography methods that improve prostate cancer imaging specificity. A major drawback of full inversion based elastography algorithms is that they are computationally intensive and not easy to implement. The proposed methods tackle this issue and reduce the complexity of the inversion algorithms for elastography.

The proposed inversion algorithms are time-consuming because of the reasons discussed later in this thesis and therefore not suitable for real-time purposes. In an attempt to accelerate the constrained elastography method, an statistical finite element method was proposed that is the next part of this work.

The last part of our work is to address an issue with the current 3D TRUS prostate needle biopsy. This system is newly developed for conducting a more successful prostate needle biopsy with a lower number of removed samples. 3D TRUS prostate needle biopsy requires registering preoperative 3D TRUS to intra-operative 2D TRUS images. Such image registration is time-consuming while its real-time implementation is yet to be developed. To bypass this registration step, the system includes a robotic structure that places the US probe at the same position relative to the prostate during the 3D and 2D image acquisition to ensure similar prostate deformation. To have such similar deformation, only visual feedback is not sufficient as such feedback can be used to only guarantee that the whole prostate is within the field of view irrespective of the probe's orientation. As such, a contact pressure feedback system was proposed to resolve this issue.

1.4 Thesis Outline

The thesis objective defined above has been presented in 4 separate chapters followed by a finalizing chapter where a thesis summary and future works are discussed. The outline of each chapter is as follows.

1.4.1 Chapter 2

In Chapter 2, a constrained full inversion elastography method is introduced. The algorithm uses the TRUS probe for mechanical stimulation of the prostate. The acquired

data during palpation are then used in a full inversion algorithm to reconstruct the true elasticity values of the normal and cancerous prostate tissue. This full inversion algorithm requires calculating the stress distribution as a result of palpation. The stress calculation was done using a finite element method (FEM). This technique utilizes pre-compression and post-compression US images for elasticity reconstruction and requires extracting the geometry of the prostate and cancerous regions. Hence it is called constrained. The method was validated with *in silico* and tissue mimicking phantom study and the obtained results indicated a favorable ability of the proposed technique for tumor classification as average error is less than 15%.

1.4.2 Chapter 3

An unconstrained US elastography is proposed in Chapter 3. This method utilizes pre-compression and post-compression Radio Frequency (RF) data. RF data are used to calculate displacement field during palpation which adds more information for elasticity reconstruction and makes the technique more robust. It is also unconstrained in terms of requiring information about geometries. In addition to *in silico* and tissue mimicking phantom study, the proposed method was applied to clinical prostate data and reconstructed elasticity images were compared to corresponding annotated histology images, which demonstrated a good potential for its clinical utility as the cancerous regions detected in reconstructed images have more than 80% overlap with their correspondents in histology images. To our knowledge, the proposed technique is the first quasi-static full inversion based prostate US elastography technique applied and validated successfully *in vivo*.

1.4.3 Chapter 4

In order to accelerate FE analysis for near real-time data processing, a novel tissue mechanics simulation technique is introduced in Chapter 4. This technique can speed up the proposed constrained elastography method. In this method, principal component analysis is used to describe each organ shape and its corresponding mechanical response for a pool of patients by a small number of weight factors. A mapping function is developed to relate the parameters of organ shape to their mechanical response

counterpart. We show that irrespective of the complexity of the tissue's constitutive law or its loading conditions, the proposed technique is highly accurate and fast in estimating the mechanical response.

1.4.4 Chapter 5

Chapter 5 introduces a conceptual add-on system to the current clinical 3D US prostate needle biopsy. The system requires adding a pressure sensor array to the ordinary TRUS probe. The contact pressure can then be measured during imaging and used to provide feedback in conjunction with an optimization algorithm for consistent probe positioning. The system is driven by the feed-back to position the probe such that pressure pattern of the sensors during 2D image acquisition is similar to the pressure pattern during 3D image acquisition to accelerate the registration process. This idea was validated with an *in silico* phantom study where the simulated contact pressure distribution required in the optimization algorithm is obtained using a prostate FE model.

1.4.5 Chapter 6

This Chapter summarizes the material presented in chapters 2 through 5. It also suggests possible future directions for the research described in the thesis and finally concludes this dissertation.

References

- [1] Canadian Cancer Society: www.cancer.ca. Accessed April 18, 2014.
- [2] American Cancer Society: www.cancer.org. Accessed April 18, 2014.
- [3] R. Etzioni, D. F. Penson, J. M. Legler, D. di Tommaso, R. Boer, P. H. Gann, and E. J. Feuer, "Overdiagnosis due to prostate-specific antigen screening: Lessons from U.S. prostate cancer incidence trends," *J. Natl. Cancer Inst.*, vol. 94, no. 13, pp. 981-990, 2002.
- [4] S. Weinmann, K. E. Richert-Boe, S. K. Van Den Eeden, S. M. Enger, B. A. Rybicki, J. A. Shapiro, and N. S. Weiss, "Screening by prostate specific antigen and digital rectal examination in relation to prostate cancer mortality: A case-control study," *Epidemiology*, vol. 16, no. 3, pp. 367-376, 2005.
- [5] K. Mistry, and G. Cable, "Meta-analysis of prostate-specific antigen and digital rectal examination as screening tests for prostate carcinoma," *JABFP*, vol. 16, no. 2, 2003.

- [6] J. M. Song, C. Kim, H. C. Chung, and R. L. Kane, "Prostate-Specific Antigen, Digital Rectal Examination and Transrectal Ultrasonography: A Meta-Analysis for This Diagnostic Triad of Prostate Cancer in Symptomatic Korean Men," *Yonsei Medical Journal*, vol. 46, no. 3, pp. 414 - 424, 2005.
- [7] I. Agalliu, N. S. Weiss, D. W. Lin, J. L. Stanford, "Prostate cancer mortality in relation to screening by prostate-specific antigen testing and digital rectal examination: a population-based study in middle-aged men," *Cancer Causes Control*, vol. 18, pp. 931-937, 2007.
- [8] A. Hoogendam, F. Buntinx, H. de Vet, "The Diagnostic Value of Digital Rectal Examination in Primary Care Screening for Prostate Cancer: a Meta-Analysis," *Family Practice*, vol. 16, no. 6, pp. 621-626, 1999.
- [9] J. C. Presti, "Prostate cancer: assessment of risk using digital rectal examination, tumour grade, prostate-specific antigen, and systematic biopsy," *Radiologic Clinics of North America*, vol. 38, no. 1, pp. 49-58, 2000.
- [10] T. Loch, "Urologic imaging for localized prostate cancer in 2007," *World J. Urol.*, vol. 25, pp. 121-129, 2007.
- [11] S. Song, N. B. Cho, I. I. Iordachita, P. Guion, G. Fichtinger, and L. L. Whitcomb, "A Study of Needle Image Article Localization in Confirmation Imaging of MRI-guided Robotic Prostate Biopsy," *IEEE International Conference on Robotics and Automation*, 2011.
- [12] H. B. Carter, P. C. Walsh, P. Landis and J. I. Epstein, "Expectant management of nonpalpable prostate cancer with curative intent: preliminary results," *Elsevier Journal of Urology*, vol. 167, Issue 3, pp. 1231-1234, 2002.
- [13] B. Turkbey, P. A. Pinto and P. L. Choyke, "Imaging techniques for prostate cancer: implications for focal therapy," *Nat. Rev. Urol.*, vol. 6, pp. 191-203, 2009.
- [14] G. J. Kelloff, P. Choyke, and D. S. Coffey, "Challenges in Clinical Prostate Cancer: Role of Imaging," *AJR*, vol. 192, pp. 1455-1470, 2009.
- [15] K. Shinohara, T. M. Wheeler, and P. T. Scardino, "The appearance of prostate cancer on transrectal ultrasonography: correlation of imaging and pathological examinations," *Journal of Urology*, vol. 142, no. 1, pp. 76-82, 1989.
- [16] H. B. Carter, U. M. Hamper, S. Sheth, R. C. Sanders, J. I. Epstein and P. C. Walsh, "Evaluation of transrectal ultrasound in the diagnosis of prostate cancer," *The Journal of Urology*, vol. 142, pp. 1008-1010, 1989.
- [17] M. Wink, F. Frauscher, D. Cosgrove, et al., "Contrast-enhanced ultrasound and prostate cancer; a multicentre European research coordination project," *European Urology*, vol. 54, no. 5, pp. 982-993, 2008.
- [18] J. Braeckman, P. Autier, C. Garbar, et al., "Computer-aided ultrasonography (HistoScanning): a novel technology for locating and characterizing prostate cancer," *BJU International*, vol. 101, no. 3, pp. 293-298, 2008.

- [19] D. Beyersdorff, M. Taupitz, B. Winkelmann, et al., "Patients with a history of elevated prostate-specific antigen levels and negative transrectal US-guided quadrant or sextant biopsy results: value of MR imaging," *Radiology*, vol. 224, no. 3, pp. 701-706, 2002.
- [20] J. C. Presti Jr., H. Hricak, P. A. Narayan, K. Shinohara, S. White, and P. R. Carroll, "Local staging of prostatic carcinoma: comparison of transrectal sonography and endorectal MR imaging," *American Journal of Roentgenology*, vol. 166, no. 1, pp. 103-108, 1996.
- [21] M. Mullerad, H. Hricak, K. Kuroiwa, et al., "Comparison of endorectal magnetic resonance imaging, guided prostate biopsy and digital rectal examination in the preoperative anatomical localization of prostate cancer," *Journal of Urology*, vol. 174, no. 6, pp. 2158-2163, 2005.
- [22] C. K. Kim, B. K. Park, and B. Kim, "Localization of prostate cancer using 3T MRI. Comparison of T2-weighted and dynamic contrast-enhanced imaging," *Journal of Computer Assisted Tomography*, vol. 30, no. 1, pp. 7-11, 2006.
- [23] C. M. Tempany, X. Zhou, E. A. Zerhouni, et al., "Staging of prostate cancer: results of Radiology Diagnostic Oncology Group project comparison of three MR imaging techniques," *Radiology*, vol. 192, no. 1, pp. 47-54, 1994.
- [24] M. Abd-Alazeez¹, A. Kirkham³, H. U. Ahmed, M. Arya, E. Anastasiadis, S. C. Charman, A. Freeman and M. Emberton, "Performance of multiparametric MRI in men at risk of prostate cancer before the first biopsy: a paired validating cohort study using template prostate mapping biopsies as the reference standard," *Nature Prostate Cancer and Prostatic Disease*, 2013.
- [25] J. Scheidler, H. Hricak, D. B. Vigneron, et al., "Prostate cancer: localization with three-dimensional proton MR spectroscopic imaging—clinicopathologic study," *Radiology*, vol. 213, no. 2, pp. 473-480, 1999.
- [26] G. Brown, D. A. Macvicar, V. Ayton, and J. E. Husband, "The role of intravenous contrast enhancement in magnetic resonance imaging of prostatic carcinoma," *Clinical Radiology*, vol. 50, no. 9, pp. 601-606, 1995.
- [27] B. Issa, "In vivo measurement of the apparent diffusion coefficient in normal and malignant prostatic tissues using echoplanar imaging," *Journal of Magnetic Resonance Imaging*, vol. 16, no. 2, pp. 196-200, 2002.
- [28] D. Beyersdorff, A. Winkel, B. Hamm, S. Lenk, S. A. Loening, and M. Taupitz, "MR imaging-guided prostate biopsy with a closed MR unit at 1.5 T: initial results," *Radiology*, vol. 234, no. 2, pp. 576-581, 2005.
- [29] K. M. Pondman, J. J. Fütterer, B. ten Haken, et al., "MR-guided biopsy of the prostate: an overview of techniques and a systematic review," *European Urology*, vol. 54, no. 3, pp. 517-527, 2008.
- [30] I. J. Liu, M. B. Zafar, Y.-H. Lai, G.M. Segall, and M. K. Terris, "Fluorodeoxyglucose positron emission tomography studies in diagnosis and staging of clinically organ-confined prostate cancer," *Urology*, vol. 57, no. 1,

pp. 108-111, 2001.

- [31] P. J. Effert, R. Bares, S. Handt, J. M. Wolff, U. B`ull, and G. Jakse, "Metabolic imaging of untreated prostate cancer by positron emission tomography with 18fluorine-labeled deoxyglucose," *Journal of Urology*, vol. 155, no. 3, pp. 994-998, 1996.
- [32] R. Schiavina, V. Scattoni, P. Castellucci, et al., "¹¹C-choline positron emission tomography/computerized tomography for preoperative lymph-node staging in intermediate-risk and high-risk prostate cancer: comparison with clinical staging nomograms," *European Urology*, vol. 54, no. 2, pp. 392-401, 2008.
- [33] K. Bouchelouche, J. Capala, and P. Oehr, "Positron emission tomography/computed tomography and radioimmunotherapy of prostate cancer," *Current Opinion in Oncology*, vol. 21, no. 5, pp. 469-474, 2009.
- [34] Y. C. Fung, *Biomechanical properties of living tissue*, Springer Verlag, New York, 1981.
- [35] W. A. D. Anderson, *Pathology*, C. V. Mosby Co., St. Louis, 1953.
- [36] D. Zink, A. H. Fischer, and J. A. Nickerson, "Nuclear structure in cancer cells," *Nature Reviews (Cancer)*, vol. 4, pp. 677-687, 2004.
- [37] J. A. Tuxhorn, G. E. Ayala and D. R. Rowley, "Reactive stroma in prostate cancer progression," *Journal of Urology*, vol. 166, pp. 2472-2483, 2001.
- [38] T. A. Krouskop, T. M. Wheeler, F. Kallel, B. S. Garra and T. Hall, "Elastic Moduli of Breast and Prostate under Compression," *J. Ultrasonic Imaging*, vol. 20, pp. 260-274, 1998.
- [39] M. Zhang, P. Nigwekar, B. Castaneda, K. Hoyt, J. V. Joseph, A. Agnes, E. M. Messing, J. G. Strang, D. J. Rubens, and K. J. Parker, "Quantitative Characterization of Viscoelastic Properties of Human Prostate Correlated with Histology," *J. Ultrasound in Med. & Biol.*, vol. 34, no. 7, pp. 1033-1042, 2008.
- [40] M. Zhang, P. Nigwekar, B. Castaneda, K. Hoyt, J. V. Joseph, A. Agnes, EE. M. Messing, J. G. Strang, D. J. Rubens, and K. J. Parker, "Quantitative Characterization of Viscoelastic Properties of Human Prostate Correlated with Histology," *Ultrasound in Med. & Biol.*, vol. 34, no.7, pp. 1033-1042, 2008.
- [41] N. Miyanaga, H. Akaza, M. Yamakawa, T. Oikawa, N. Sekido, S. Hinotsu, K. Kawai, T. Shimazui, and T. Shiina, "Tissue elasticity imaging for diagnosis of prostate cancer: a preliminary report," *Int. J. Urol.*, vol. 13, no. 12, pp. 1514-1518, 2006.
- [42] L. Pallwein, M. Mitterberger, J. Gradl, F. Aigner, W. Horninger, H. Strasser, G. Bartsch, D. zur Nedden, and F. Frauscher "Value of contrast-enhanced ultrasound and elastography in imaging of prostate cancer," *Curr. Opin. Urol.*, vol. 17, no. 1, pp. 39-47, 2007.
- [43] K. K`onig, U. Scheipers, A. Pesavento, A. Lorenz A, H. Ermert, and T. Senge, "Initial experiences with real-time elastography with real-time elastography guided biopsies of the prostate," *J. Urol.*, vol. 174, no. 1, pp. 115-117, 2005.

- [44] L. Pallwein, M. Mitterberger, P. Struve, W. Horninger, F. Aigner, G. Bartsch, J. Gradl, M. Schurich, F. Pedross and F. Frauscher, "Comparison of sonoelastography guided biopsy with systematic biopsy: impact on prostate cancer detection," *Eur. Radiol.*, vol. 17, no. 9, pp. 2278-2285, 2007.
- [45] A. Samani, J. Bishop, D. B. Plewes, "A Constrained Modulus Reconstruction Technique for Breast Cancer Assessment," *IEEE Trans. Medical Imaging*, vol. 20, no. 9, pp. 877-85, 2001.

Chapter 2

A Fast Shape-Similarity-Based Ultrasound Elastography Technique for Prostate Cancer Diagnosis

A variant of this chapter has been submitted to the journal of Computer Methods in Biomechanics and Biomedical Engineering.

2.1 Introduction

Prostate cancer is the second common cancer among men worldwide, and it remains the second leading cancer-related cause of death in mature men [1]. This disease can be even cured if it is detected at early stages, implying that prostate cancer detection at early stages is very critical for desirable treatment outcome. The necessity of tackling this disease led research groups to make efforts towards developing highly effective prostate cancer diagnosis and treatment techniques. The gold standard diagnostic technique of prostate cancer is transrectal ultrasound (TRUS) guided needle biopsy followed by histopathological assessment. However, this technique has a number of drawbacks including patient discomfort, risk of infection and cost in addition to its high rate of false negative [2]. As such, it is desirable to have alternate reliable diagnostic techniques with the aim of minimizing the number of unnecessary needle biopsies. Conventional prostate cancer screening and detection techniques, such as Digital Rectal Examination (DRE),

Prostate-Specific Antigen (PSA) are known to have low sensitivity and specificity [3]; hence they are not suitable to achieve the objective of avoiding unnecessary needle biopsies. Furthermore, while using MRI for imaging the prostate (e.g. T2-weighted MRI imaging) has proven beneficial, cost and broad accessibility issues have prevented its routine clinical utility towards achieving that objective. Given the pathological complexities associated with prostate cancer, some research groups took another approach of imaging multiple parameters pertaining to the tissue with the aim of encompassing various signatures associated with the disease. This led to the multi-parametric imaging technique which has shown to improve prostate cancer diagnosis state of the art [4, 5]. Again, cost remains a significant hurdle that has precluded its routine clinical utility. As a result, researchers have made efforts to develop affordable yet relatively reliable techniques for prostate cancer detection and classification. The association of tissue stiffness alteration with pathology such as prostate and breast cancers is well-established [6, 7]. As such, mapping the *in vivo* mechanical properties of the prostate can potentially lead to prostate cancer detection and tumor classification with a reasonably high degree of reliability [8]. Recently, computer assisted medical intervention has gained significant attention in the medical community. Examples of this in the context of prostate cancer related intervention is computer assisted brachytherapy and needle biopsy. This method of intervention is highly sophisticated, and often involves biomechanical simulation of the prostate. Examples of such applications include virtual reality (VR) systems of prostate surgery and planning or intra-operative computer-aided prostate interventions. Padilla et al. [9] developed a VR surgery simulation system for training Transurethral Resection of the Prostate (TURP) based on a biomechanical model. DiMaio et al. [10] developed a biomechanical model to simulate needle insertion for prostate biopsy and image-guided brachytherapy, which could be potentially incorporated in a computer assisted intervention system to manage prostate cancer. In the literature of tissue biomechanical modeling, the tissue mechanical properties are often assigned values obtained from mechanical testing of *ex vivo* tissue samples. However, *ex vivo* mechanical properties are known to differ from their corresponding *in vivo* properties because of alteration in blood flow, interstitial pressure, temperature and metabolic activities. Furthermore, there is considerable variation in tissue properties among individuals,

especially when diseased tissue is involved. Previous studies have indicated that the accuracy of simulated displacements in biomechanical simulations can be highly sensitive to material properties input in the model [11-13]. Therefore, reliable biomechanical simulation of prostate requires accurate measurement of the prostate tissues mechanical properties.

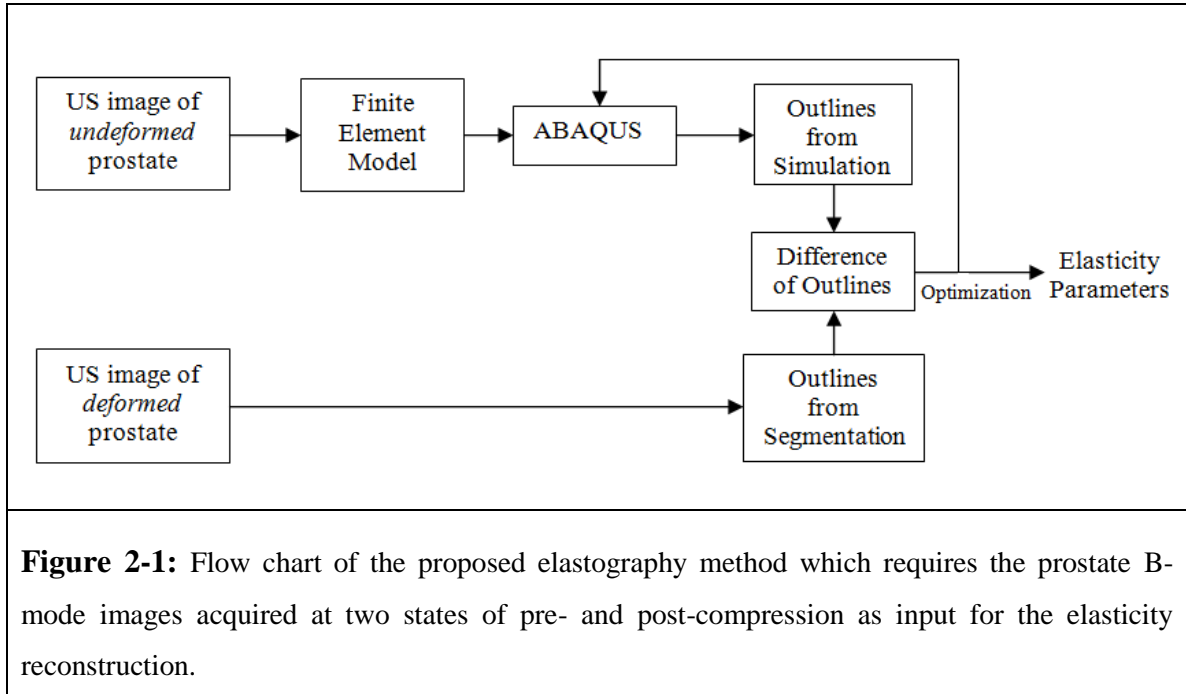
For the prostate cancer detection and diagnosis purpose, elastography has shown significant promise [14-17]. Elastography is an imaging technique that uses tissue stiffness as contrast mechanism. Several groups used the elastography concept to develop elasticity imaging techniques for prostate cancer detection and staging. The key assumption in most of these methods, which are known as strain imaging methods [18, 19], is that tissue stress distribution is uniform. The stress distribution, however, is known to be non-uniform, especially in clinical applications where this non-uniformity is very significant. While efficient given its real-time data acquisition and image visualization, strain imaging is often associated with artifacts resulting from the stress uniformity assumption. Furthermore, strain values displayed in strain images provide only a rough estimate of the tissue actual elasticity moduli, hence can only be used for rough localization of abnormal tissue regions. These issues led researchers to develop more accurate elastography techniques based on mathematical inversion of measured tissue displacement data. In these techniques, tissue stress distribution is estimated directly or indirectly based on fundamental differential equations governing the tissue mechanics. While some researchers developed methods of direct data inversion for elastic modulus reconstruction [20], others developed iterative reconstruction algorithms which involved stress field calculation using Finite Element Method (FEM) [21]. These algorithms require tissue displacements data calculated using acquired ultrasound or MRI raw data. Miga [22] developed a novel elastography technique, which does not require displacement data for elastic modulus reconstruction. This technique, instead of tissue displacement data, uses two images at pre- and post-deformation states as input for the elastic modulus image reconstruction. It is noteworthy that the displacement data is somewhat implicit in these two input images. Following this approach, Curtis and Samani [23] proposed an iterative prostate elastography technique which also uses two prostate images at pre- and post-deformation states as input for the reconstruction. Their

technique formulates the elasticity reconstruction problem as an optimization problem with the aim of finding the elastic modulus distribution parameters that lead to maximum similarity between the measured post-deformation image and its corresponding image calculated by deforming the pre-deformed image using FEM. In this paper, we follow a similar approach to introduce a novel elastography method for the prostate Young's modulus reconstruction. This method requires only two sets of prostate pre- and post-compression TRUS B-mode images. Hence, a conventional US imaging scanner is sufficient to develop the proposed elastography system and no additional hardware or software is required for tissue displacement data acquisition. Unlike the technique introduced in [23] which is based on the overall similarity of two images, this method relies on similarity between the most essential image features including the outlines of the prostate capsule and tumors. In other words, through an optimization algorithm, it finds a set of tissue elastic moduli that maximizes the similarity between segmented prostate capsule and tumor outlines in the prostate's post-compression B-mode image and its outlines counterpart calculated using FEM. The FEM is time-consuming; hence its incorporation in the proposed technique does not lead to real-time or near real-time image reconstruction and visualization. To address this issue, the proposed technique incorporates an alternate accelerated method for tissue deformation calculation previously developed in our laboratory [24]. For validation, *in silico* and tissue mimicking phantom studies were conducted which demonstrated that the proposed technique is robust, efficient and reasonably accurate.

2.2 Method

The proposed technique follows the constrained elastic modulus concept proposed by Samani et al. 2001 [21]. As such, it assumes that the elastic modulus is uniform within the volume of each tissue type. In 2D TRUS imaging, the probe pushes the prostate, leading to tissue compression and deformation. The outlines of the undeformed and deformed prostate capsule and tumors represent essential elements that characterize the prostate displacements field. These deformed outlines depend on the amount and direction of the probe's loading and the tissues' elastic moduli. Hence, using the undeformed and deformed outlines, the tissue elastic properties can be estimated using an

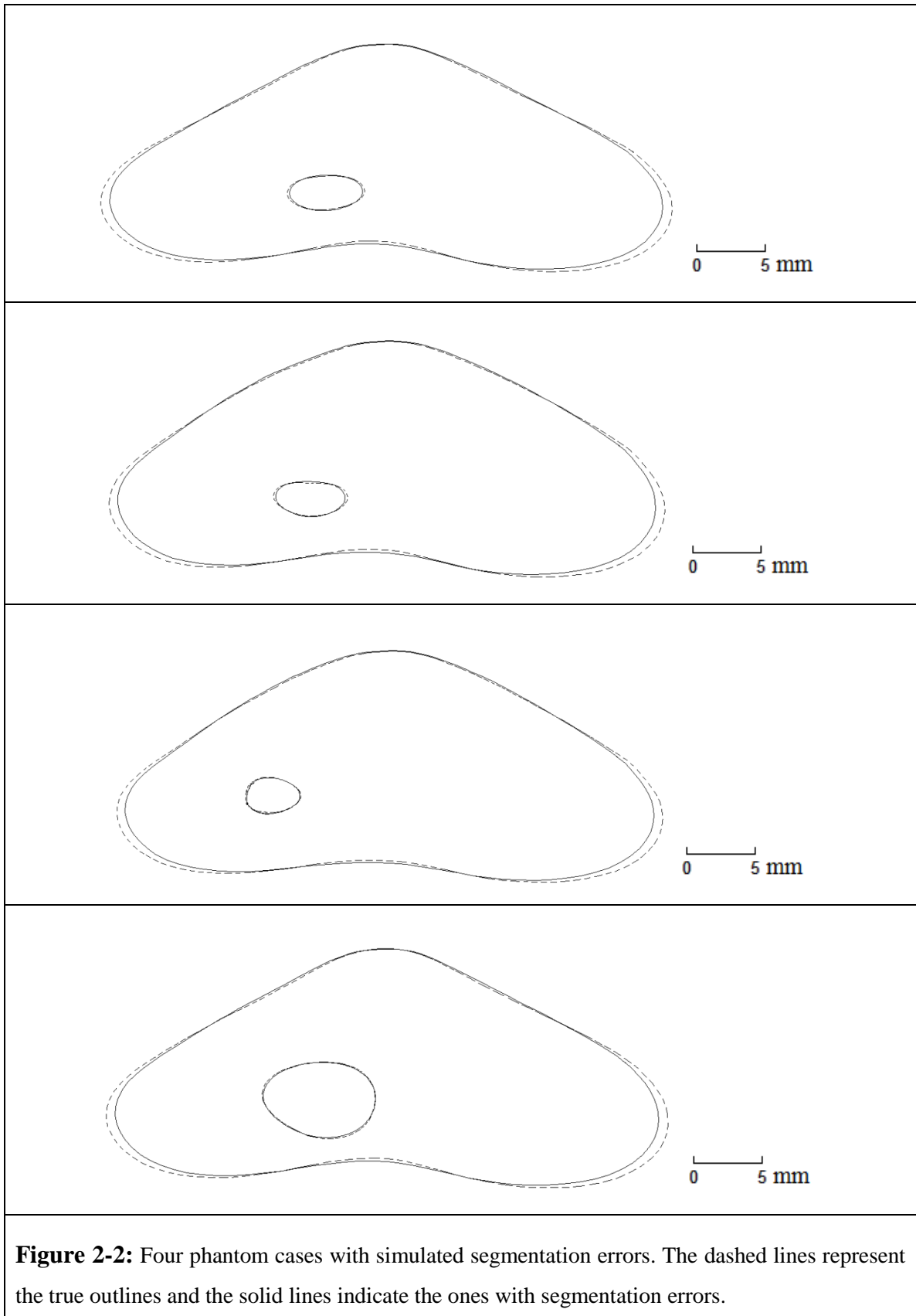
inversion technique that involves an optimization algorithm. This algorithm estimates the tissue Young's modulus distribution and parameters characterizing loading boundary conditions such that the deformed outlines calculated using FEM match their observed counterparts. Figure 2.1 shows the flow chart of the proposed method.



In this work the prostate cancer patient is assumed to undergo a TRUS imaging procedure. Therefore, the prostate, including a tumor and its surrounding tissue, is stimulated with an ultrasound probe. For the prostate tissue Young's modulus estimation, acquired TRUS B-mode images of the prostate's pre- and post-compression states will be used.

2.2.1 *In Silico* Phantom Study

This study involved 4 prostate phantom cases with various tumor locations within the peripheral zone and various tissue Young's modulus values. FE model of each phantom was created and loaded by a TRUS probe using contact problem analysis. The resulting prostate capsule and tumor outlines were considered as the observed post-compression outlines.



To assess the impact of image segmentation accuracy on the reconstructed results' reliability, random noise with maximum amplitudes of 0.84 mm and 0.21 mm was added to the theoretical deformed capsule and tumor outlines, respectively in both of the pre- and post-deformation states. These values were chosen based on the variations in prostate capsule and tumor borders manually segmented from 86 2D US prostate images. The four phantom cases are shown in Figure 2.2 where the solid lines indicate the segmentation outlines with the added errors.

2.2.2 Tissue Mimicking Phantom Study

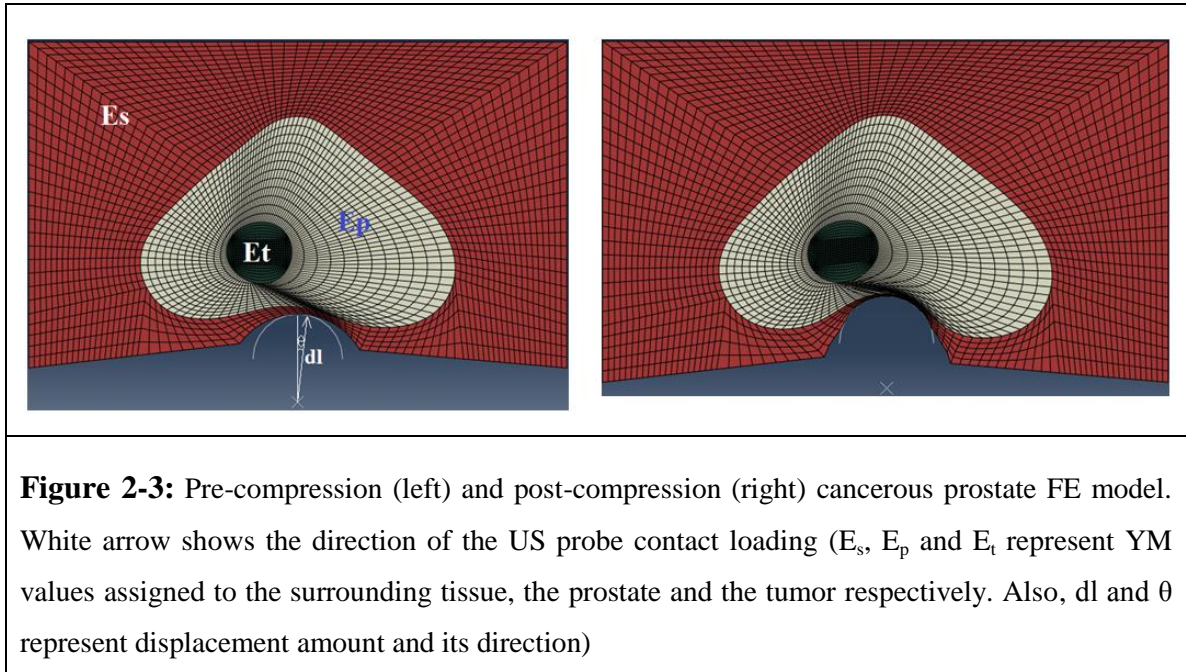
In order to validate the proposed elastography method, a tissue mimicking phantom study was conducted. The phantom was constructed using gelatin and agar (for more detail, please refer to section 3.2.5). It consisted of three parts mimicking the prostate, tumor and the prostate's surrounding tissue with the Young's modulus values close to values reported in the literature [25]. Cylindrical samples were also constructed with exactly the same material proportions to find the tissue Young's modulus values of tissues mimicking the prostate, tumor and surrounding tissue by independent uniaxial compression tests.

Using the US probe, compression was applied to the bottom of the prostate and pre- and post-compression images were acquired. These images were acquired using convex BPC8-4/10 transducer of the Ultrasonix RP system (Ultrasonix Medical Corporation, Richmond, BC, Canada). To acquire these images 5 MHz frequency was applied.

As stated earlier, the proposed method follows constrained elastography approach which requires the geometry of each tissue type. To find this geometry, image segmentation is necessary. The outlines of the prostate capsule and tumor can be obtained from the prostate TRUS B-mode images using the Discrete Dynamic Contour (DDC) technique [26]. In this technique, a rough initial outline is manually drawn by the operator. Following outline initialization, the DDC algorithm modifies the approximate outline iteratively until it converges to a smooth outline that reliably captures the borders of the prostate and its tumor(s).

2.2.3 Finite Element Modeling

After image segmentation, the pre-deformation image can be discretized into a FE mesh before it can be analyzed using FEM to obtain its predicted displacement field. The FE mesh of the prostate including the tumor(s) and surrounding tissue can be generated using a Transfinite Interpolation (TFI) based Technique [27]. A sample of such mesh is shown in Figure 2.3 where quadrilateral elements are used to create the mesh.



Mechanical stimulation of the TRUS probe is applied at the bottom of the prostate along a direction with some deviation from the posterior-anterior (PI) direction, leading to the compression of the tumor, the prostate and its surrounding tissue. The prostate tissue along with a block of surrounding tissue is incorporated in the model since, according to Saint-Venant's principle; the effect of the probe compression becomes insignificant at points far away from its application region (beyond the prostate capsule) [28]. Hence, the model contains the prostate inside a box mimicking the surrounding connective tissue. All points on the box's edges are fixed except the points on the curve that mimic the rectum wall where the probe applies compression. Different Young's moduli were assigned to the three regions of the prostate, the tumor and surrounding tissue. After FE meshing and setting the boundary conditions and loading, the prostate FE

model can be analyzed using FE solver such as ABAQUS (Dassault Systèmes Simulia Corp, USA) to obtain the post-compression outlines of the prostate capsule and tumor(s).

2.2.4 Young's Modulus Reconstruction

By obtaining the post-compression prostate capsule and tumor outlines using FEM, the prostate and tumor Young's moduli can be found by optimizing the following cost function:

$$\text{Cost Function} = |\Gamma_{FEM_p} - \Gamma_{true_p}| + |\Gamma_{FEM_t} - \Gamma_{true_t}| \quad (2.1)$$

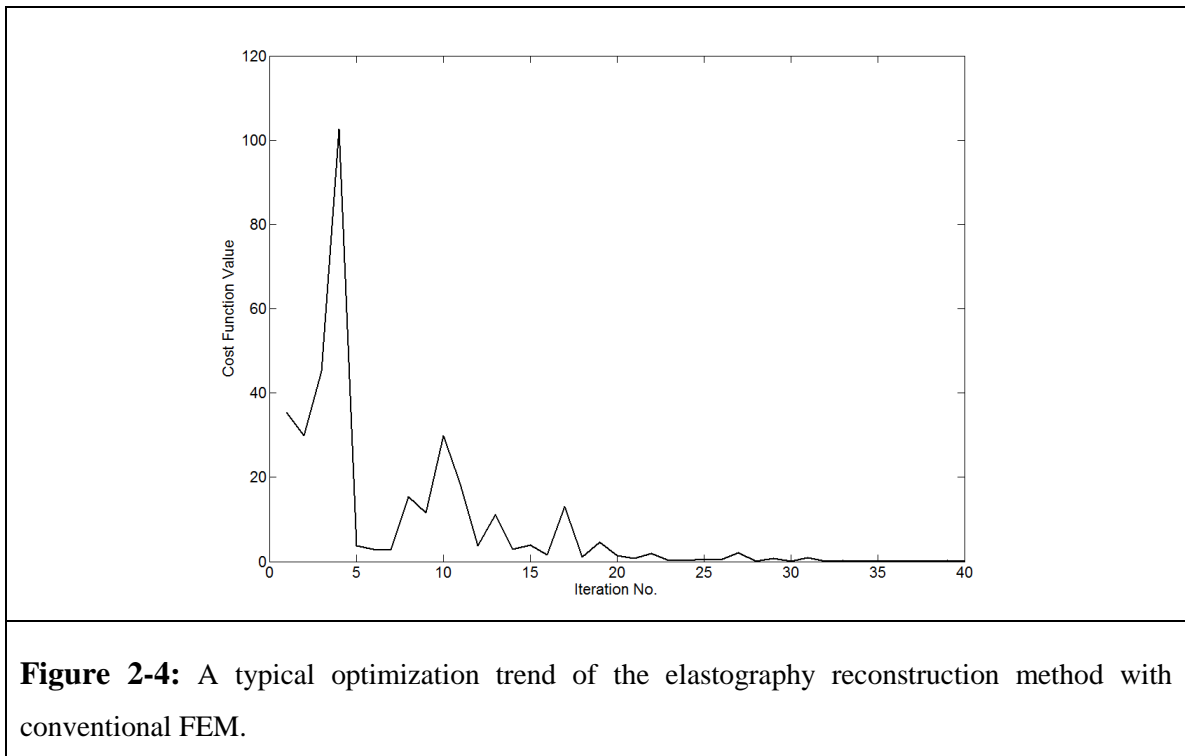
where $\Gamma_{FEM_p}, \Gamma_{FEM_t}$ represent the FEM-generated post-compression prostate capsule and tumor outlines and $\Gamma_{true_p}, \Gamma_{true_t}$ represent their true counterpart outlines obtained from the post-compression B-mode image of the prostate. Also, $|\cdot|$ is the Euclidian norm. It should be noted that Γ_{FEM_p} and Γ_{FEM_t} are functions of E_t, E_p and E_s which are the Young's Moduli of the tumor, the prostate and surrounding tissues, respectively. They are also a function of the loading. The TRUS probe's loading is modeled using contact modeling with the probe's mechanical stimulation as a prescribed displacement boundary condition with unknown magnitude (dl) and angle with the PI direction (θ). It is important to note that minimizing the cost function yields the relative Young's modulus values of E_t/E_s and E_p/E_s . Obtaining the absolute Young's modulus values requires force data which is not easy to provide. The constructed Young's modulus ratios are still expected to provide simply valuable diagnostic information pertaining to malignancy and cancer type [25]. As such, the relative Young's modulus values, E_t/E_s and E_p/E_s can be obtained using the following equation:

$$\left(\frac{E_p}{E_s}, \frac{E_t}{E_s} \right) = \arg \min_{E_t, E_p, E_s, dl, \theta} \left[|\Gamma_{FEM_p} - \Gamma_{true_p}| + |\Gamma_{FEM_t} - \Gamma_{true_t}| \right] \quad (2.2)$$

This is an optimization problem which can be solved using optimization algorithms such as Nelder-Mead's Simplex algorithm [29]. Accordingly, the step by step reconstruction algorithm can be summarized as follows:

1. Construct the Finite Element (FE) Model of the prostate and tumor using the TFI technique.
2. Input initial guess for E_t , E_p and E_s , dl, and θ .
3. Pass the FE Model with the current estimates of E_t , E_p and E_s , dl, and θ to FEM solver (e.g. ABAQUS) to obtain outlines of the prostate and tumor.
4. Calculate the cost function using Equation 2.1.
5. If the cost function does not satisfy the conditions of the Nelder-Mead's Simplex optimization method, update E_t , E_p and E_s , dl, and θ and return to 3.
6. If convergence is achieved, stop.

Using ABAQUS FEM solver to obtain the outlines is time-consuming. Figure 2.4 shows a typical optimization trend in which convergence was achieved after 32 iterations.



Each iteration involves one run of the ABAQUS solver which takes ~10 s. The total optimization time is approximately 5 minutes. In order to speed up the procedure, we used Statistical Finite Element Method (SFEM) [24] (for more detail about SFEM, please refer to Chapter 4) as an efficient alternate to the conventional FEM in the reconstruction

algorithm. This SFEM alternative has proven to be accurate as errors are less than 2% and fast as each FE process takes 0.01 seconds.

2.3 Results

As stated in the Methods, the proposed method was first validated using an *in silico* phantom study followed by a tissue mimicking phantom study. Results of these studies are reported in the following.

2.3.1 *In Silico* Phantom Study

The reconstruction algorithm was run for each *in silico* phantom and reconstructed relative Young's modulus values were obtained using conventional FEM solver and SFEM solver.

2.3.1.1 Results of the proposed elastography method using ABAQUS

Results obtained for the 4 phantom cases where segmentation errors were not considered are summarized in Table 2.1. This table provides relative Young's modulus values of E_t/E_s and E_p/E_s . Based on these results, the average errors for E_t/E_s , E_p/E_s and dl are all negligible. Results corresponding to the same 4 phantoms with simulated segmentation errors are summarized in Table 2.2. These results indicate that the average errors for E_t/E_s , E_p/E_s , dl and θ are 29.9%, 11%, 5.3% and 12.3%, respectively. This confirms the importance of image segmentation accuracy in the proposed reconstruction algorithm.

Table 2-1: Reconstruction results of the phantom study using FEM where segmentation errors are not considered.

Case		E_t/E_s	E_p/E_s	dl (mm)	θ (rad)
1	Actual Value	2.28	1.27	2.96	-0.085
	Reconstructed Value	2.28	1.27	2.96	-0.085
2	Actual Value	2.57	1.27	2.75	-0.075
	Reconstructed Value	2.57	1.27	2.75	-0.075
3	Actual Value	2.06	1.17	3.42	-0.020
	Reconstructed Value	2.06	1.17	3.42	-0.020
4	Actual Value	2.5	1.31	3.06	+0.050
	Reconstructed Value	2.5	1.31	3.06	+0.050

Table 2-2: Reconstruction results of the phantom study using FEM where segmentation errors are considered.

Case		E_t/E_s	E_p/E_s	dl (mm)	θ (rad)
1	Actual Value	2.28	1.27	2.96	-0.085
	Reconstructed Value	1.57	1.08	3.08	-0.079
2	Actual Value	2.57	1.27	2.75	-0.075
	Reconstructed Value	1.74	1.15	2.90	-0.078
3	Actual Value	2.06	1.17	3.42	-0.020
	Reconstructed Value	1.55	1.06	3.60	-0.024
4	Actual Value	2.5	1.31	3.06	+0.050
	Reconstructed Value	1.72	1.18	3.25	+0.041

2.3.1.2 Results of the proposed elastography method using SFEM

Results obtained for the 4 phantom cases where segmentation errors were not considered are summarized in Table 2.3. This table provides relative Young's modulus values of E_t/E_s and E_p/E_s . Based on these results, the average errors for E_t/E_s , E_p/E_s , dl and θ are 15%, 7.1%, 10.1% and 22.3%, respectively. Results corresponding to the same 4 phantoms with simulated segmentation errors are summarized in Table 2.4. These results indicate that the average errors for E_t/E_s , E_p/E_s , dl and θ are 32.9%, 3.5%, 4.7% and 20.8%, respectively. Using SFEM, the total process time decreases to less than a second.

Table 2-3: Reconstruction results of the phantom study using SFEM where segmentation errors are not considered.

Case		E_t/E_s	E_p/E_s	dl (mm)	θ (rad)
1	Actual Value	2.28	1.27	2.96	-0.085
	Reconstructed Value	1.77	1.21	2.75	-0.091
2	Actual Value	2.57	1.27	2.75	-0.075
	Reconstructed Value	2.56	1.14	2.60	-0.079
3	Actual Value	2.06	1.17	3.42	-0.020
	Reconstructed Value	2.37	1.06	2.66	-0.031
4	Actual Value	2.5	1.31	3.06	+0.050
	Reconstructed Value	3.05	1.36	2.88	+0.039

Table 2-4: Reconstruction results of the phantom study using SFEM where segmentation errors are considered.

Case		E_t/E_s	E_p/E_s	dl (mm)	θ (rad)
1	Actual Value	2.28	1.27	2.96	-0.085
	Reconstructed Value	1.55	1.29	3.06	-0.076
2	Actual Value	2.57	1.27	2.75	-0.075
	Reconstructed Value	1.55	1.29	2.66	-0.084
3	Actual Value	2.06	1.17	3.42	-0.020
	Reconstructed Value	1.55	1.25	3.00	-0.029
4	Actual Value	2.5	1.31	3.06	+0.050
	Reconstructed Value	1.63	1.35	3.06	+0.044

2.3.1.3 Weight Factor Effect

The reconstructed E_t/E_s values indicate that we have lost a percentage of accuracy by reconstructing the values with SFEM in real time. The loss of such accuracy may be due to the possibility that the optimization technique we used is sensitive to SFEM errors. In order to improve the results accuracy, we examined the following weighted cost function for the optimization:

$$\left(\frac{E_p}{E_s}, \frac{E_t}{E_s} \right) = \arg \min_{E_t, E_p, E_s, dl, \theta} \left[\omega \left| \Gamma_{FEM_p} - \Gamma_{true_p} \right| + (1 - \omega) \left| \Gamma_{FEM_t} - \Gamma_{true_t} \right| \right] \quad (2.3)$$

where ω is a weight factor used to adjust the capsule's outline importance with respect to that of the tumor. In order to find the optimal ω , we varied the ω from 0.1 to 0.9. A value corresponding to the minimum Young's modulus reconstruction errors will be considered as the optimal value. To accelerate the reconstruction process, we used SFEM for the simulation. The results obtained for the 4 phantom cases where segmentation errors were not considered are summarized in Table 2.5. For each ω , the average errors were

calculated based on the difference between the actual values and the corresponding reconstructed values of the four cases. This analysis indicated that the smallest errors of E_t/E_s and E_p/E_s occur when ω is 0.775. The average errors for E_t/E_s , E_p/E_s in this case are 12.8% and 8.4%, respectively.

Table 2-5: Reconstruction results of the proposed phantom study using SFEM for different weight factors where segmentation errors are not considered.

ω	Average E_t/E_s error	Average E_p/E_s error	ω	Average E_t/E_s error	Average E_p/E_s error
0.9	12.3%	11.5%	0.475	14.2%	9.7%
0.875	14.7%	9.4%	0.45	14.8%	11.0%
0.85	17.9%	8.4%	0.425	21.9%	11.0%
0.825	15.0%	8.8%	0.4	16%	13.8%
0.8	14.2%	8.6%	0.375	17.4%	12.9%
0.775	12.8%	8.4%	0.35	23.3%	13.9%
0.75	15.4%	8.3%	0.325	22.5%	15.0%
0.725	15.4%	8.2%	0.3	15.2%	14.9%
0.7	15.5%	7.8%	0.275	14.4%	14.6%
0.675	15.6%	10.0%	0.25	14.3%	15.4%
0.65	14.8%	10.2%	0.225	14.1%	15.3%
0.625	13.3%	10.0%	0.2	20.3%	18.2%
0.6	13.4%	9.2%	0.175	14.0%	14.4%
0.575	13.2%	8.2%	0.15	14.3%	14.2%
0.55	12.2%	13.4%	0.125	16.9%	12.2%
0.525	14.2%	9.5%	0.1	23.8%	16.7%
0.5	15%	7.1%	-	-	-

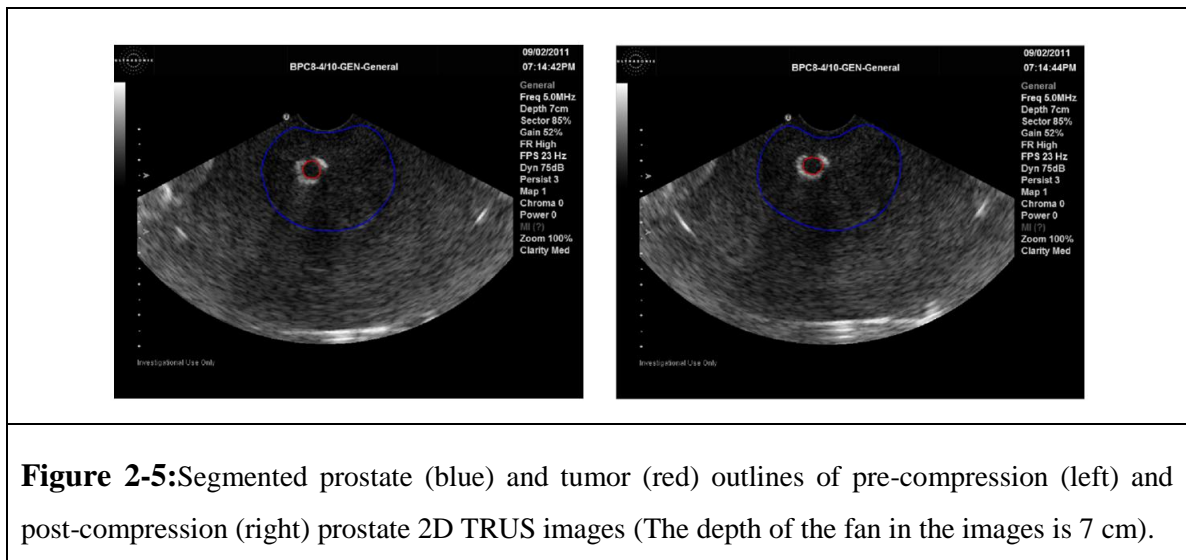
Table 2-6: Reconstruction results of the proposed phantom study using SFEM for different weight factors where segmentation errors are considered.

ω	Average E_t/E_s error	Average E_p/E_s error	ω	Average E_t/E_s error	Average E_p/E_s error
0.9	14.1%	11.4%	0.475	27.5%	10.3%
0.875	17.9%	10.8%	0.45	29.0%	11.9%
0.85	15.8%	10.3%	0.425	29.1%	10.7%
0.825	25.5%	2.5%	0.4	30%	11.4%
0.8	15.4%	7.1%	0.375	22.8%	9.3%
0.775	14.6%	6.9%	0.35	35.5%	14.1%
0.75	6.8%	11.2%	0.325	28.3%	10.6%
0.725	18.4%	8.6%	0.3	40.7%	18.3%
0.7	18.2%	11.3%	0.275	40.4%	18.0%
0.675	28.5%	15.3%	0.25	40.1%	17.5%
0.65	28.1%	14.9%	0.225	40.0%	18.2%
0.625	30.3%	13.7%	0.2	39.7%	18.4%
0.6	27.0%	13.1%	0.175	39.5%	18.6%
0.575	26.5%	11.8%	0.15	39.1%	18.9%
0.55	30.1%	10.9%	0.125	38.7%	19.2%
0.525	26.7%	9.5%	0.1	38.4%	16.3%
0.5	32.9%	3.5%	-	-	-

A similar analysis was also conducted where segmentation errors were simulated. Results obtained from this analysis are summarized in Table 2.6. The best combination of E_t/E_s and E_p/E_s errors occurs when ω is 0.75. The average errors for E_t/E_s and E_p/E_s are 6.8% and 11.2%, respectively. In both cases, the optimal value of ω is greater than 0.5 indicating that more uncertainty is associated with the tumor outline. The small average errors for E_t/E_s and E_p/E_s indicate that the method is reasonably accurate.

2.3.2 Tissue Mimicking Phantom Study

The DDC segmentation technique was applied to the phantom's pre- and post-compression 2D TRUS B-mode images to find their outlines (Figure 2.5). Having the prostate and tumor outlines from the pre-compression image, a FE model can be generated. The proposed method was then employed to reconstruct the relative elasticity moduli using both FEM and SFEM. The uniaxial compression test performed on the cylindrical samples described in the Methods led to Young's modulus values of 25 kPa, 43 kPa and 110 kPa for the surrounding tissue, prostate capsule and the tumor, respectively.



In order to investigate the repeatability of the reconstruction technique with respect to segmentation errors, the prostate capsule and tumor outlines corresponding to the two pre- and post-compression states were obtained 10 times by segmenting their 2D B-mode images starting from 10 different manually selected initial outlines. The shape similarity-based reconstruction method was then applied using $\omega = 0.75$ with each of these input

outlines in conjunction with FEM and SFEM. Results are reported in Table 2.7 Which shows that the average error for E_t/E_s and E_p/E_s were determined at $17.08\% \pm 1.11\%$ and $11.46\% \pm 1.89\%$, respectively using FEM. The average error for E_t/E_s and E_p/E_s with SFEM were calculated at $22.18\% \pm 2.49\%$ and $16.71\% \pm 2.55\%$, respectively. These errors were obtained using the true moduli values obtained from the uniaxial tests. Given the relatively small variance values, it can be concluded that the reconstructed values are not significantly sensitive to the initial DDC outline.

2.4 Discussion and Conclusions

In this paper, a novel prostate elastography technique was proposed. The advantage of this technique lies in its simplicity as it requires only two TRUS B-mode images of the prostate undergo two states of pre- and post-compression. This means that a conventional US imaging scanner is sufficient to develop the proposed elastography system while no additional hardware or software is required for the tissue displacement data acquisition. The proposed method is a constrained method where the underlying assumption is that the Young's modulus of each tissue is uniform within its volume. The reconstruction algorithm was formulated based on an inverse problem approach which led to an optimization framework. The essence of this algorithm is to find the prostate and tumor tissues' Young's modulus values that maximizes the similarity between the calculated and observed prostate capsule and tumor outlines. To obtain these outlines image segmentation is required. As such, image segmentation substitutes RF data processing in US imaging or phase imaging in MRI which are necessary for displacement data acquisition. It is noteworthy that the segmented outlines of the prostate capsule and tumor(s) under the two states of pre- and post-deformation contain essential tissue displacement information. The proposed optimization algorithm involves FEM analysis in each iteration to obtain tissue deformation corresponding to the current parameters estimate. To accelerate the reconstruction computations, SFEM was used which proved to be highly effective. While the proposed method is conceptually similar to the mutual information based elastography technique introduced by Miga [22], it differs in the fact that it focuses only on a portion of the image information and therefore it is presumably a faster and simpler method.

Table 2-7: Elasticity ratios and errors for shape similarity-based elastography method

Case		FEM		SFEM	
		E_t/E_s	E_p/E_s	E_t/E_s	E_p/E_s
1	Reconstructed Ratio	5.12	1.49	5.51	1.39
	Error	16.4%	13.4%	25.2%	19.1%
2	Reconstructed Ratio	5.07	1.47	5.32	1.45
	Error	15.3%	14.5%	20.9%	15.7%
3	Reconstructed Ratio	5.17	1.94	5.25	2.02
	Error	17.5%	12.8%	19.3%	17.4%
4	Reconstructed Ratio	5.21	1.89	5.46	1.98
	Error	18.4%	9.9%	24.1%	15.1%
5	Reconstructed Ratio	5.09	1.87	5.23	1.92
	Error	15.7%	8.7%	18.9%	11.6%
6	Reconstructed Ratio	5.14	1.52	5.43	1.40
	Error	16.8%	11.6%	23.4%	18.6%
7	Reconstructed Ratio	5.22	1.56	5.36	1.43
	Error	18.7%	9.3%	21.8%	16.8%
8	Reconstructed Ratio	5.13	1.50	5.55	1.37
	Error	16.6%	12.8%	26.1%	20.3%
9	Reconstructed Ratio	5.17	1.90	5.27	1.97
	Error	17.5%	10.6%	19.8%	14.5%
10	Reconstructed Ratio	5.19	1.53	5.38	2.03
	Error	17.9%	11.0%	22.3%	18.0%

This may be advantageous for two reasons: 1) its required computation is less intensive and 2) it is less prone to convergence to local minima. An *in silico* phantom

study and a tissue mimicking phantom study were conducted to assess the proposed method. The *in silico* phantom study involved 4 prostate phantom cases with variable tumor locations and Young's modulus values. To assess the impact of prostate capsule and tumor outline errors introduced by image segmentation, random errors were added to the known outlines vertices. These errors led to reconstruction errors of the same order which indicates the method's robustness. Another numerical experiment was conducted where the weight of the two terms, which represent the similarity between the two outlines of the prostate capsule and tumor, were varied to determine the optimal weight factors. It was concluded that weight factors of 0.775 and 0.75 were optimal in conjunction with FEM and SFEM, respectively. In the tissue mimicking prostate phantom study, pre- and post-deformation TRUS images acquired a US scanner were obtained and used as input with the proposed method. Results from this study indicated that the proposed method can reconstruct the mechanical properties of the tumor, prostate and its surrounding tissue with reasonable accuracy (with errors $< 25\%$). Based on Krouskop et al. [25] measurements, there is a contrast of 3.4 between normal prostate tissue elasticity and cancerous tissue elasticity. If the maximum YM reconstruction errors obtained in this study for the prostate and tumor are considered, the contrast will reduce to 2.2. The latter is still adequate for discriminating cancerous tumors from normal prostate tissue, especially considering that the purpose of the proposed technique is minimizing unnecessary needle biopsies and not using it as a substitute. A drawback of the proposed technique is that it requires sufficient image contrast to perform segmentation. Such contrast is not always available with prostate TRUS images; however, in cases where such contrast is available this method can provide highly valuable diagnostic information, potentially leading to tumor classification. Furthermore, this study may be considered as a proof of concept of the effectiveness of the reconstruction technique in conjunction with imaging modalities capable of providing reasonably high contrast (e.g. MRI). The reasonably high accuracy achieved when the proposed technique was implemented in conjunction with SFEM demonstrates the possibility of real-time reconstruction. Another potential application of the proposed technique is biomechanical simulation of the prostate which requires having reasonably accurate tissues' elastic moduli to achieve reliable results. As the proposed method is

capable of obtaining these moduli *in vivo*, it can be used in applications that involve biomechanical simulation of prostate. Examples of such applications include virtual reality (VR) systems of prostate surgery and computer-aided prostate intervention. Unifocal prostate cases were studied in this work. As the concept is not limited to the number of inclusions, the technique can be extended to reconstruct elasticity modulus of multifocal tumor cases by adding more similarity terms in the objective function. It is also noteworthy that the concept can be also extended to other types of cancer such as breast cancer where US or MRI images of the breast under two states of pre- and post-deformation are available.

References

- [1] Canadian Cancer Society: www.cancer.ca. Accessed April 18, 2014.
- [2] A. E. Wefer, H. Hricak, D. B. Vigneron, F. V. Coakley, Y. Lu, J. Wefer, U. Mueller-Lisse, P. R. Carroll, and J. Kurhanewicz, "Sextant localization of prostate cancer: comparison of sextant biopsy, magnetic resonance imaging and magnetic resonance spectroscopic imaging with step section histology. *Journal of Urology*, vol. 164, no. 2, pp. 400-404, 2000.
- [3] G. Salomon, J. Köllerman, I. Thederan, F. K. Chun, L. Budäus, T. Schlomm, H. Isbarn, H. Heinzer, H. Huland, M. G. Graefen, "Evaluation of Prostate Cancer Detection with Ultrasound Real-Time Elastography: A Comparison with Step Section Pathological Analysis after Radical Prostatectomy," *European Urology*, vol. 54, pp.1354-1362, 2008.
- [4] B. Turkbey, P. A. Pinto, H. Mani, M. Bernardo, Y. Pang, Y. L. McKinney, K. Khurana, G. C. Ravizzini, P. S. Albert, M. J. Merino, and P. L. Choyke, "Prostate Cancer: Value of Multiparametric MR Imaging at 3 T for Detection-Histopathologic Correlation," *Radiology*, vol. 255, no.1, pp. 89-99, 2010.
- [5] D. L. Langer, T. H. van der Kwast, A. J. Evans, J. Trachtenberg, B. C. Wilson and M. A. Haider "Prostate cancer detection with multi-parametric MRI: logistic regression analysis of quantitative T2, diffusion-weighted imaging, and dynamic contrast-enhanced MRI," *Magnetic Resonance Imaging*, vol. 30, no. 2, pp. 327-334, 2009.
- [6] Fung, Y. C., *Biomechanical properties of living tissue*, Springer Verlag, NY, 1981.
- [7] Anderson, W. A. D., *Pathology*, C. V. Mosby Co., St. Louis, 1953.
- [8] R. Souchon, O. Rouvière, A. Gelet, V. Detti, S. Srinivasan, J. Ophir, J. Y. Chapelon, "Visualisation of HIFU lesions using elastography of the human prostate *in vivo*: preliminary results," *Ultrasound Med. Biol.*, vol. 29, no. 7, pp. 1007-1015, 2003.

- [9] M.A. Padilla, S. Teodoro, E. Lira, D. Soriano, F. Altamirano and F. Arámbula, "Virtual Reality Simulator of Transurethral Resection of the Prostate," Proceedings of Pan American Health Care Exchanges (PAHCE) Conference, pp. 116-119, 2009.
- [10] S. P. DiMaio and S. E. Salcudean, "Needle Insertion Modeling and Simulation," IEEE Transactions on Robotics and Automation, vol. 19, no. 5, pp.864-875, 2003.
- [11] Y. Chi, J. Liang and D. Yan, "A material sensitivity study on the accuracy of deformable organ registration using linear biomechanical models," Med. Phys. vol. 33, no. 2, pp.421-433, 2006.
- [12] C. Tanner, J. A. Schnabel, D. L. Hill, D. J. Hawkes, M. O. Leach and D. R. Hose, "Factors influencing the accuracy of biomechanical breast models," Med. Phys., vol. 33, no. 6, pp. 1758-1769, 2006.
- [13] Y. Hu, H. U. Ahmed, Z. Taylor, C. Allen, M. Emberton, D. Hawkes and D. Barratt, "MR to ultrasound registration for image-guided prostate interventions," Med. Image Anal., vol. 16, no. 3, pp. 687-703, 2011.
- [14] M. Tsutsumi, T. Miyagawa, T. Matsumura, N. Kawazoe, S. Ishikawa, T. Shimokama, T. Shiina, N. Miyanaga and H. Akaza, "The impact of real-time tissue elasticity imaging (elastography) on the detection of prostate cancer: clinicopathological analysis," Int J Clin Oncol., vol. 12, no. 4, pp. 250-255, 2007.
- [15] M. Brock, C. von Bodman, R. J. Palisaar, B. Löppenber, F. Sommerer, T. Deix, J. Noldus and T. Eggert "The impact of real-time elastography guiding a systematic prostate biopsy to improve cancer detection rate: a prospective study of 353 patients," J Urol., vol.187, no. 6, pp. 2039-2043, 2012.
- [16] K. König, U. Scheipers, A. Pesavento, A. Lorenz, H. Ermert and T. Senge "Initial experiences with real-time elastography guided biopsies of the prostate," J Urol., vol. 174, no. 1, pp. 115-117, 2005.
- [17] L. S. Taylor, D. J. Rubens, B. C. Porter, Z. Wu, R. B. Baggs, P. A. di Sant'Agnese, G. Nadasdy, D. Pasternack, E. M. Messing, P. Nigwekar and K. J. Parker, "Prostate cancer: three-dimensional sonoelastography for in vitro detection," Radiology, vol. 237, pp. 981-985, 2005.
- [18] F. Kallel, J. Ophir, K. Magee and T. Krouskop, "Elastographic imaging of low-contrast elastic modulus distributions in tissue," Ultrasound Med Biol., vol. 24, no. 3, pp. 409-425, 1988.
- [19] F. Kallel, R. E. Price, E. Konofagou and J. Ophir "Elastographic imaging of the normal canine prostate in vitro," Ultrason Imaging., vol. 21, no. 3, pp. 201-15, 1999.
- [20] A. Skovoroda, S. Emelianov and M. O'Donnell, "Tissue elasticity reconstruction based on ultrasonic displacement and strain images," IEEE Trans. UFFC, . vol. 42, pp.747-765, 1995.

- [21] A. Samani, J. Bishop and D. B. Plewes “A Constrained Modulus Reconstruction Technique for Breast Cancer Assessment,” *IEEE Trans. Medical Imaging* vol. 20, no.9, pp. 877-85, 2001.
- [22] M. I. Miga “A new approach to elastography using mutual information finite elements,” *Phys. Med. Biol.*, vol. 48, pp. 467–480, 2003.
- [23] P. Courtis and A. Samani, “Detecting Mechanical Abnormalities in Prostate Tissue Using FE-Based Image Registration,” *MICCAI*, pp. 244-251, 2007.
- [24] S. R. Mousavi, I. Khalaji, A. Sadeghi Naini, K. Raahemifar and A. Samani, “Statistical finite element method for real-time tissue deformation estimation,” *Computer Methods in Biomechanics and Biomedical Engineering*, vol 15, no. 6, pp. 595-608, 2012.
- [25] T. A. Krouskop, T. M. Wheeler, F. Kallel, B. S. Garra and T. Hall, “Elastic moduli of breast and prostate tissues under compression,” *Ultrason Imaging*, vol. 20, no. 4, pp. 260–274, 1998.
- [26] S. Lobregt and M. Viergever, “A discrete dynamic contour model,” *Trans. Medical Imaging*, vol. 14, pp.12–24, 1995.
- [27] P. Knupp and S. Steinberg, *Fundamentals of Grid Generation*, CRS Press Inc. 1994.
- [28] Love AEH, *A treatise on the mathematical theory of elasticity*, Cambridge University Press, 1927.
- [29] J. A. Nelder and R. Mead “A simplex method for function minimization,” *Computer Journal*, vol. 7, pp. 308–313, 1965.

Chapter 3

Towards Clinical Prostate Ultrasound Elastography Using Full Inversion Approach

The material presented in this chapter has been published in journal of Medical Physics 41(3):1-12 (2014).^{*}

3.1 Introduction

Prostate cancer is the second most common cancer among men worldwide, remaining the second leading cancer-related cause of death in mature men [1]. Similar to many other types of cancer, early detection plays a vital role in successful prostate cancer treatment. Studies have shown that the 5-year survival rate of patients diagnosed with prostate cancer at early stages is more than 97% whereas this rate falls down to less than 28% for patients with late diagnosis [2]. In fact studies indicate that prostate cancer can be cured, if it is detected at early stages. Conventional prostate cancer screening and detection techniques such as Digital Rectal Examination (DRE) and Prostate-Specific Antigen (PSA) testing are known to have low sensitivity and specificity [3]. An alternate imaging

^{*} © 2014 American Association of Physics in Medicine (AAPM). This modified version has been reprinted, with permission, from S. R. Mousavi, A. Sadeghi Naini, G. Czarnota and A. Samani, "Towards Clinical Prostate Ultrasound Elastography Using Full Inversion Approach," Medical Physics, February 2014.

method for prostate cancer detection utilizes local prostate tissue stiffening as a contrast mechanism. This method is based on the fact that prostate tissue stiffness alteration is associated with pathology [4, 5]. This was demonstrated by stiffness measurement studies of ex vivo prostate tissues conducted by Krouskop et al. [6] and Zhang et al. [7]. Krouskop et al. conducted quasi-static uniaxial tests while Zhang et al. conducted stress relaxation tests for prostate tissue stiffness measurement. Based on their measurements, there is a significant difference between the Young's moduli of prostate tumor and healthy prostate tissues. As such, imaging prostate tissue stiffness can potentially lead to a prostate cancer diagnosis noninvasively with a high degree of sensitivity and specificity. For this purpose, elastography techniques were developed where tissue elasticity modulus are reconstructed and displayed [8].

For imaging tissue elasticity, the tissue is mechanically stimulated while its resulting tissue deformation data are acquired. These data are processed via an inverse problem framework to determine the spatial distribution of the tissue elastic modulus [8]. Depending on the type of mechanical stimulation, elastography methods are classified into two general categories of quasi-static and harmonic methods. In quasi-static methods, the tissue is mechanically stimulated very slowly (< 1 Hz) while resulting tissue deformation data are acquired using imaging modalities such as MR or ultrasound (US). These data are processed to obtain estimates of the tissue elastic modulus distribution. In harmonic elastography, a mechanical wave is induced in the tissue and either vibration amplitude or wave speed is measured using MRI or US imaging techniques [9-13].

Among recent works in the area of displacement data measurement using US imaging, O'Donnell et al. [14], Lubinski et al. [15], and Jiang and Hall [16] proposed speckle tracking algorithms for measuring the displacement field while Zahiri and Salcudean [17] developed a motion estimation method based on time-domain cross-correlation. More recently, Rivaz et al. [18] developed a tissue displacement measurement technique from ultrasound imaging data using dynamic programming. Other efforts were also geared towards acquiring higher quality tissue displacement data using MRI. Among others Chenevert et al. [19] developed a technique for this purpose which employs a stimulated-echo phase contrast method. Under a simplifying assumption of uniform tissue stress

distribution it can be demonstrated that tissue stiffness is proportional to its strain reciprocal. This has led to the earliest elastography techniques of strain imaging [8]. In strain imaging, higher strain values indicate softer tissue while lower strain values show stiffer tissue. Since strain images can be generated in real-time, strain imaging has been implemented in some clinical US systems. Using such methods, several groups have used transrectal ultrasound (TRUS) strain imaging for prostate cancer assessment [20-22]. However, strain imaging does not provide reliable quantitative tissue stiffness information necessary for high sensitivity and specificity because the stress spatial variation developed within the prostate tissue during TRUS is not from uniform. sensitivity and specificity of strain imaging in detecting prostate cancer is approximately 75% [3]. In order to improve strain imaging, researchers have developed full-inversion based elastography techniques which can account for tissue stress variation. Kallel and Bertrand [23] proposed a full inversion method for elasticity reconstruction. They used a Newton-Raphson method to vary a finite element (FE) model of tissue elasticity to fit a set of axial tissue displacement fields. Doyley et al. [24] proposed an inverse reconstruction technique where they also employed a modified Newton-Raphson iterative scheme for solving equations obtained from an inverse finite element framework. To achieve faster elastography image reconstruction, Oberai et al. [25] solved the elastography inverse problem using a gradient-based optimization algorithm where they employed an adjoint formulation to calculate the gradient efficiently. More recently, Jiang et al. [26] proposed a constrained optimization framework where they used regularization to solve the inverse problem iteratively. In the field of prostate cancer assessment, McGrath et al. [27] proposed a quasi-static MR elastography where they used a high field of 7 Tesla for prostate elastography. Other prostate elastography studies involved harmonic elastography. For example, Li et al. [28] and Hoyt et al. [29] reported feasibility studies aiming at prostate cancer diagnosis which involved harmonic MR and US elastography, respectively.

One difficulty with inversion based quasi-static elastography methods is that they frequently require knowledge of the tissue boundary conditions which cannot be delineated easily with US imaging [30]. In contrast, most harmonic elastography techniques involve approximations which lead to a theoretical framework that does not

incorporate the tissue boundary condition information. Such framework leads to elastic modulus distribution which mainly depends on the wave form and propagation characteristics. In this study we present a full inversion based quasi-static elastography technique for quantitative prostate cancer assessment in which accurate knowledge of patient-specific tissue boundary conditions is not necessary. Another major drawback of full inversion based elastography algorithms is that they are computationally unstable, intensive and not easy to implement. In an attempt to reduce the complexity of the inversion algorithms of elastography techniques, Samani et al. [31] developed an inversion algorithm for breast elastography. Relative tissue elastic modulus reconstruction in that algorithm is iterative, where each iteration involves tissue stress computation using FEM followed by updating Young's modulus via Hooke's law using measured strain and the computed stress. This iterative procedure is continued until convergence is achieved. Due to noise in the measured strain, such an iterative procedure is known to diverge if it is applied for each individual FE. This problem was circumvented by assuming that each tissue type, including normal and tumor tissues, is homogeneous within its volume. This assumption provided a constraint in the inversion algorithm which was used as *a priori* knowledge. With this constraint the elastic modulus of each tissue was computed by averaging the updated FE moduli within the tissue volume. While proving to be robust, the algorithm proposed by Samani et al. [31] required image segmentation to delineate tissue volumes including the tumor volume. This requirement is not easy to fulfill, especially with US imaging.

To address these issues, we present an unconstrained full inversion algorithm for ultrasound elastography. This algorithm was incorporated into a prostate US elastography technique where knowledge of prostate tissue geometry and its segmentation was not necessary. The method was validated by *in silico* and tissue mimicking phantom studies. It was also applied to clinical prostate data and results were compared to corresponding annotated histology images, which demonstrated a good potential for its clinical utility. To our knowledge, the proposed technique is the first quasi-static full inversion based prostate US elastography technique applied successfully *in vivo*.

3.2 Methodology

The proposed method was developed based on the breast elastography technique proposed by Samani et al. [31] where they presented a Young's modulus (YM) reconstruction technique for cancer assessment. In their method, the tissue was considered linear elastic and isotropic undergoing small deformation. Under these conditions, the following equation derived from Hooke's law is valid for each point in the tissue volume:

$$\frac{1}{E} = \frac{\varepsilon_{11}}{\sigma_{11} - \nu\sigma_{22} - \nu\sigma_{33}} \quad (3.1)$$

In this equation ε and σ represent the tissue strain and stress resulting from mechanical stimulation, respectively. Also, 1, 2, and 3 represent three orthogonal directions and ν is the tissue's Poisson's ratio. The tissue was idealized as a near incompressible material, hence $\nu = 0.49$ was employed in the reconstruction. Samani et al. [31] measured the tissue strain using MR phase imaging technique. Their reconstruction technique is iterative as it was reformulated as $E^{i+1} = f(E^i)$ in each iteration, where f involves stress calculation using finite element method. Unless certain measures are taken, such iterative procedure is known to diverge. To avoid this issue, they assumed that the YM is constant throughout the volume of normal and suspicious tissues. Hence each tissue volume was segmented and Young's modulus values of points within each volume were averaged to obtain the tissue's YM.

3.2.1 Unconstrained Modulus Reconstruction Algorithm

Although the assumption of tissue elasticity uniformity is reasonably good, the boundaries of tissue volumes especially those of the tumor cannot be easily delineated from medical images obtained from ultrasound (US) imaging which is commonly used for real-time elastography. In prostate US elastography, 2D B-mode images are acquired using a TRUS probe. These images have relatively poor sensitivity where the prostate outline is somewhat visible while tumors are frequently indistinguishable from the surrounding tissue, hence cannot be segmented. In order to address this issue which is necessary for achieving reconstruction converge, we developed an alternate strategy that

does not require image segmentation. This strategy involves dividing the model into subsets of $n \times n$ finite elements windows where the YM averaging is performed within each window. In other words, these $n \times n$ elements windows substitute the delineated anatomical regions in the proposed reconstruction algorithm. Furthermore, in order to achieve an elasticity image with smooth YM distribution, a Gaussian smoothing filter was applied to the reconstructed Young's moduli in each iteration. Figure 3.1a shows a B-mode image of a prostate cancer patient in which the tumor is visible as a hypo-echoic area. Figure 3.1b illustrates the approach taken by Samani et al. [31] which requires image segmentation while Figure 3.1c demonstrates the proposed strategy which does not require image segmentation.

In US elastography, it is common that only the axial strain component is acquired (strain along palpation direction). Moreover, the acquired images and consequently the finite element model are both two dimensional. Hence, the following equation is adopted for the Young's modulus reconstruction. This equation is derived from one of 2D Hooke's law equations of linear elastic and isotropic material. This assumption is appropriate given the small tissue deformation induced for stimulation in prostate elastography.

$$\frac{1}{E} = \frac{\varepsilon_{11}}{\sigma_{11} - \nu\sigma_{22}} \quad (3.2)$$

Here ε_{11} , σ_{11} , and σ_{22} are axial strain, axial stress, and lateral stress, respectively. It must be noted that this equation calculates the Young's modulus reciprocal in order to suppress the experimental noise of the strain through averaging. Based on the above equation, the Young's modulus within each $n \times n$ elements window is calculated iteratively as follows:

1. Starting with an initial Young's modulus value distribution assigned to the elements, the stress field is calculated using FE analysis.
2. Having the axial strain filed from US imaging, the Young's modulus reciprocal value of each element is calculated using Equation 3.2.
3. The average Young's modulus reciprocal value of each $n \times n$ elements window is assigned to all elements in the window.

4. A Gaussian smoothing filter is applied to have a smooth distribution of the Young's modulus reciprocal values.
5. Inverse values of the Young's modulus reciprocals are calculated and considered as the updated Young's modulus values of elements.
6. Return to step 2 where the stress field is calculated using the updated Young's modulus distribution.

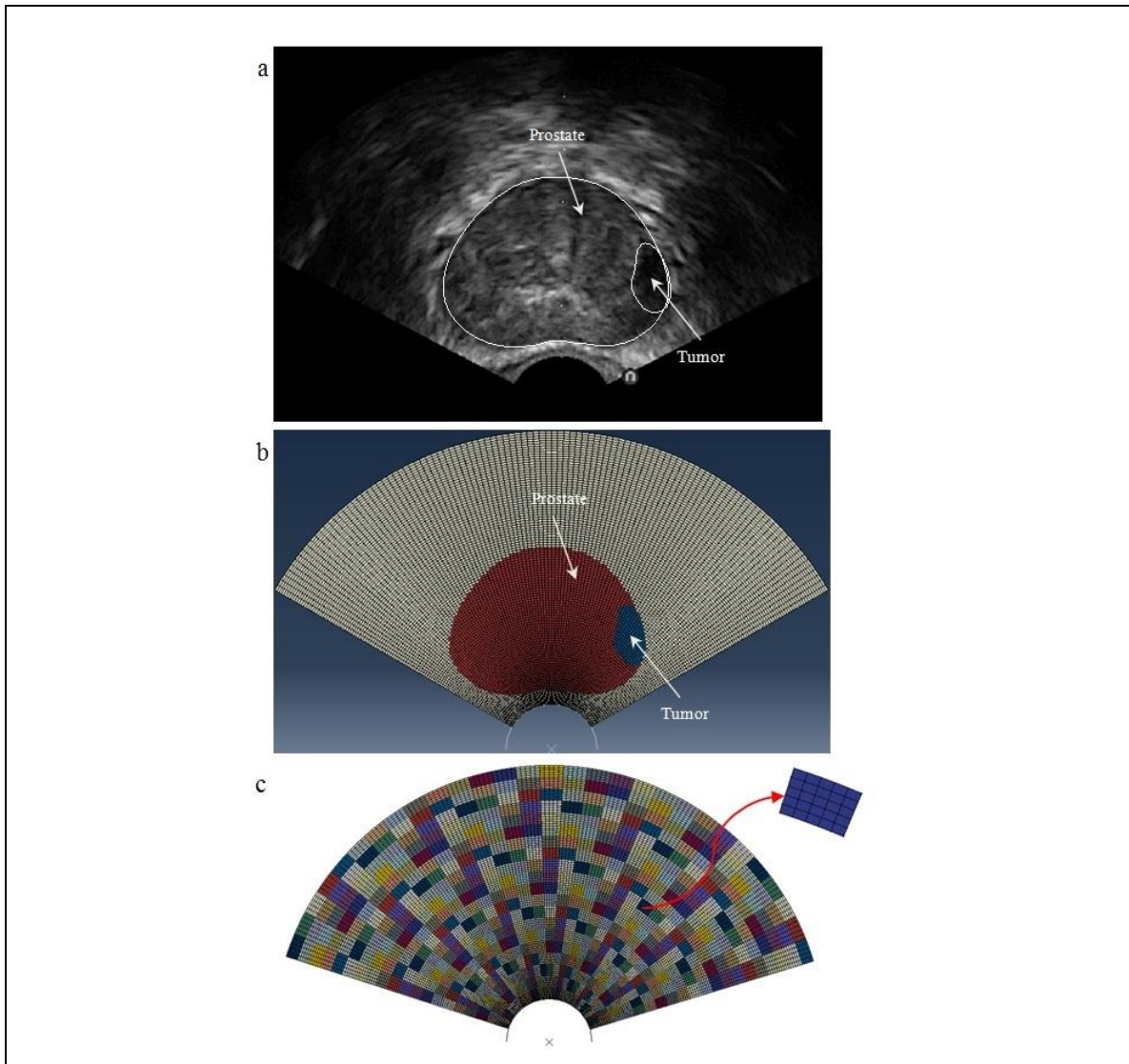
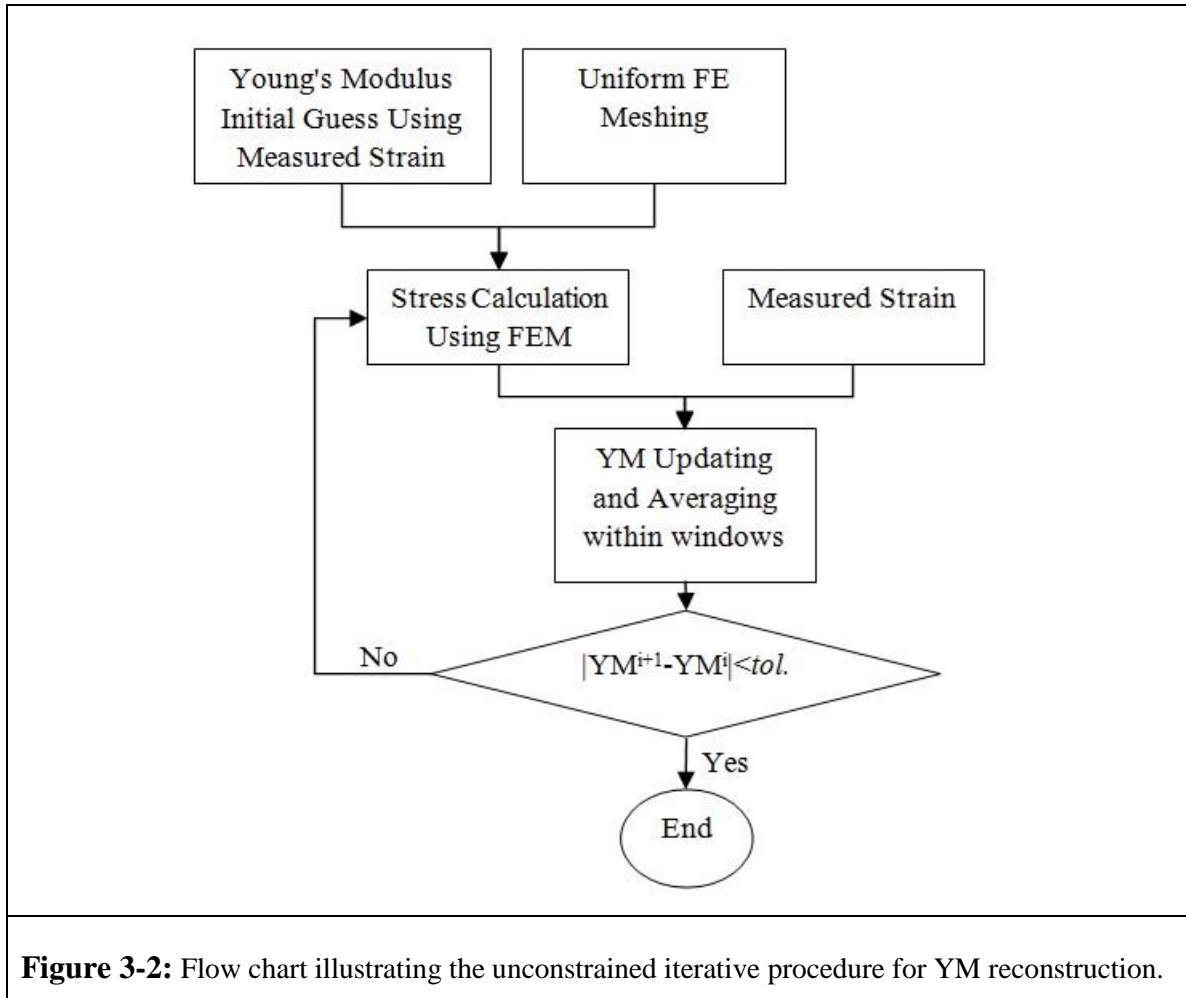


Figure 3-1: Typical B-mode image of a prostate cancer patient (the hypo-echoic area shows the tumor) (a), finite element model used for constrained elastography (b), and uniform meshing with 5×5 elements processing windows used for unconstrained iterative elastography (c). A 5×5 window is magnified and shown separately.

This iterative process is repeated until convergence is achieved where the difference between two consecutive relative Young's modulus ($E_{\text{tumor}}/E_{\text{prostate}}$) is less than a preset small value. The threshold considered for convergence in this work was 0.01 which was determined based on a trade-off between reaching iteration plateau and minimizing image blurring. The flow diagram of the proposed method is shown in Figure 3.2.



3.2.2 Strain Measurement

Clinical strain images were acquired using a Sonix RP ultrasound imaging system (Ultrasonix Medical Corporation, Richmond, BC, Canada). Strain values in these images are normalized such that the images are optimal for clinical visualization purposes. To obtain strain values necessary for YM reconstruction, we used the method developed by Rivaz et al. [17]. In this method strain values are calculated using two radiofrequency (RF) signal sets corresponding to the pre and post-compression states of tissue. Their

algorithm involves three stages. At the first stage, integer values of axial and lateral displacements are determined by minimizing a cost function that is a combination of RF similarity and displacement continuity in both axial and lateral directions. Dynamic programming is used in this stage for this minimization. In the second stage, residual values of the axial and lateral displacements are calculated using an analytical minimization of a cost function constructed based on the integer values obtained from the previous steps. At the end, strain values are calculated by applying a Kalman filter on the calculated displacement field.

3.2.3 Finite Element Modeling

In order to calculate the stress field in the prostate while undergoing mechanical stimulation induced by the TRUS probe, FEM modeling was used. This modeling requires the geometry and biomechanical properties of the tissue, including the prostate and its surrounding tissue, and its boundary conditions. In this work, 2D TRUS B-mode images were used to construct the FE model. An example of such image is the image shown in Figure 3.1.a. In TRUS, the mechanical stimulation is applied to the posterior side of the prostate through the rectum using ultrasound probe. This leads to mechanical compression of the prostate and its surrounding tissues. For FE analysis, a finite size fan shaped model is considered mimicking the fan shaped prostate B-mode image. As boundaries of the prostate and tumor tissues are assumed to be unknown, the whole block was uniformly meshed radially as shown in Figure 3.3.b. Adjacent to the loading area (TRUS probe) where high stress concentration is anticipated finer elements were employed in order to capture expected higher displacements gradients accurately. Larger elements were employed to mesh tissue volumes far from the loading area as small displacement variations are expected. All points on the model are free to move except the nodes on the anterior edge, which are restricted from movement in the radial direction due to the pubic bone. The prostate is placed about 2 cm behind the pubic symphysis, from which it is separated by a plexus of veins and a quantity of loose fat [32]. Furthermore, based on *ex vivo* measurements we conducted on four cadaveric samples, the average distance between the rectum and pubic bone is 1.75 the prostate's size. Based on this range we decided to consider each end of the RF line as a fixed boundary, which

is ~ 1.5 the prostate's size for the two patient cases presented in this paper. These points are shown in a transverse view of the prostate in Figure 3.3a. It is expected that the reconstruction error resulting from this inaccurate estimation of the fixed boundary condition points is insignificant as tissue displacements decline rapidly with distance from the US probe. Probe loading was modeled as a contact model in which a rigid body mimicking the ultrasound probe contacts the prostate's elastic finite element mesh.

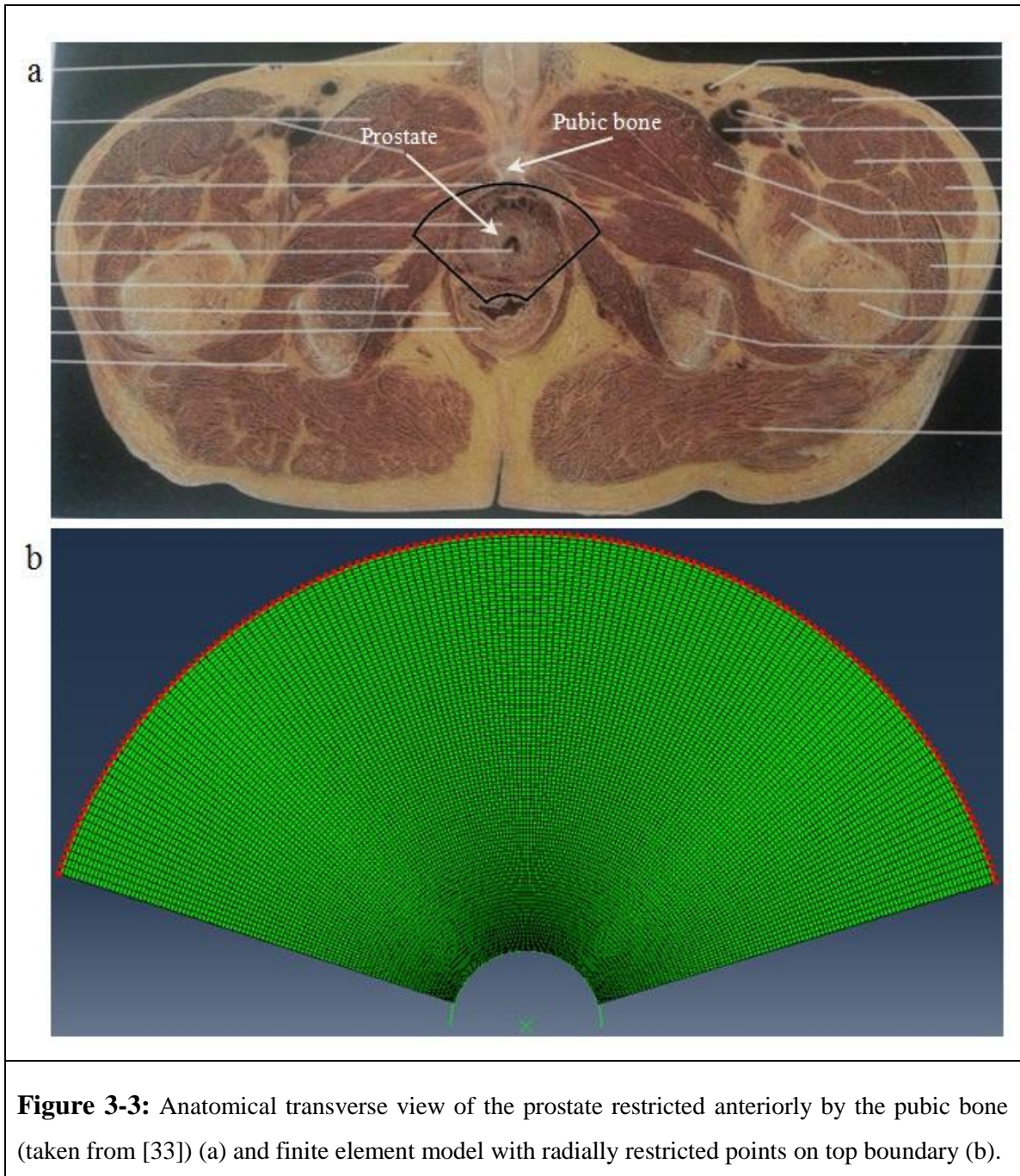
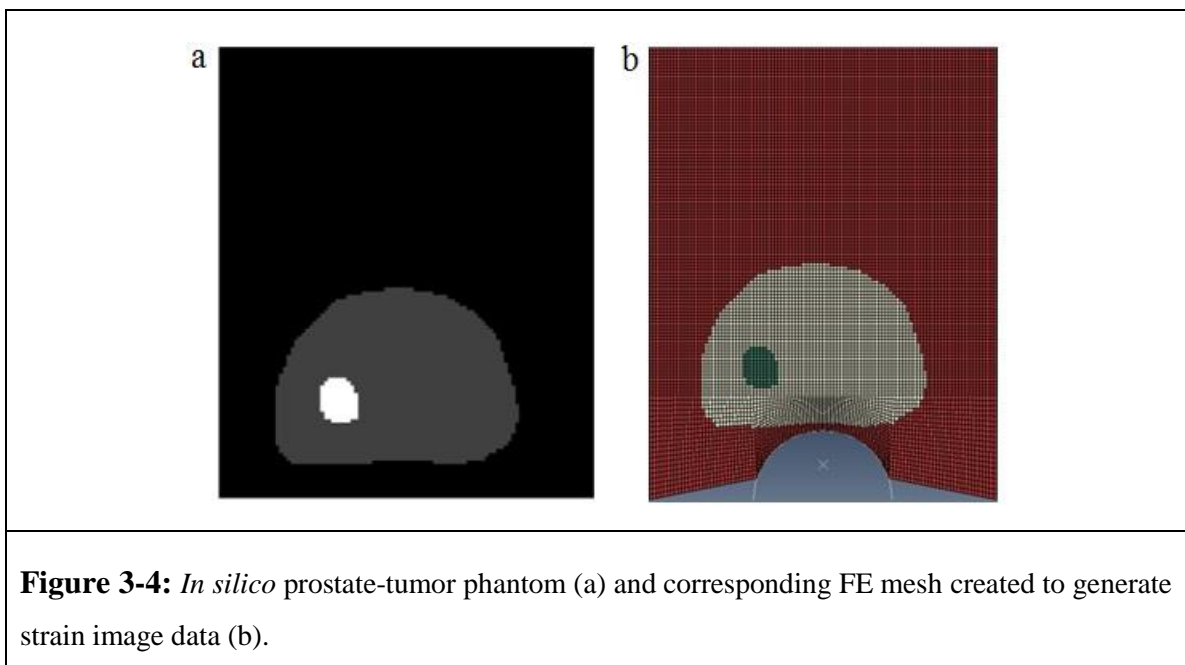


Figure 3-3: Anatomical transverse view of the prostate restricted anteriorly by the pubic bone (taken from [33]) (a) and finite element model with radially restricted points on top boundary (b).

3.2.4 *In Silico* Phantom Study

A numerical phantom study involving a prostate phantom with a small tumor, as shown in Figure 3.4.a, was conducted to assess the performance of the proposed elasticity reconstruction technique, including its sensitivity to noise. In this phantom, the ratio of tumor to surrounding tissue's YM (E_t/E_s) was set to 2.20 while the ratio of the prostate to surrounding tissue YM (E_p/E_s) was set to 1.30. These ratios are selected based on measured values given by [6] and [7]. The input strain images for YM reconstruction was computed using FE modeling of this phantom by employing ABAQUS (Dassault Systèmes Simulia Corp, Providence, RI, USA). The FE mesh created for the prostate phantom including the surrounding tissue is illustrated in Figure 3.4.b. For the unconstrained method of YM reconstruction, an optimum value for the window size, n , needs to be determined. This can be done based on the trade-off between image resolution and extent of noise suppression that determines the reconstructed YM distribution smoothness. Note that in order to have a better resolution for YM, n should be adequately small while to suppress noise effects n should be sufficiently large. A simulated prostate phantom investigation we conducted in this study indicated that a window size of 5 elements is optimum for strain SNR value 10 dB. This window size was adapted in this study.



3.2.5 Tissue Mimicking Phantom Study

The proposed elastography method was also validated with studies on tissue mimicking phantoms. The phantoms consisted of three parts which mimic the prostate, tumor, and surrounding tissues, respectively. Two phantoms were constructed where the first one included a single tumor (unifocal), while the other one included two tumors (bifocal), as illustrated in Figure 3.5.



The phantoms were constructed using gelatin and agar dissolved in water. By using different proportions of gelatin and agar for regions mimicking the prostate, tumor, and surrounding tissue, we obtained suitable YM ratios of E_t/E_s and E_p/E_s for these phantoms according to values reported in the literature [6]. Tables 3.1 and 3.2 show the amount of each material used to construct the unifocal and bifocal tissue mimicking phantoms. A few drops of formaldehyde were added to the dissolved gelatin and agar to increase the melting point of the mixture and increase the phantom's resistance against developing mould. Also, glycerol was added to the mixture to regulate the ultrasound wave speed in both the normal and tumor areas such that the wave speed is approximately 1540 m/s [34]. All the materials used to make the phantoms are manufactured by Sigma-Aldrich Co. LLC, ON, Canada. In order to have better image contrast between normal and tumor areas, different amounts of Sigmacell were added into the batch prepared for each tissue type. For validation, a cylindrical sample was constructed from each batch. These

samples were set to solidify under the same conditions for each tissue mimicking gelatin-agar material. These samples underwent uniaxial compression tests to measure their YM values independently.

Table 3-1: Amounts of different materials used for constructing different regions of the unifocal phantom.

	Gelatin (g)	Agar (g)	Water (cc)	Glycerol (cc)	Sigmacell (g)	Formaldehyde (drop)
Surrounding Tissue	15	3	250	20	2.5	1
Normal Prostate Tissue	15	6	250	20	2	1
Tumor	15	9	250	20	1.5	1

Table 3-2: Amounts of different materials used for constructing different regions of the bifocal phantom.

	Gelatin (g)	Agar (g)	Water (cc)	Glycerol (cc)	Sigmacell (g)	Formaldehyde (drop)
Surrounding Tissue	30	9.5	600	48	1	1
Normal Prostate Tissue	18	7.8	300	24	3	1
Tumor 1	9	5	150	12	0.5	1
Tumor 2	9	5.5	150	12	0.5	1

3.2.6 Clinical Study

The proposed unconstrained elastography method was also validated throughout a pilot clinical study. Two men diagnosed with localized palpable prostate cancer (T2/T3) to be treated with radical prostatectomy were recruited for this study. Transrectal ultrasound scans were performed with patients in lithotomy position using an in-house rail-based probe mount fixture. Volumetric data were collected using a Sonix RP system utilizing a 128 element curvilinear array transrectal ultrasound transducer (Vermon S.A., Tours, France) spanning the whole prostate, with a transmit frequency of 10 MHz. Acquired data consisted of B-mode images, clinical strain images, and RF data collected with a

sampling frequency of 40 MHz and processed as described in details earlier. The field of view covered 85% of the sector width with line density 512, permitting 430 RF lines per frame.

Patients underwent a radical prostatectomy surgery within 1-2 weeks after ultrasound data collection. Following surgery, patient prostatectomy specimens were fixed, sectioned, and mounted on whole-mount [35] histopathology slides. Fixation was performed in 5% formalin for up to 24 h. Embedded tissue was sectioned in a serial fashion from apex to base at a 90° orientation perpendicular to the urethra, nominally matching the orientation at which ultrasound scans were performed. Sections were then cut for staining and microscopy and mounted on 2 in. × 3 in. glass slides. Staining was performed on each slide with haematoxylin and eosin (H&E). Stained glass slides were subsequently digitized at 1 μm resolution using a confocal scanner (TISSUE scope, Huron Technologies, Waterloo, ON, Canada). The digital images were examined by a pathologist for detecting and localizing malignancies and abnormal glandular structures.

3.3 Results

3.3.1 *In Silico* Phantom Study

With the determined optimal window size of 5 × 5 elements, the proposed algorithm was applied for the given prostate phantom, leading to Young's modulus ratios of $E_t/E_s = 2.17$ and $E_p/E_s = 1.28$. The resulting Young's modulus image is shown in Figure 3.6.a. In a more realistic study, Gaussian noise was added to the strain field such that the strain SNR was 10 dB. Figure 3.6.b shows the elasticity image reconstructed from this noisy strain field using the proposed technique. In this case, the obtained elasticity ratios were $E_t/E_s = 2.32$ and $E_p/E_s = 1.39$. Errors of these two cases are reported in Tables 3.3 and 3.4, respectively. The reconstructed Young's modulus values obtained in this study and the following studies are average values calculated over each tissue region.

Table 3-3: Reconstructed YM ratio values of the in silico phantom (noise free case).

	True Value	Reconstructed Value	Error
E_p/E_s	1.30	1.28	1.5 %
E_t/E_s	2.20	2.17	1.3 %

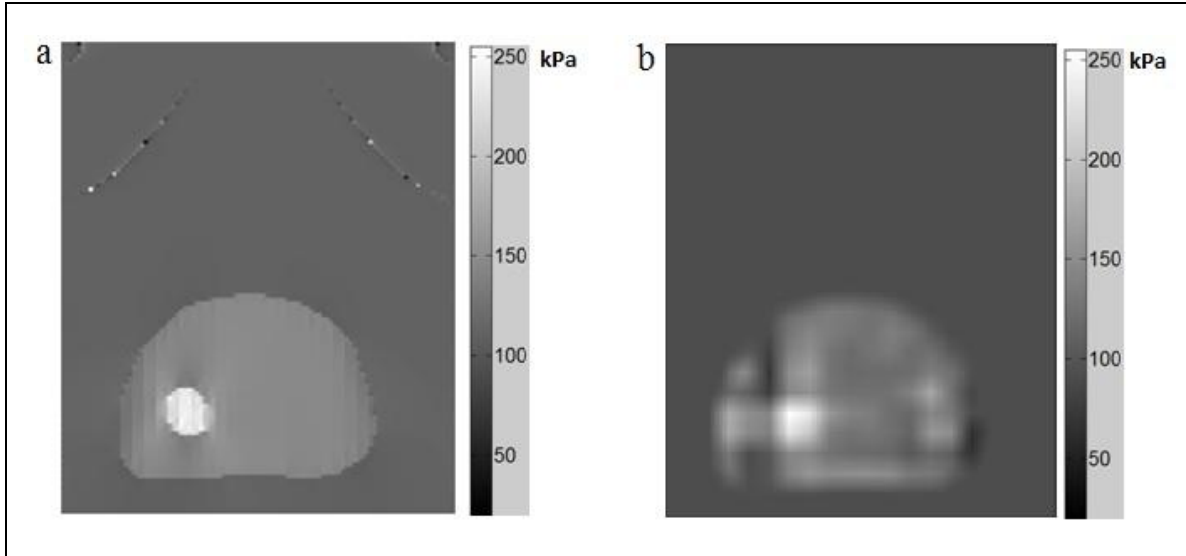


Figure 3-6: Reconstructed Young's modulus image using data with no noise (a) and reconstructed elasticity image using strain field with SNR of 10 dB (b) (The size of the rectangle is 10×8 cm).

Table 3-4: YM ratio values of the *in silico* phantom reconstructed from strain data with SNR of 10 dB.

	True Value	Reconstructed Value	Error
E_p/E_s	1.30	1.39	6.9 %
E_t/E_s	2.20	2.32	5.4 %

3.3.2 Tissue Mimicking Phantom Study

Based on the uniaxial compression tests conducted to measure the YM of each tissue mimicking part in the phantoms, the YM ratios of the unifocal phantom tissues were $E_t/E_s = 4.40$ and $E_p/E_s = 1.72$, respectively. The proposed unconstrained elastography method was applied to reconstruct these ratios. Figure 3.7 illustrates acquired B-mode ultrasound image, strain image, and reconstructed elasticity image of this phantom. Based on the strain image, the tissue YM ratios were obtained at $E_t/E_s = 1.40$ and $E_p/E_s = 0.65$, indicating an error of 68% for the tumor's relative elasticity. As shown in Table 3.5, YM ratios obtained from the reconstructed elasticity image are at $E_t/E_s = 3.92$ and $E_p/E_s = 1.66$, indicating errors of only 11% and 4% for the tumor and prostate tissues, respectively.

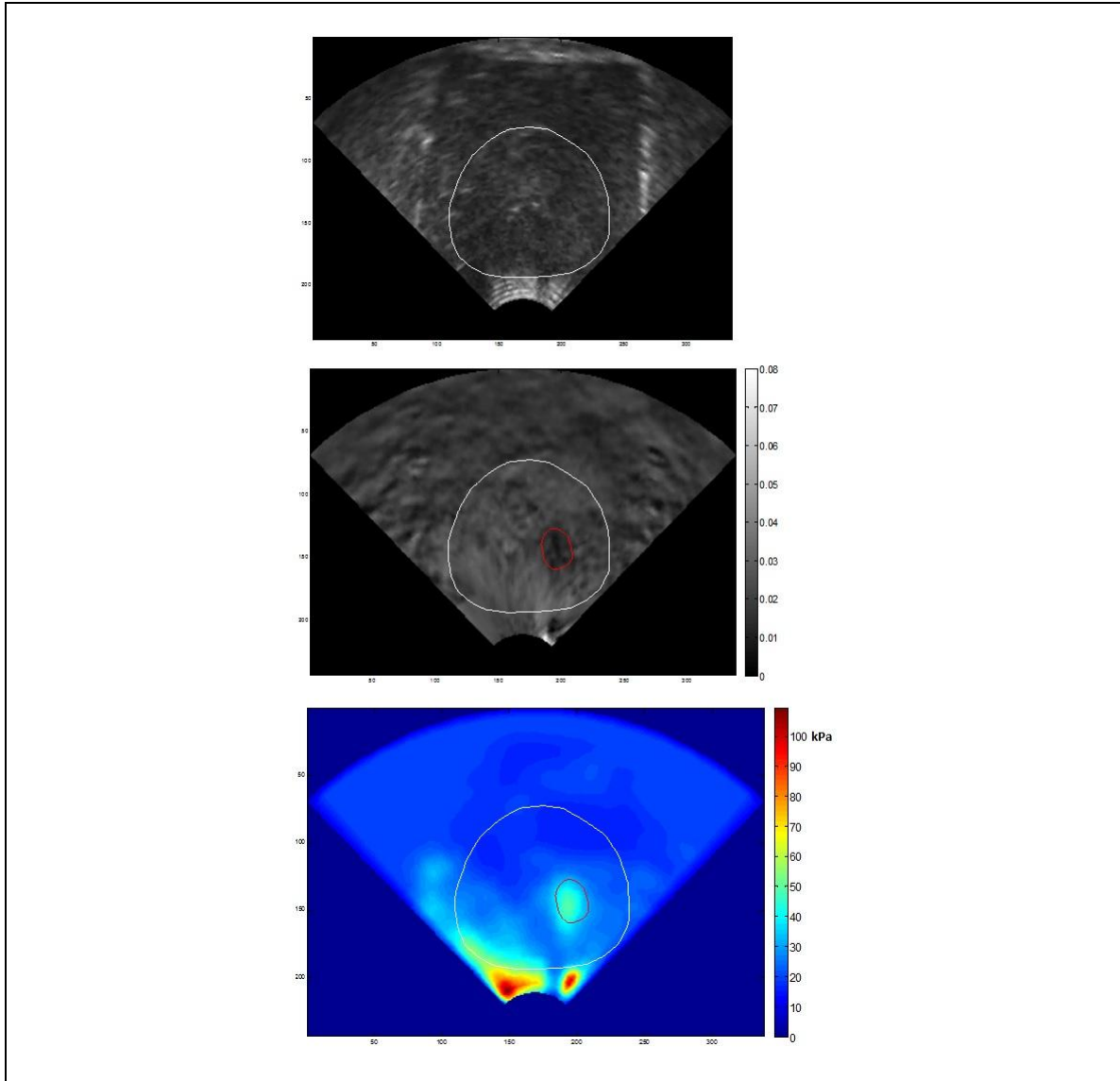


Figure 3-7: B-mode ultrasound image of the tissue mimicking phantom (top), corresponding strain image (middle), and reconstructed elasticity image using the proposed elastography technique (bottom). The tumor area has been roughly segmented based on the B-mode image on the strain and YM images. (The depth of the fan in all images is 7 cm)

Table 3-5: Reconstructed YM ratio values of unifocal tissue mimicking phantom

	True Value	Strain Imaging	Error	The proposed Method	Error
E_p/E_s	1.72	0.65	62%	1.66	4%
E_t/E_s	4.40	1.40	68%	3.92	11%

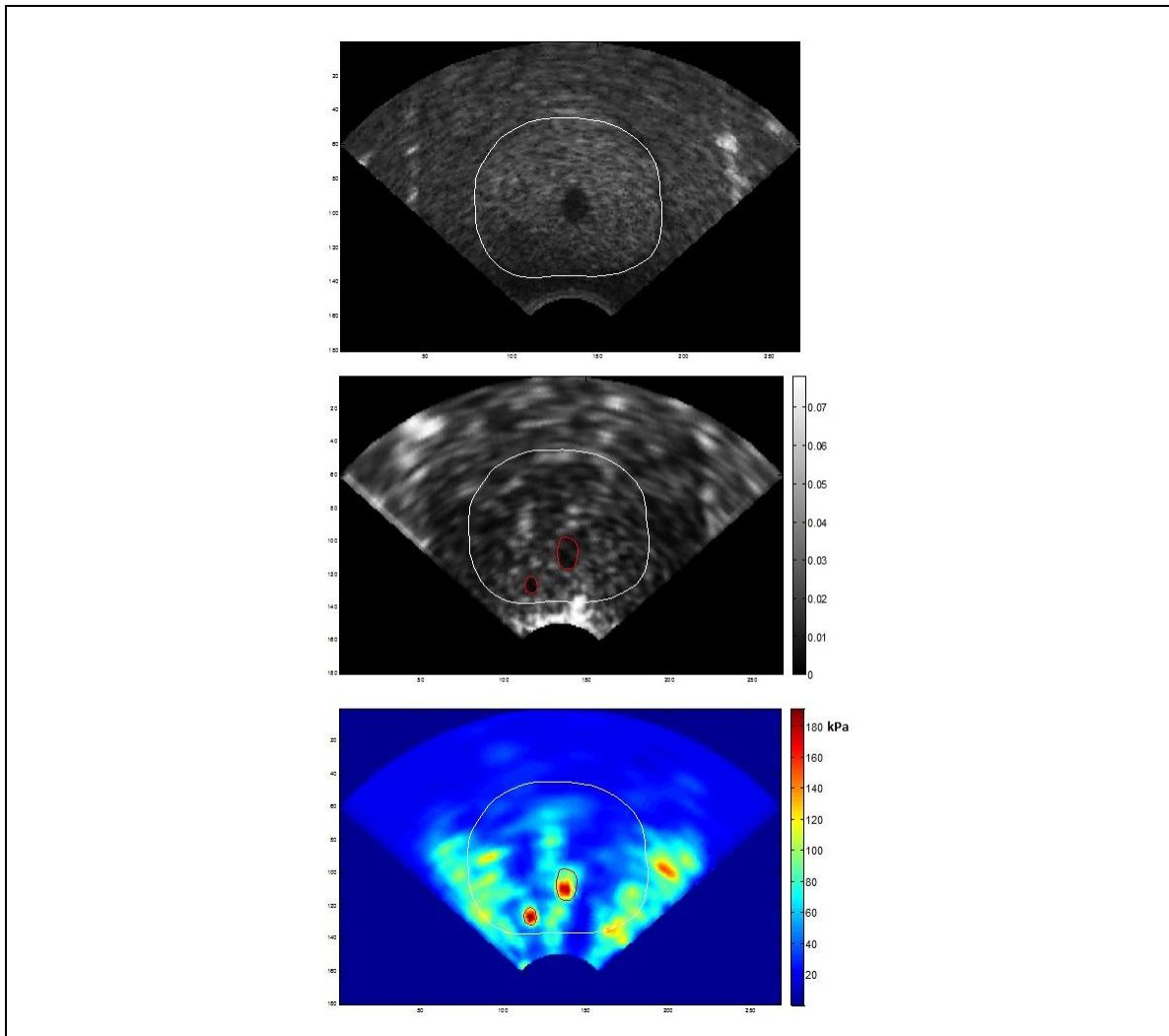


Figure 3-8: B-mode ultrasound image of the bifocal tissue mimicking phantom (top), corresponding strain image (middle), and elasticity image reconstructed using the proposed elastography technique (bottom). The tumor areas have been roughly segmented based on the B-mode image on the strain and YM images. (The depth of the fan in all images is 5 cm)

In the bifocal tumor phantom case, based on the uniaxial compression tests, YM ratios of $E_{t1}/E_s = 7.23$, $E_{t2}/E_s = 6.17$ and $E_p/E_s = 3.86$ were obtained. Acquired B mode ultrasound image, strain image, and reconstructed elasticity image of this phantom are shown in Figure 3.8. As summarized in Table 3.6, the tissues YM ratios obtained from the strain image are $E_{t1}/E_s = 11.87$, $E_{t2}/E_s = 7.75$, and $E_p/E_s = 2.77$ whereas YM ratios obtained from the reconstructed YM image are $E_{t1}/E_s = 6.56$, $E_{t2}/E_s = 5.44$, and $E_p/E_s =$

2.75, indicating errors at 9%, 12%, and 29% for tumor 1, tumor 2, and prostate tissues, respectively. Results reported in Tables 3.5 and 3.6 were obtained with a probe compression displacement estimated at 1.9 mm. Reconstructions were also performed with other US image frames corresponding to probe displacements estimated at 2.2 and 2.5 mm, leading to insignificantly different YM ratios.

Table 3-6: Reconstructed YM ratio values of bifocal tissue mimicking phantom

	True Value	Strain Imaging	Error	The proposed Method	Error
E_p/E_s	3.86	2.77	28%	2.75	29%
E_{t1}/E_s	7.23	11.87	64%	6.56	9%
E_{t2}/E_s	6.17	7.75	25%	5.44	12%

3.3.3 Patient Study

Figure 3.9 shows a histology image, B-mode image, clinical strain image, strain image calculated using the Rivaz et al. algorithm [17] and reconstructed YM image for patient 1. The large cancerous region identified within the histopathology image is barely detectable in the B-mode and clinical strain images because of their low sensitivity. However, the hypo-intensity area of the calculated strain image shows the cancerous region in the prostate's peripheral zone. Strain ratio of this region with respect to the surrounding background tissue was estimated at 7.34. Based on the smooth reconstructed YM image not only the separate nodules are detected but also their YM ratios can be calculated. The YM ratios of nodules 1 and 2 with respect to the surrounding background tissue were calculated at 3.14 and 2.68, respectively. These values were obtained with a probe displacement value estimated at 0.9 mm. Two other reconstructions were also performed with probe displacements of 1.5 and 1.7 mm which lead to YM ratio increase ranging from 15% to 18% due to tissue hyperelasticity.

Figure 3.10 shows histopathology, clinical and reconstructed strain images corresponding to patient 2. Although the clinical strain images show suspicious regions near the cancerous area, these regions do not completely fit the cancerous tissue pattern visible in the histology image. The reconstructed YM image shown in Figure 3.10e

indicates a suspicious area that is closer to the cancerous region shown in the histopathology image.

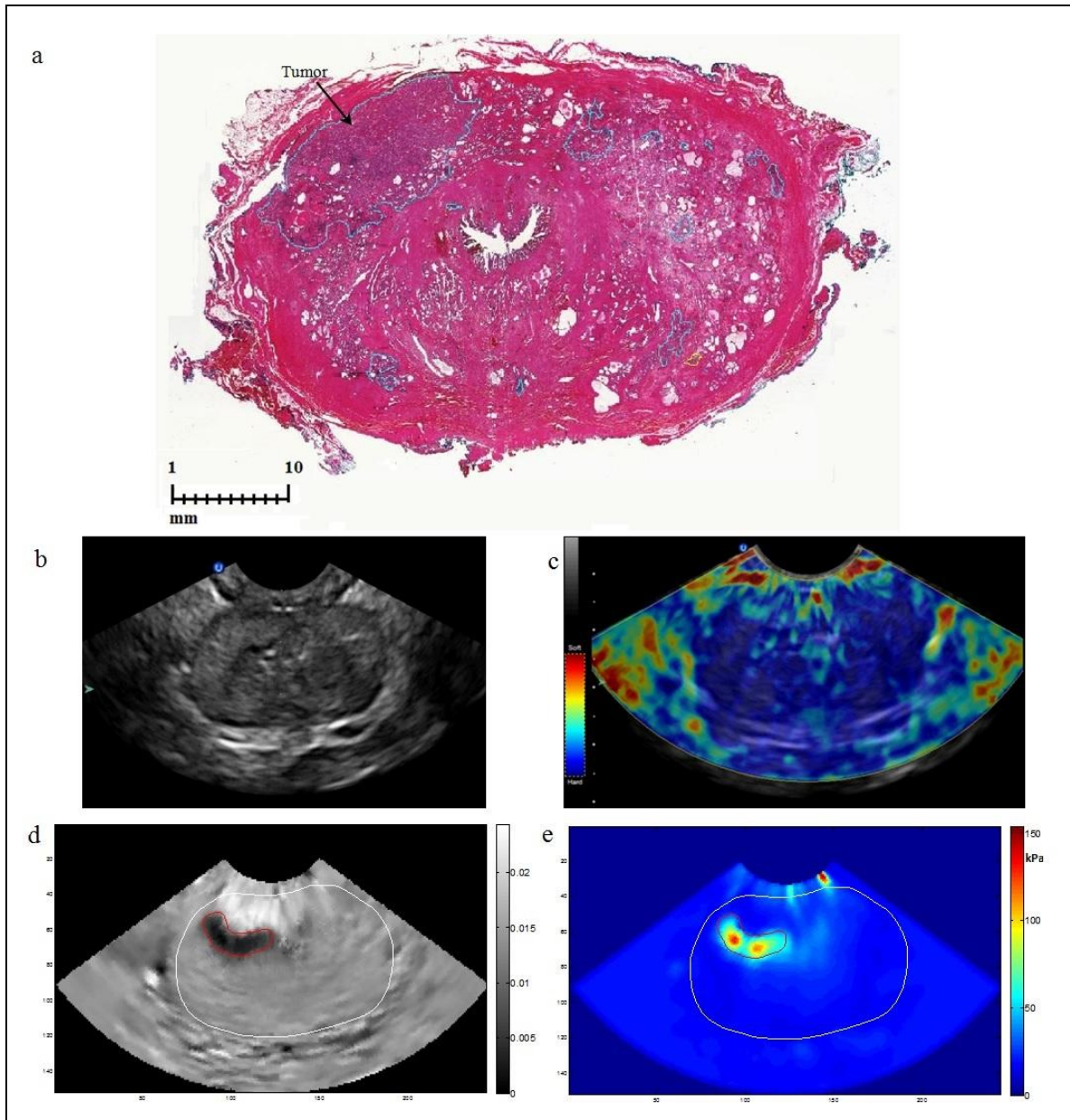


Figure 3-9: Macroscopic image of the whole-mount histopathology section of the prostatectomy specimen acquired from patient 1 (a), demonstrating the cancerous areas contoured by a pathologist. The scale bar is ~ 1 cm. B-mode ultrasound image (b), clinical strain image (c), calculated strain image (d), and reconstructed YM image corresponding to patient 1 (e). Prostate cancer is visible as a hypo-intensity area in the reconstructed strain image and as two nodules in the reconstructed YM image (contoured in white). (The depth of the fan in all images is 4 cm)

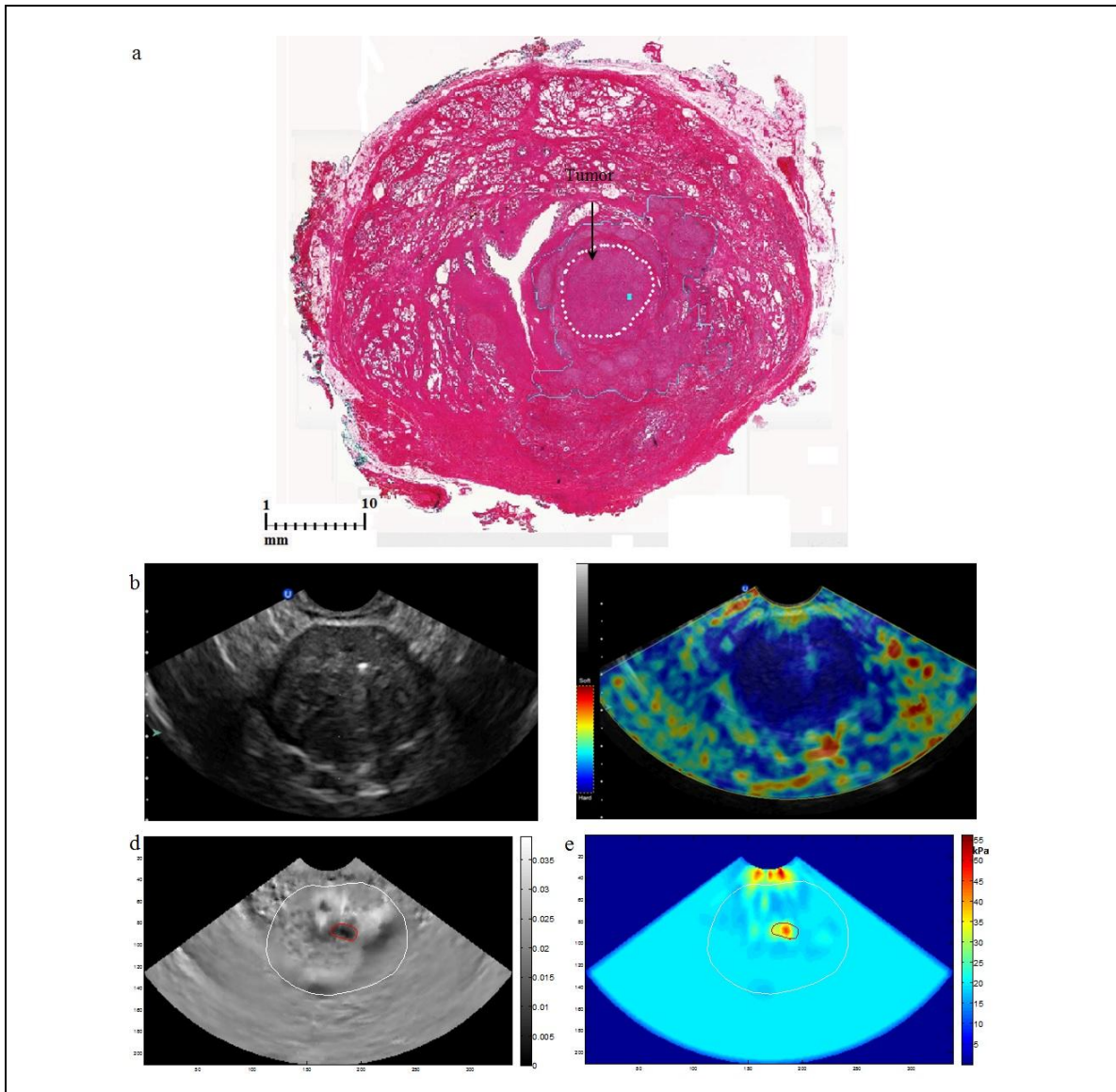


Figure 3-10: Macroscopic image of the whole-mount histopathology section of the prostatectomy specimen acquired from patient 2 (a), demonstrating the cancerous area contoured by a pathologist. The scale bar is ~ 1 cm. B-mode ultrasound image (b), clinical strain image (c), calculated strain image (d) and reconstructed YM image (e) corresponding to patient 2. The hypointensity area in the reconstructed strain image shows a single outlined tumor region. A distinct suspicious outlined area is visible in the reconstructed YM image that fits the cancerous region of the histology image. (The depth of the fan is 5cm in B-mode image and 6 cm in clinical and calculated strain images and the reconstructed YM image)

Strain and YM ratios of this region with respect to the surrounding background tissue were estimated at 6.73 and 2.31, respectively. These values were obtained with probe displacement value estimated at 1.3 mm. Two other reconstructions were also performed with probe displacements of 1.6 and 1.8 mm which lead to YM ratio increase ranging from 13% to 17% due to tissue hyperelasticity.

3.4 Discussion and Conclusions

A full inversion quasi-static US elastography technique was introduced in this paper. To our knowledge, the proposed technique is the first quasi-static full inversion-based US elastography technique applied clinically for prostate cancer diagnosis. Unlike many other US and MR elastography techniques [8-19] where boundary conditions are not considered while extensive idealizations are incorporated, the mathematical framework of this technique takes into account realistic boundary conditions and stress non-uniformity, leading to more reliable YM reconstruction. Compared to harmonic elastography techniques, however, the proposed quasi-static elastography technique is not capable of providing information related to tissue viscosity properties. The latter properties may be regarded as additional cancer biomarkers as they may potentially carry more diagnostic information pertaining to the type and staging of prostate cancer.

While harmonic US and MR elastography techniques require additional hardware attachments for wave generation in addition to *ad hoc* software including specialized pulse sequences for MR elastography, the proposed elastography technique only requires the prostate TRUS pre- and post-compression RF signals provided by a clinical ultrasound system. These data requirement can be met at a low-cost using any widely available ultrasound imaging system (e.g., Sonix RP and higher models: Ultrasonix Medical Corporation, Richmond, BC, Canada) while no additional hardware attachment is necessary. Compared to constrained elastography techniques [31, 36] another advantage of the proposed method is that it does not require image segmentation in the YM reconstruction process. In addition to reducing the computational complexity of the reconstruction, this is critical for US elastography as B-mode or strain images frequently lack enough sensitivity and SNR necessary for prostate capsule and tumor segmentation. While the proposed reconstruction algorithm is computationally more complex than

strain imaging as it requires stress analysis using FEM, its complexity is comparable to full inversion based reconstruction algorithms formulated using nonlinear optimization [24, 37-40]. Because of this time complexity issue, the method is not suitable for real-time applications. However, it may be accelerated with parallel computing using GPU programming [41] or accelerated FEM techniques such as Statistical Finite Element Method (SFEM) [42].

The proposed prostate US elastography method is robust as indicated by the *in silico* phantom study, where it was shown that it leads to highly accurate relative YM reconstruction under both noise free and noisy strain data with the highest reconstruction error of less than 7%. Furthermore, unlike strain imaging which can only detect tissue abnormality with limited accuracy, the method is quantitative as it yields the prostate's YM ratios with reasonably high accuracy as demonstrated by the tissue mimicking phantom study including the unifocal and bifocal cancer phantoms. This study showed that the YM ratio of the tumor to the surrounding tissue can be measured with errors ranging from only 5% to 11%. In addition to the reasonably high accuracy of reconstructed YM ratios, the phantom study showed that the method is also capable of accurate determination of the tumors' location and shape. The unifocal phantom case demonstrated an accurate detection of tumor location and shape.

The reconstructed relative YM pertaining to the bifocal one showed diffused tumors. The diffused shapes could have been caused by actual gelatin-agar material diffusion between the tumors and surrounding tissue. Some minor artifacts, including stiffening near the rectum, are also visible in the reconstructed YM ratio images of the tissue mimicking phantoms. These are caused by various factors including the high contact stresses near the rectum area combined with strain data with limited accuracy. Note that out of plane strain becomes significant under high tissue deformation conditions. This would introduce errors pertaining to using the 2D FE model in the reconstruction algorithm. Such conditions further impact the local relative YM reconstruction accuracy as a result of further reduction of in plane strain estimation. To address this issue more sophisticated tissue motion tracking algorithms are required. It is noteworthy that the stress calculation step using FEM may have variable spatial accuracy due to assumed

boundary conditions such as fixed and prescribed boundary conditions of the probe, leading to variable stress estimation accuracy. Results of the clinical study revealed that the proposed method can detect cancerous regions reasonably accurately. Comparing the histopathology images with the reconstructed elasticity images in some cases indicates imperfect matches between tumor location and geometry. This lack of perfect matching can be attributed to factors which contribute to image artifacts through the image reconstruction process as discussed earlier. They can also be attributed to the fact that the histopathology sections are deformed significantly compared to the corresponding in vivo prostate sections. Another contributing factor is that histopathology sections often do not exactly match the position and orientations of US scan sections, hence the nearest section to the processed B-mode view is frequently considered for comparison. Two factors may influence the proposed method's reproducibility, which are the amount and direction of the probe compression. In the experimental setup used in this study, the amount of compression is controlled by the Ultrasonix imaging system. The system is designed such that the users should apply only a limited amount of compression to have a meaningful image in the elastography mode of the Ultrasonix (a colored image within the range). As for the direction, in this investigation the operator was instructed to apply pressure in the AP direction, otherwise to provide approximate probe compression direction for the purpose elasticity reconstruction. The clinical study presented in this work should be regarded as a preliminary study to introduce the concept and assessing its potential accuracy and clinical utility. Krouskop et al. [6] showed that stiffness of *ex vivo* Benign Prostate Hyperplasia (BPH) is different from normal tissue and cancerous tissue. This implies that the technique has the potential to differentiate BPH from cancer. In fact this is one of our group's planned future works for continuing this research. Assessment of the method's sensitivity and specificity requires a thorough statistical study which should involve a relatively larger number of clinical cases with different tumor size and location scenarios. An interesting future study that may follow sensitivity and specificity assessment can be testing an important hypothesis of correlation between tumor stiffness and its level of invasiveness.

Appendix

The unconstrained elastography method proposed in this chapter does not require image segmentation. As such, it is not only capable of tumor classification but also tumor detection. As discussed in chapter 3, two factors may influence the proposed method's reproducibility, which are the amount and direction of the probe compression. In an attempt to address the concern of uncertainty in the amount and direction of probe compression, reconstruction was done with three different amounts of compression for both tissue mimicking phantom study and clinical study. For this purpose, different post-compression frames were adopted for strain reconstruction showing the different levels of loadings. Probe displacement, in each case, which is proportional to tissue deformation, was then calculated and YM ratios were reconstructed. Reconstruction results are reported in the following tables.

Table 0-1: Reconstructed YM ratio values of unifocal tissue mimicking phantom for different probe compression values.

Probe Displacement Amount (mm)	Elasticity Ratio	True Value	The proposed Method	Error
1.9	E_p/E_s	1.72	1.66	4%
	E_t/E_s	4.40	3.92	11%
2.2	E_p/E_s	1.72	1.61	6%
	E_t/E_s	4.40	4.02	9%
2.5	E_p/E_s	1.72	1.63	5%
	E_t/E_s	4.40	3.87	12%

Table 0-2: Reconstructed YM ratio values of bifocal tissue mimicking phantom for different probe compression values.

Probe Displacement Amount (mm)	Elasticity Ratio	True Value	The proposed Method	Error
1.5	E_p/E_s	3.86	2.75	29%
	E_{t1}/E_s	7.23	6.56	9%
	E_{t2}/E_s	6.17	5.44	12%
1.9	E_p/E_s	3.86	2.91	25%
	E_{t1}/E_s	7.23	6.41	11%
	E_{t2}/E_s	6.17	5.58	10%
2.2	E_p/E_s	3.86	2.63	32%
	E_{t1}/E_s	7.23	6.49	10%
	E_{t2}/E_s	6.17	5.21	15%

Table 0-3: Reconstructed YM ratio values of clinical study # 1 for different probe compression values.

Probe Displacement Amount (mm)	Index	Elasticity Ratio
0.9	$E_{\text{nodule1}}/E_{\text{background}}$	3.14
	$E_{\text{nodule1}}/E_{\text{background}}$	2.68
1.5	$E_{\text{nodule1}}/E_{\text{background}}$	3.73
	$E_{\text{nodule1}}/E_{\text{background}}$	2.87
1.7	$E_{\text{nodule1}}/E_{\text{background}}$	3.83
	$E_{\text{nodule1}}/E_{\text{background}}$	2.91

Table 0-4: Reconstructed YM ratio values of clinical study # 2 for different probe compression values.

Probe Displacement Amount (mm)	Index	Elasticity Ratio
1.3	$E_{\text{nodule1}}/E_{\text{background}}$	2.31
1.6	$E_{\text{nodule1}}/E_{\text{background}}$	2.67
1.8	$E_{\text{nodule1}}/E_{\text{background}}$	2.74

Based on this analysis, the amount of compression did not change the YM ratios significantly in the tissue mimicking phantoms. This is attributed to the fact that the gelatin-agar materials used to reconstruct the phantoms are elastic. However, the amount of compression increased the contrast between cancerous and normal tissue stiffness in clinical studies, which attributed to the fact that the prostate tissues are hyper elastic.

References

- [1] www.cancer.ca for Canadian Cancer Society. Accessed April 16 2014.
- [2] www.cancer.org for American Cancer Society. Accessed April 16 2014.
- [3] G. Salomon, J. Kollerman, I. Thederan, F. K. H. Chun, L. Budaus, T. Schlomm, H. Isbarn, H. Heinzer, H. Huland, and M. Graefen, "Evaluation of prostate cancer detection with ultrasound real-time elastography: A comparison with step section pathological analysis after radical prostatectomy," *J. Eur. Urol.*, vol. 54, pp. 1354-1362, 2008.
- [4] Y. C. Fung, *Biomechanical Properties of Living Tissue*, Springer Verlag, New York, 1981.
- [5] W. A. D. Anderson, *Pathology*, C. V. Mosby Co., St. Louis, 1953.
- [6] T. A. Krouskop, T. M. Wheeler, F. Kallel, B. S. Garra, and T. Hall, "Elastic moduli of breast and prostate under compression," *J. Ultrason. Imaging*, vol. 20, pp. 260-274, 1998.
- [7] M. Zhang, P. Nigwekar, B. Castaneda, K. Hoyt, J. V. Joseph, A. Agnes, E. M. Messing, J. G. Strang, D. J. Rubens, and K. J. Parker, "Quantitative characterization of viscoelastic properties of human prostate correlated with histology," *J. Ultrasound Med. Biol.*, vol. 34, no. 7, pp. 1033-1042, 2008.
- [8] J. Ophir, I. Céspedes, H. Ponnekanti, Y. Yazdi, and X. Li, "Elastography: A quantitative method for imaging the elasticity of biological tissues," *Ultrason. Imaging*, vol. 13, no. 2, pp. 111-134, 1991.
- [9] S. A. Kruse, J. A. Smith, A. J. Lawrence, M. A. Dresner, A. Manduca, J. F. Greenleaf, and R. L. Ehman, "Tissue characterization using magnetic resonance elastography: Preliminary results," *Phys. Med. Biol.*, vol. 45, pp. 1579-1590, 2000.
- [10] R. Sinkus, J. Lorenzen, J. Schrader, M. Lorenzen, M. Dargatz, and D. Holz, "High-resolution tensor MR elastography for breast tumor detection," *Phys. Med. Biol.*, vol. 45, pp. 1649-1664, 2000.
- [11] T. E. Oliphant, A. Manduca, R. L. Ehman, and J. F. Greenleaf, "Complex valued stiffness reconstruction for magnetic resonance elastography by algebraic inversion of the differential equation," *Magn. Reson. Med.*, vol. 45, pp. 299-310, 2001.

- [12] J. Bercoff, S. Chaffai, M. Tanter, L. Sandrin, S. Catheline, M. Fink, J. L. Gennisson, and M. Meunier, "In vivo breast tumor detection using transient elastography," *Ultrasound Med. Biol.*, vol. 29, pp. 1387-1396, 2003.
- [13] J. McLaughlin and D. Renzi, "Using level set based inversion of arrival times to recover shear wave speed in transient elastography and supersonic imaging," *Inverse Probl.*, vol. 22, pp. 707-725, 2006.
- [14] M. O'Donnell, A. R. Skovoroda, B. M. Shapo, and S. Y. Emelianov, "Internal displacement and strain imaging using ultrasonic speckle tracking," *IEEE Trans. Ultrason. Ferroelectr. Freq. Control*, vol. 41, no. 3, pp. 314-325, 1994.
- [15] M. A. Lubinski, S. Y. Emelianov, and M. O'Donnell, "Speckle tracking methods for ultrasonic elasticity imaging using short-time correlation," *IEEE Trans. Ultrason. Ferroelectr. Freq. Control*, vol. 46, no. 1, pp. 82-96, 1999.
- [16] J. Jiang and T. J. Hall, "A generalized speckle tracking algorithm for ultrasonic strain imaging using dynamic programming," *Ultrasound Med. Biol.*, vol. 35, no. 11, pp. 1863-1879, 2009.
- [17] R. Zahiri-Azar and S. E. Salcudean, "Motion estimation in ultrasound images using time-domain cross-correlation with prior estimates," *IEEE Trans. Biomed. Eng.*, vol. 53, no. 10, pp. 1990-2000, 2006.
- [18] H. Rivaz, E. Boctor, M. Choti, and G. Hager, "Real-time regularized ultrasound elastography," *IEEE Trans. Med. Imaging*, vol. 30, pp. 928-945, 2011.
- [19] T. L. Chenevert, A. R. Skovoroda, M. O'Donnell, and S. Y. Emelianov, "Elasticity reconstructive imaging by means of stimulated echo MRI," *Magn. Reson. Med.*, vol. 39, pp. 482-490, 1998.
- [20] R. Souchon, O. Rouviere, A. Gelet, V. Detti, S. Srinivasan, J. Ophir, and J. Chapelon, "Visualisation of HIFU lesions using elastography of the human prostate in vivo: Preliminary results," *J. Ultrasound Med. Biol.*, vol. 29, no. 7, pp. 1007-1015, 2003.
- [21] N. Miyanaga, H. Akaza, M. Yamakawa, T. Oikawa, N. Sekido, S. Hinotsu, K. Kawai, T. Shimazui, and T. Shiina, "Tissue elasticity imaging for diagnosis of prostate cancer: A preliminary report," *Int. J. Urol.*, vol. 13, no. 12, pp. 1514-1518, 2006.
- [22] L. Pallwein, M. Mitterberger, J. Gradl, F. Aigner, W. Horninger, H. Strasser, G. Bartsch, D. zur Nedden, and F. Frauscher, "Value of contrast-enhanced ultrasound and elastography in imaging of prostate cancer," *Curr. Opin. Urol.*, vol. 17, no. 1, pp. 39-47, 2007.
- [23] F. Kallel and M. Bertrand, "Tissue elasticity reconstruction using linear perturbation method," *IEEE Trans. Med. Imaging*, vol. 15, pp. 299-313, 1996.
- [24] M. M. Doyley, P. M. Meaney, and J. C. Bamber, "Evaluation of an iterative reconstruction method for quantitative elasticity," *Phys. Med. Biol.*, vol. 45, pp. 1521-1540, 2000.

- [25] A. A. Oberai, N. H. Gokhale, and G. R. Feijoo, "Solution of inverse problems in elasticity imaging using the adjoint method," *Inverse Probl.*, vol. 19, pp. 297-313, 2003.
- [26] J. Jiang, T. Varghese, C. Brace, E. Madsen, T. Hall, S. Bharat, M. Hobson, J. Zagzebski, and F. Lee, Jr., "Young's modulus reconstruction for radio-frequency ablation electrode-induced displacement fields: A feasibility study," *IEEE Trans. Med. Imaging*, vol. 28, no.8, pp. 1325-1334, 2009.
- [27] D. M. McGrath, W. D. Foltz, N. Samavati, J. Lee, M. A. Jewett, T. H. van der Kwast, C. Ménard, and K. K. Brock, "Biomechanical property quantification of prostate cancer by quasi-static MR elastography at 7 telsa of radical prostatectomy and correlation with whole mount histology," *Proc. Int. Soc. Mag. Reson. Med.*, vol. 19, p. 1483, 2011.
- [28] S. Li, M. Chen, W. Wang, W. Zhao, J. Wang, X. Zhao, and C. Zhou, "A feasibility study of MR elastography in the diagnosis of prostate cancer at 3.0T," *Acta Radiol.*, vol. 52, pp. 354-358, 2011.
- [29] K. Hoyt, B. Castaneda, M. Zhang, P. Nigwekar, A. Agnes, J. V. Joseph, J. G. Strang, D. J. Rubens, and K. J. Parker, "Tissue elasticity properties as biomarkers for prostate cancer," *Cancer Biomarkers*, vol. 4, pp. 213-225, 2008.
- [30] J. F. Greenleaf, M. Fatemi, and M. Insana, "Selected methods for imaging elastic properties of biological tissues," *Annu. Rev. Biomed. Eng.*, vol. 5, pp. 57-78, 2003.
- [31] A. Samani, J. Bishop, and D. B. Plewes, "A Constrained modulus reconstruction technique for breast cancer assessment," *IEEE Trans. Med. Imaging*, vol. 20, no. 9, pp. 877-85, 2001.
- [32] Henry Gray, *Anatomy of the Human Body*, Lea & Febiger, Philadelphia, 1918, see www.bartleby.com/107/. Last accessed January 7, 2014.
- [33] J. Rohen and C. Yokochi, *Color Atlas of Anatomy*, 2nd ed., Igaku-Shion Inc, New York, p. 316, 1988.
- [34] E. L. Madsen, M. A. Hobson, H. Shi, T. Varghese, and G. R. Frank, "Tissue mimicking agar/gelatin materials for use in heterogeneous elastography phantoms," *Phys. Med. Biol.*, vol. 50, no. 23, pp. 5597-5618, 2005.
- [35] G. M. Clarke, S. Eidt, L. Sun, G. Mawdsley, J. T. Zubovits, and M. J. Yaffe, "Whole specimen histopathology: A method to produce whole-mount breast serial sections for 3-D digital histopathology imaging," *Histopathology*, vol. 50, pp. 232-242, 2007.
- [36] H. Karimi, A. Fenster, and A. Samani, "A novel fast full inversion based breast ultrasound elastography technique," *Phys. Med. Biol.*, vol. 58, no.7, pp. 2219-2230, 2013.
- [37] L. Ji, J. R. McLaughlin, D. Renzi, and J. R. Yoon, "Interior elastodynamics inverse problems: Shear wave speed reconstruction in transient elastography," *Inverse Probl.*, vol. 19, pp. 1-29, 2003.

- [38] M. I. Miga, "A new approach to elastography using mutual information finite elements," *Phys. Med. Biol.*, vol. 48, pp. 467-480, 2003.
- [39] E. E. Van Houten, M. M. Doyley, F. E. Kennedy, J. B. Weaver, and K. D. Paulsen, "Initial in vivo experience with steady-state subzone-based MR elastography of the human breast," *J. Magn. Reson. Imaging*, vol. 17, pp. 72-85, 2003.
- [40] A. A. Oberai, N. H. Gokhale, S. Goenezenm, P. E. Barbone, T. J. Hall, A. M. Sommer, and J. F. Jiang, "Linear and nonlinear elasticity imaging of soft tissue in vivo: Demonstration of feasibility," *Phys. Med. Biol.*, vol. 54, pp. 1191-1207, 2009.
- [41] J. R. Joldes, A. Wittek, and K. Miller, "Real-time nonlinear finite element computations on GPU - Application to neurosurgical simulation," *Comput Methods Appl. Mech. Eng.*, vol. 199, no. 49-52, pp. 3305-3314, 2010.
- [42] S. R. Mousavi, I. Khalaji, A. Sadeghi Naini, K. Raahemifar, and A. Samani, "Statistical finite element method for real-time tissue mechanics analysis," *Comput. Methods Biomech. Biomed. Engin.*, vol. 15, no. 6, pp. 595-608, 2012.

Chapter 4

Statistical Finite Element Method for Real-Time Tissue Mechanics Analysis

*The material presented in this chapter has been published in Journal of Computer Methods in Biomechanics and Biomedical Engineering, 15(6): 595-608 (2012).**

4.1 Introduction

Many biomedical applications involve computer simulation of tissue mechanics. Examples of such applications include virtual reality (VR) systems of surgical procedures, computer-aided clinical intervention, design of prosthetic body parts and elastography imaging systems. Tissue mechanics simulators are usually based on numerical models of the tissue. Such models are often complex leading to time-consuming simulation. Some applications such as computer-aided interventional procedures and elastography image reconstruction require real-time or at least near real-time tissue computer simulation. These applications indicate that a fast and yet reasonably accurate tissue mechanics computer simulator is highly desirable.

* © 2012 Taylor & Francis. This modified version has been reprinted, with permission, S. R. Mousavi, I. Khalaji, A. Sadeghi Naini, K. Raahemifar and A. Samani., "Statistical finite element method for real-time tissue mechanics analysis," Computer Methods in Biomechanics and Biomedical Engineering, June 2012.

Since the mid-1990s, the concept of training surgeons using VR simulators was introduced, which led to efforts to develop realistic surgery simulators. The development of such simulators has also made possible novel surgical therapy procedures paving the way for robotic surgery and minimally invasive intervention. Computer-aided surgery involves updating preoperative images that is often conducted using soft tissue simulators. In such cases, limited computational resources and fast computation are two competing factors, which necessitate optimal management of computation time [1].

Satava [2] classified generations of surgical simulators into three categories. Among these, the most sophisticated one encompasses simulators that take into account anatomical, physical and physiological description of the human body. Physics-based deformable models proposed for computer graphics applications are grouped in four general categories that include Lagrangian mesh based and mesh-free methods [3]. Finite element method (FEM) and Mass Spring (MS)-based models are founded on the Lagrangian mesh-based category. They are currently the most popular techniques for tissue mechanics simulation. While FEM is known for its accuracy, it suffers from low computation speed. On the other hand, the MS-based method is the simplest and most intuitive of all deformable models. Given their high speed, MS models may seem more suitable for such applications. However, they lack solid theoretical foundations in continuum mechanics and do not lend themselves well for modeling isotropic and specific anisotropic materials. To provide MS models with suitable theoretical foundations, some researchers proposed simulators, which require tissue property input parameters derived based on FEM formulation [4, 5].

The functionality of prosthesis is determined by three factors: fitting, strength and stability. The most important factor is the strength, which can be assessed by stress analysis of the prosthesis and the surrounding tissue. The most accurate method of stress analysis in this application is FEM. To assess prosthesis or surrounding tissue mechanical failure, it is ideal to conduct stress analysis based on prosthetic parts that are custom-designed for patients. However, computation time and the associated cost required for such custom-design approach is prohibitive.

Elasticity imaging or elastography is a novel imaging technique in which elastic properties of tissues are reconstructed and displayed. Elastography image reconstruction techniques typically involve inversion of tissue displacement data using tissue biomechanical model. This reconstruction can be done iteratively where each iteration involves tissue stress analysis. Although FEM can provide highly accurate tissue stress fields, it is time-consuming and hence not suitable for real-time or near real-time imaging. As such, there are many biomedical applications that may benefit from an alternate accelerated method of tissue stress or displacement analysis.

The complexity of a finite element (FE) model depends on the number and type of elements used in the tissue model. Nonlinearity is also a significant factor that adds to the FE time complexity. The high time complexity drawback renders conventional FE models unfit for real-time tissue mechanics problems. As such, a fast technique and reasonably accurate technique that can be used as an alternate to FEM is highly desirable for applications where real-time tissue mechanics simulation is required.

In an attempt to accelerate FE analysis of a cornea model, Sagar et al. [6] developed a 3D computer graphics model of the eye in a virtual environment. In this work, the stress and displacement fields were updated every second. Bro-Nielsen [7] introduced a condensation technique [8] similar to the boundary element method, in which surface and interior nodes were decomposed and FE equations were solved on surface elements only. To speed up this technique, Bro-Nielsen and Cotin [9] inverted the stiffness matrix explicitly and used a selective matrix–vector multiplication for a linearised FE model. Later, Cotin et al. [10] used quasi-static pre-computed linear elastic models corresponding to elementary deformations of surface nodes and employed the superposition principle to compute any given deformation. However, this technique cannot incorporate patient-specific information effectively since it requires large amount of pre-calculation for any new geometry. More recently, Cotin et al. [11] introduced a dynamic, linear elastic FE-based model referred to as mass-tensor model (MTM). In the MTM, the modeled object was discretised into a tetrahedral mesh with forces calculated at the vertices of each tetrahedron. This approach facilitates faster calculation of tissue deformation as it takes advantage of preprocessed information to compute the stiffness

matrix. Similar to the previous method, the entire pre-processing procedure has to be performed for a given new object, which renders it time-consuming for clinical applications.

Model order reduction is a well-known approach to accelerate the FE analysis. The goal of model order reduction is to find a low-dimensional but accurate approximation of the large-scale quasi-static/dynamic system. With this approach, one can drastically reduce the time required for transient and harmonic simulation and find a compact representation suitable for system level simulation. Farle et al. [12] discussed several model order reduction techniques developed over the past decades in different FE-based applications. Krysl et al. [13] and Lall et al. [14] used empirical eigenvectors to achieve a reduced basis (RB) which reproduces the dynamic response of a full nonlinear system in a statistical sense. The RB methods [15, 16] were also used by other researchers for the solution of parameterized partial differential equations in elasticity problems [15, 17].

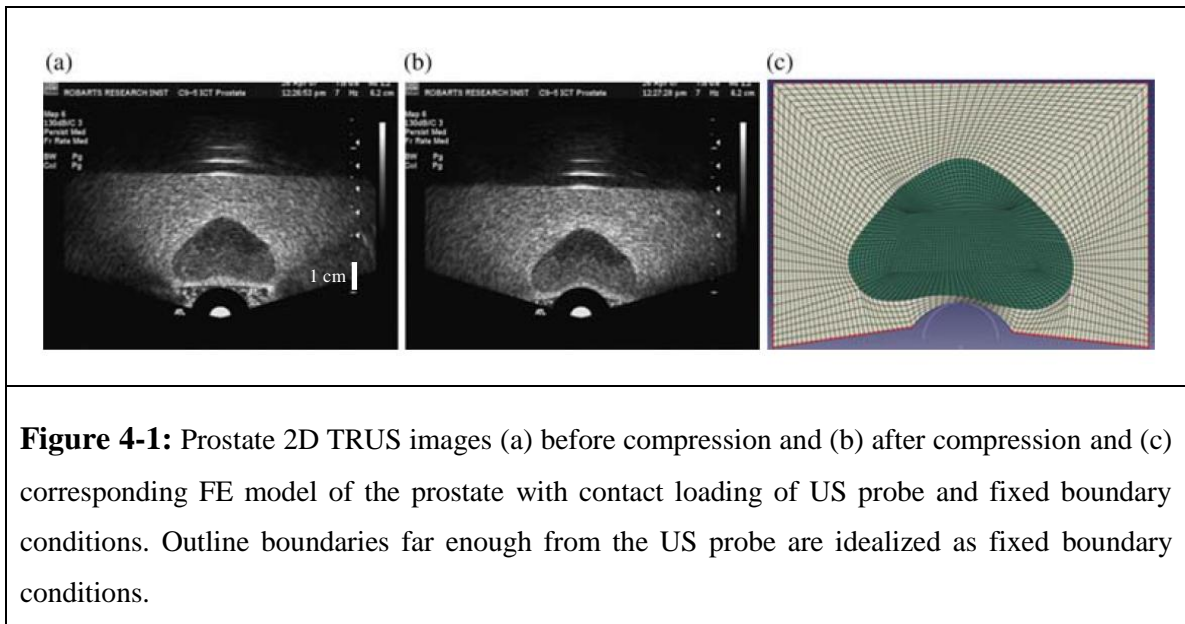
In this work, we present a novel FE-based technique to estimate the deformation and stress pattern of soft tissues. This technique is not only highly accurate but also very fast. The technique involves FE analysis of a class of organs under certain loading conditions, followed by principal component analysis (PCA) and data fitting. While the FE analysis stage is time-consuming as it involves a large number of organs, it can be done offline very effectively. Because of the substantial similarity in the geometry of a specific organ of different subjects, this approach is laid down such that it takes full advantage of tissue mechanics simulation results previously obtained for these organs. The validation results, obtained based on numerically generated shapes, are very encouraging, and demonstrate that the technique has a good potential to be utilized in biomedical applications where real-time or near real-time tissue simulation is required.

4.2 Methodology

4.2.1 Prostate Model

To calculate a displacement or stress field of tissue undergoing mechanical stimulation, FEM modelling can be used. This modelling requires the geometry and biomechanical properties of the tissue and boundary conditions. This work demonstrates the proposed

concept and methodology using a prostate model example. 2D prostate transrectal ultrasound (TRUS) images were used to construct the model. As shown in Figure 4.1, mechanical stimulation of ultrasound probe is applied to the bottom of the prostate leading to the compression of the prostate and its surrounding tissue. The prostate tissue along with a block of surrounding tissue is incorporated in the model since the effect of the probe compression becomes insignificant at points far away from its application region. Hence, as shown in Figure 4.1c, the model contains the prostate inside a box mimicking the surrounding connective tissue. All points on the box's edges are fixed except the points on the curve that mimic rectum wall where the probe applies compression. Various Young's moduli were assigned to the two regions of the prostate and surrounding tissue, and the model was discretised into an FE mesh. As the load acts in the plane of the 2D model (with small thickness) the problem is idealised as a plane stress problem.



4.2.2 Statistical Shape Model

The proposed technique in this paper, which we refer to as statistical finite element method (SFEM), is based on the statistical shape model (SSM) concept [18]. SSM is used to provide an efficient parameterisation of geometrical variability of a shape class, leading to a compact representation of shape and allowing shape constraints to be applied effectively during interpretation. In SFEM, each shape in a class of objects is

represented by a set of points encompassing its outline called ‘landmarks’. To compare equivalent points from different shapes, all shapes are aligned by scaling, rotation and translation with respect to a set of axes. Considering a set of N 2D shapes, each of which is outlined by n landmarks, every shape can be represented by a single point in a $2n$ -D space:

$$\mathbf{X}_i = (x_{i1}, y_{i1}, x_{i2}, y_{i2}, \dots, x_{ik}, y_{ik}, \dots, x_{in}, y_{in})^T \quad i = 1, \dots, N \quad (4.1)$$

Thus, a set of N shapes may be seen as a cloud of N points in this $2n$ -D space. Following the concept of PCA, Cootes et al. [18] assumed that these points lie within some region in the principal component space called ‘allowable shape domain’. Each axis in this space shows a way in which the landmark points move together in some fashion as the shape varies. As such, PCA of this data-set implies that each shape can be obtained by summing up the mean shape and a linear combination of main modes of variation, i.e.

$$\mathbf{X} = \mathbf{X}_{mean} + \mathbf{P}\mathbf{b} \quad (4.2)$$

where $\mathbf{P} = (\mathbf{p}_1 \mathbf{p}_2 \dots \mathbf{p}_t)$ is the matrix of the first t unit eigenvectors of the shapes’ covariance matrix \mathbf{S} , $\mathbf{b} = (b_1 b_2 \dots b_t)^T$ is a vector of weight factors and \mathbf{X}_{mean} is the mean shape calculated by:

$$\mathbf{X}_{mean}^T = \frac{1}{N} \sum_{i=1}^N \mathbf{X}_i \quad (4.3)$$

To calculate the set’s $2n \times 2n$ covariance matrix, \mathbf{S} , deviation vectors of each shape from the mean are calculated and assembled into the following form:

$$\mathbf{S} = \frac{1}{N} \sum_{i=1}^N d\mathbf{X}_i d\mathbf{X}_i^T \quad (4.4)$$

where $d\mathbf{X}_i = \mathbf{X}_i - \mathbf{X}_{mean}$ is the deviation vector for each shape. The eigenvectors of \mathbf{S} are the orthogonal components that span this space and their corresponding eigenvalues show how significant they are. The larger the eigenvalue, the more significant is its corresponding eigenvector. Hence, based on the eigenvalues of the shape space, the t most significant eigenvectors are adopted as the main modes of the shape space in Equation 4.2 such that the ratio of the sum of the corresponding t eigenvalues to the sum

of all eigenvalues is more than 0.99. The above equations can generate new examples of the shapes by varying the parameters (b_k) within suitable limits (Cootes et al. 1995):

$$-3\sqrt{\lambda_k} \leq b_k \leq +3\sqrt{\lambda_k} \quad (4.5)$$

where λ_k is the k^{th} eigenvalue of the shape set's covariance matrix.

4.2.3 Statistical Finite Element Model

Stiffness matrix computation and the solution to a linear or nonlinear system of equations are the most time-demanding part of FE analysis. However, for a set of similar body organs such as the prostate or the breast, the shape, tissue type distribution and their material properties have significant similarities in different individuals. Therefore, it is reasonable to assume that the stiffness matrix \mathbf{K} , thus the FE solution (e.g. displacement field) corresponding to an organ in a set of similar organs depends mainly on the organ's geometry. Finding a relationship between organ geometry and its corresponding FE solution can avoid performing tedious FE calculation for every shape in the class of body organs, paving the way for obtaining a reasonably accurate FE solution in real-time fashion. The complexity of the tissue's constitutive law incorporated in the FE analysis is expected to increase the complexity of the relationship between geometry and FE solution. As such, various function-fitting approaches such as neural network (NN) or PCA-based regression may be suitable for linking shape parameters and FE solution of a set of a particular body organ. One possible representation of geometry and FE solution is discretised shape outline and its corresponding 2D or 3D FE solution, respectively. However, due to the very large dimensions of input and output with this representation, a fitting function is unlikely to yield a reasonably accurate mapping function. Hence, we use PCA to reduce the dimensions of input and output and make them appropriate for fitting functions.

4.2.4 Formulation

In this paper, we introduce a novel technique which we refer to as statistical finite element method (SFEM). This technique is developed for tissue biomechanical analysis and is capable of estimating tissue deformation and stress field in real-time fashion. The

technique employs PCA to obtain a compact representation for the organ's shape and its corresponding FE solution. The essence of the proposed technique is that shapes of an organ set and their corresponding FE solutions pertaining to specific loading and boundary conditions can be related quantitatively. Hence, by assuming similar tissue biomechanical properties in a class of organs, the shape information of the object is sufficient to find its deformation and stress field under the specific loading and boundary conditions. This technique enables developing patient-specific body organ modelling where the organ undergoes similar type of loading such as loading associated with TRUS-guided prostate biopsy or breast biopsy.

To develop a relationship between organ set shapes and their FE solutions, we employed the PCA concept. In PCA of a shape set, each node in the discretised representation of the shape must correspond to a unique feature. Such feature can be derived from the anatomy of the organs. In the absence of such features or for simplicity, we obtain equivalent nodes throughout a body organ set by mapping each shape to a unique regular grid in the logical space using transfinite interpolation (TFI) [19]. TFI is straight forward to implement and only requires mapping the boundaries of the shape (physical space) to the sides of a unique square grid in the logical space. For the sake of simplicity, we use landmarks on the shape boundaries corresponding to points uniformly spaced on the square boundaries in the logical space. Hence, internal nodes are generated automatically using TFI blending functions [19]. In the presence of distinct landmarks or regions in the body organ shapes, other linear or nonlinear blending functions could be used to generate equivalent nodes throughout the body organ class.

As discussed earlier, the shape space is given by Equation 4.2. Similarly, using a common TFI-based FE mesh with quadrilateral elements, each shape can be discretised by m nodes and p elements. Hence, the 2D displacement field of each shape obtained from FE analysis can be represented by a single point in the $2m$ -D space as follows:

$$u_i = (u_{x,i1}, u_{y,i1}, u_{x,i2}, u_{y,i2}, \dots, u_{x,im}, u_{y,im})^T \quad i = 1, \dots, N \quad (4.6)$$

Similarly, the 2D stress field of each shape obtained from FE analysis can be represented by a single point in the $3p$ -D space as follows:

(4.7)

$$S_i = (S_{xx,i1}, S_{yy,i1}, S_{xy,i1}, S_{xx,i2}, S_{yy,i2}, S_{xy,i2}, \dots, S_{xx,ip}, S_{yy,ip}, S_{xy,ip})^T \quad i = 1, \dots, N$$

Similar to [18], we can assume that for a set of N shapes, there is an allowable shape domain in $2m$ -D principal component displacement space and in $3p$ -D principal component stress space to which an ellipsoid can be fitted. Each principal axes of this ellipsoid, which shows a mode of displacement or stress variation, can be calculated by employing PCA to the data. Therefore, the FE space can be defined as:

$$\mathbf{u} = \mathbf{u}_{mean} + \mathbf{Q}\mathbf{c} \quad (4.8)$$

$$\mathbf{S} = \mathbf{S}_{mean} + \mathbf{R}\mathbf{d} \quad (4.9)$$

where \mathbf{u}_{mean} is the mean vector of nodal displacements obtained from FE analysis of all shapes in the dataset, $\mathbf{c} = (c_1 \ c_2 \ \dots \ c_s)^T$ is a weight factor vector, and $\mathbf{Q} = (\mathbf{q}_1 \ \mathbf{q}_2 \ \dots \ \mathbf{q}_s)$ is the matrix of nodal displacements principal modes (major axes of the ellipsoid or the first s eigenvectors of the displacements covariance matrix) obtained by PCA. Similarly, \mathbf{S}_{mean} is the mean vector of element stress values obtained from the FE analysis of all shapes in the dataset, $\mathbf{d} = (d_1 \ d_2 \ \dots \ d_l)^T$ is a weight factor vector and $\mathbf{R} = (\mathbf{r}_1 \ \mathbf{r}_2 \ \dots \ \mathbf{r}_l)$ is the matrix of stress values corresponding to the first l principal modes. The covariance matrices can be obtained using an equation similar to Equation 4.4 for the displacement and stress vectors of each shape. Similar to SSMs, Equations 4.8 and 4.9 essentially represent statistical displacement and stress models, respectively. These equations can generate new examples of the displacement and stress fields by varying the parameters within suitable limits, similar to Equation 4.5:

$$-3\sqrt{\eta_k} \leq c_k \leq +3\sqrt{\eta_k} \quad (4.10)$$

$$-3\sqrt{\theta_k} \leq d_k \leq +3\sqrt{\theta_k} \quad (4.11)$$

where η_k is the k^{th} eigenvalue of the displacements covariance matrix and θ_k is the k^{th} eigenvalue of the stress covariance matrix.

4.2.5 Procedure

The fundamental assumption of SFEM is that a shape set corresponding to a sufficiently large number of objects is available. In medical applications, the objects refer to a number of shapes of a specific organ, e.g. prostate, breast or lung, which can be obtained by segmenting medical images of an organ acquired from different patients. This shape set will be used as a training set employed to predict the deformation and stress field of an organ of a patient not included in the set. Our proposed technique for tissue displacements and stress calculation of this organ involves two steps: a pre-processing step to determine a shape space-FE space relationship followed by displacement and stress fields calculation step using the obtained relationship. In the first step, we perform PCA analysis on the given shape set via Equation 4.2 to determine vector \mathbf{b} of each organ shape in the set. Note that equivalent landmarks must be employed for outlining the shapes at this step. Next, as described earlier, a common TFI-based FE mesh is used to perform FE analysis on each organ shape in the training set. The loading and boundary conditions of the FE model of each organ in the set correspond to a specific medical procedure such as US probe contact loading in prostate TRUS. After conducting FE analysis for each object undergoing the loading of interest, PCA is carried out to obtain the main modes of deformation and stress (\mathbf{Q} and \mathbf{R}) and weight factors (\mathbf{c} and \mathbf{d}) needed in Equations 4.8 and 4.9.

For a new shape not included in the training set, \mathbf{b}_{new} , the weight vector of the new shape can be calculated easily by either obtaining the least squares solution of Equation 4.2 or by employing active shape models [18]. If the new shape has already been outlined by equivalent landmarks (similar to those used with the training data-set), the weight vector \mathbf{b}_{new} can be found by obtaining the least squares solution to Equation 4.2 as follows:

$$\mathbf{b}_{\text{new}} = \mathbf{P}^+(\mathbf{x}_{\text{new}} - \mathbf{x}_{\text{mean}}) \quad (4.12)$$

where \mathbf{P}^+ is the pseudo inverse matrix of \mathbf{P} . Otherwise, if the new shape is a new medical image of a body organ of a patient, it can be simply segmented by the Active Shape Model technique [18] paving the way for \mathbf{b}_{new} direct calculation.

To find the displacement field corresponding to this object, only \mathbf{c}_{new} , the displacement weights vector of the new shape, needs to be determined before substitution in Equation 4.8. Similarly, to find the stress field corresponding to this object, only \mathbf{d}_{new} , the stress weights vector of the new shape, needs to be determined before substitution in Equation 4.9. Tissue displacement and stress fields depend on both the organ shape and its tissue mechanical properties. We use \mathbf{M} as the vector that contains the organ tissues' mechanical properties. \mathbf{M} would contain Young's modulus values or hyperelastic parameters of the tissues depending on the tissue models used in the FE model. Therefore, to account for tissue properties dependence in \mathbf{c}_{new} and \mathbf{d}_{new} calculation, we establish a relationship between the augmented vectors $[\mathbf{b} \ \mathbf{M}]$ and their corresponding FE solution space characterized by $[\mathbf{c} \ \mathbf{d}]$.

As can be seen, although FE and PCA in the preprocessing step are computation demanding, the step of the new shape's displacement field calculation is very fast as it involves a simple linear least square calculation or real-time active shape analysis [18] followed by simple substitution in Equation 4.8 or Equation 4.9. Note that unlike the displacement or stress field calculation step, which needs to be carried out very fast in real-time biomedical applications, the pre-processing step's speed is not critical and can be carried out offline. Although the methodology of the proposed SFEM technique is general and can handle inhomogeneous organs, only homogenous objects are presented in this work.

4.2.6 Fitting Function Approaches

The key step in the proposed technique is fitting a relationship between the compact representation of geometry (\mathbf{b}) and the FE fields (\mathbf{c} and \mathbf{d}). While various techniques exist for data fitting, we explored two different techniques described in Sections 4.2.6.1 and 4.2.6.2.

4.2.6.1 Multilayer NN

As discussed earlier, we use NN to relate shape and FE solution throughout a data-set of object class. Again, the shape is characterised by vector \mathbf{b} and FE fields are characterised by vectors \mathbf{c} and \mathbf{d} . The NN we used for this purpose is a multilayer feed-forward back-

propagation NN. In general, multilayer feed-forward NNs (FF-NN) [20] are widely used in function approximation applications. Such networks consist of an input layer, which conducts the inputs to the next layer, a number of hidden layers and an output layer. Hidden and output layers include a number of neurons. Each neuron receives a number of weighted inputs as well as a bias and yields an output. To compute its output, each neuron uses a transfer function over the sum of its weighted inputs and bias. During the training phase, the network finds an optimum mapping relationship between the input and output vectors using training samples, i.e. a number of input vectors and their corresponding output vectors. This is carried out by the network through adjusting its neurons' weights and bias values to minimise the differences between the network's known responses to their respective input samples. The most common training algorithm used in FF-NN is the back-propagation algorithm, which is based on the gradient descent method. The term back-propagation refers to the manner in which the gradient is computed for nonlinear multilayer networks. In the simulation phase, the trained network responds to new input vectors based on its knowledge achieved during the training phase to produce the output. In this study, a four-layer feed-forward back-propagation NN was applied for function approximation. The NN's topology was chosen such that the input layer has the size of input vector $[\mathbf{b} \ \mathbf{M}]$ with two hidden layers consisting of 15 neurons each in addition to the output layer. The output layer includes as many neurons as the size of output vector $[\mathbf{c} \ \mathbf{d}]$. All the neurons used tangent-sigmoid as their transfer function except the neurons of output layer that have a linear transfer function.

4.2.6.2 PCA-based Technique

Another approach to establish a relationship between $[\mathbf{b} \ \mathbf{M}]$ and $[\mathbf{c} \ \mathbf{d}]$ is to find a linear regression between them based on PCA. In this approach, the input and output are assembled in one vector \mathbf{a} :

$$\mathbf{a}_i = [\mathbf{b}_i \ \mathbf{M}_i \ \mathbf{c}_i \ \mathbf{d}_i] \quad i = 1, \dots, N \quad (4.13)$$

Applying PCA to \mathbf{a} leads to a compact representation of $[\mathbf{b} \ \mathbf{M}]$ and $[\mathbf{c} \ \mathbf{d}]$ as follows:

$$\mathbf{a} = \mathbf{a}_{\text{mean}} + \mathbf{S}\mathbf{e} \quad (4.14)$$

where \mathbf{e} is a weight factor vector, \mathbf{S} is the matrix of the first u principal modes and \mathbf{a}_{mean} is the mean vector of all \mathbf{a} vectors. Alternatively, we can rewrite Equation 2.14 in terms of \mathbf{b} , \mathbf{M} , \mathbf{c} and \mathbf{d} and their associated matrices \mathbf{S}_b , \mathbf{S}_M , \mathbf{S}_c and \mathbf{S}_d as:

$$\begin{Bmatrix} \mathbf{b} \\ \mathbf{M} \\ \mathbf{c} \\ \mathbf{d} \end{Bmatrix} = \begin{Bmatrix} \mathbf{b}_{\text{mean}} \\ \mathbf{M}_{\text{mean}} \\ \mathbf{c}_{\text{mean}} \\ \mathbf{d}_{\text{mean}} \end{Bmatrix} + \begin{Bmatrix} \mathbf{S}_b \\ \mathbf{S}_M \\ \mathbf{S}_c \\ \mathbf{S}_d \end{Bmatrix} \mathbf{e} \quad (4.15)$$

For any new shape with \mathbf{b}_{new} as its geometry vector and \mathbf{M}_{new} as its mechanical properties, \mathbf{e}_{new} can be found using the first two rows of Equation 4.15 using a least squares solution, if the system of equations is not underdetermined:

$$\begin{Bmatrix} \mathbf{b}_{\text{new}} \\ \mathbf{M}_{\text{new}} \end{Bmatrix} = \begin{Bmatrix} \mathbf{b}_{\text{mean}} \\ \mathbf{M}_{\text{mean}} \end{Bmatrix} + \begin{Bmatrix} \mathbf{S}_b \\ \mathbf{S}_M \end{Bmatrix} \mathbf{e}_{\text{new}} \quad (4.16)$$

In other words, to have a unique solution to Equation 4.16, the size of \mathbf{e} must be equal to or smaller than $[\mathbf{b} \ \mathbf{M}]$. Therefore, the first u eigenvectors of the covariance matrix of vectors \mathbf{e} used in Equation 4.14 must be chosen such that not only should it reproduce the majority of the variance of \mathbf{e} but also must have a size smaller than the size of vector $[\mathbf{b} \ \mathbf{M}]$. After obtaining \mathbf{e}_{new} , \mathbf{c}_{new} and \mathbf{d}_{new} can be found readily from Equation 4.15 as follows:

$$\mathbf{c}_{\text{new}} = \mathbf{c}_{\text{mean}} + \mathbf{S}_c \mathbf{e}_{\text{new}} \quad (4.17)$$

$$\mathbf{d}_{\text{new}} = \mathbf{d}_{\text{mean}} + \mathbf{S}_d \mathbf{e}_{\text{new}} \quad (4.18)$$

4.3 Results

To demonstrate the performance of the proposed technique, we present an *in silico* study of prostate deformation under TRUS loading. The techniques described above have been used to generate point distribution models for numerical 2D prostate phantoms in both shape and FE spaces. To demonstrate the capabilities of the proposed technique, four different FE analysis types were used in the pre-processing step. Results corresponding to each FE model are presented in the following sections. Although the proposed method (SFEM) requires having the same tissue constitutive law for all objects in both the pre-

processing step and the deformation calculation step, it will be shown that accurate results are still achieved for organs consisting of tissues with significantly different mechanical properties.

4.3.1 Dataset

To evaluate the proposed technique *in silico*, a database of 500 prostate configurations was produced. This dataset covers prostate sizes vary from a walnut size (typical healthy prostate size) to sizes 5 times bigger than normal (elderly cases with BPH). It also considers prostate shape variation among different individuals using prostate shapes segmented from 86 TRUS images. To consider uncertainty and inter-patient variability in tissue elastic properties, we used a range of elastic or hyperelastic parameter values of (mean \pm 0.25 \times mean) which implies an uncertainty in the elastic or hyperelastic properties as much as 25% of the mean values. For the linear elastic tissue models, we used Young's modulus value of 55 kPa, which matches the values reported in Krouskop et al. [21] for the prostate. Considering a variation of 25%, this value leads to a range of 41 kPa $<$ E $<$ 69 kPa. Similarly for the hyperelastic FE models, we used Yeoh model hyperelastic parameter values of $C_{10} = 5.74 \times 10^{-3}$; $C_{20} = 3.57 \times 10^{-1}$ and $C_{30} = 2.05 \times 10^{-3}$. With a STD value of 25% of the mean values, this leads to $4.31 \times 10^{-3} < C_{10} < 7.17 \times 10^{-3}$; $2.68 \times 10^{-1} < C_{20} < 4.46 \times 10^{-1}$ and $1.54 \times 10^{-3} < C_{30} < 2.56 \times 10^{-3}$. Unit of these parameters is N/mm².

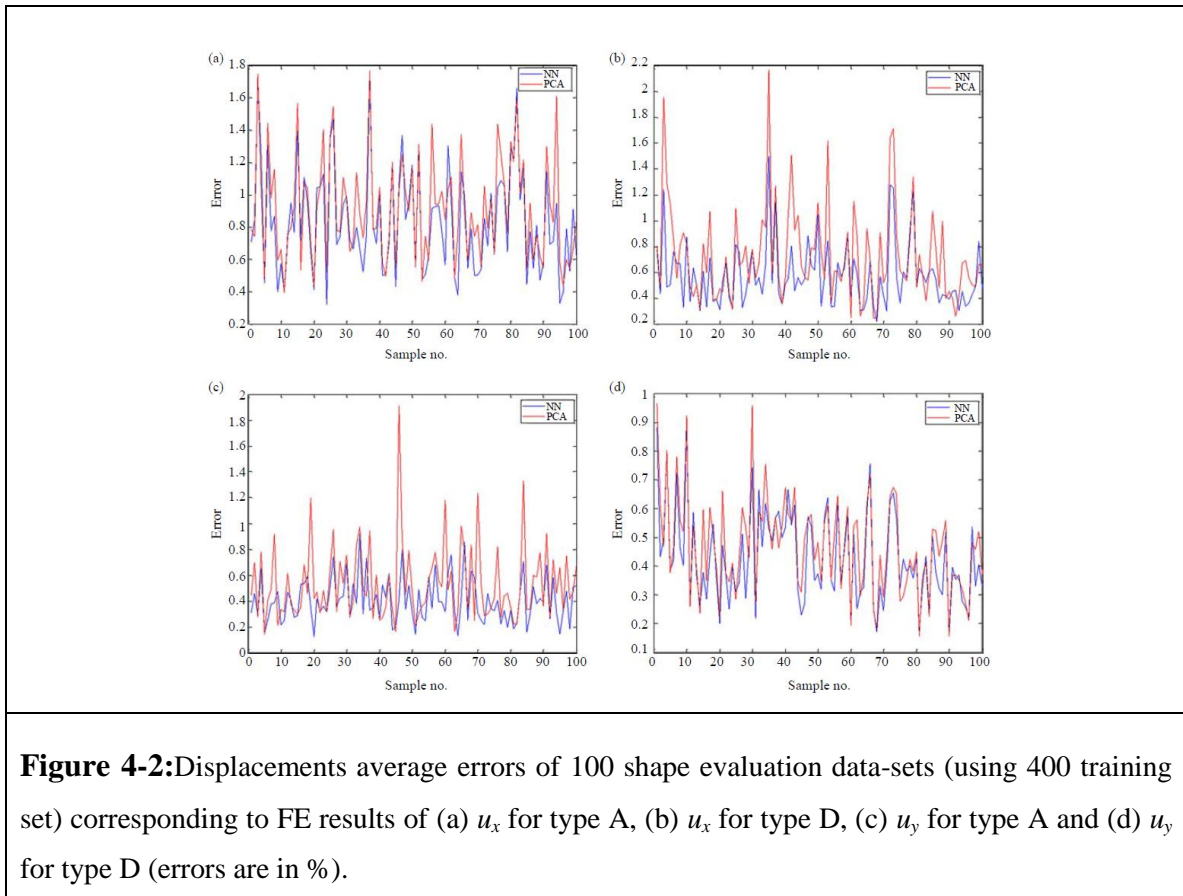
4.3.2 SFEM Evaluation

FE analysis was performed on each generated prostate shape of dataset. Here, we performed the following four different FE analysis types using ABAQUS FE software package (SIMULIA, Dassault Systemes, RI, USA):

- (1) Linear elastic material with moving nodes on the curve in the model that simulates US probe loading in TRUS and fixed nodes elsewhere on the boundary where the loading area is far enough (analysis type A).
- (2) Hyperelastic material with moving nodes on the curve in the model and fixed nodes elsewhere on the boundary where the loading area is far enough (analysis type B).

- (3) Linear elastic material with contact problem at the bottom that simulates a prostate contact loading of US probe in TRUS procedure more accurately (analysis type C).
- (4) Hyperelastic material with contact problem at the bottom (analysis type D).

The boundary conditions used in the above models are illustrated schematically in Figure 4.1.c. The fitting functions were then trained with 400 out of the 500 samples. One hundred additional samples were used to test the mapping function. Results were validated by FE analysis results obtained by ABAQUS. Figures 4.2 and 4.3 show results obtained from this analysis using two different fitting functions for u_x , u_y , σ_{xx} and σ_{yy} , respectively. These figures depict displacement and stress average errors for all the shape evaluation data-sets corresponding to FE analysis of two analysis types A and D explained earlier. These analysis types represent the least and the most complex types of analysis given in this investigation. The results are also summarised in Tables 4.1-4.4. These results show very good agreement between SFEM and FEM.



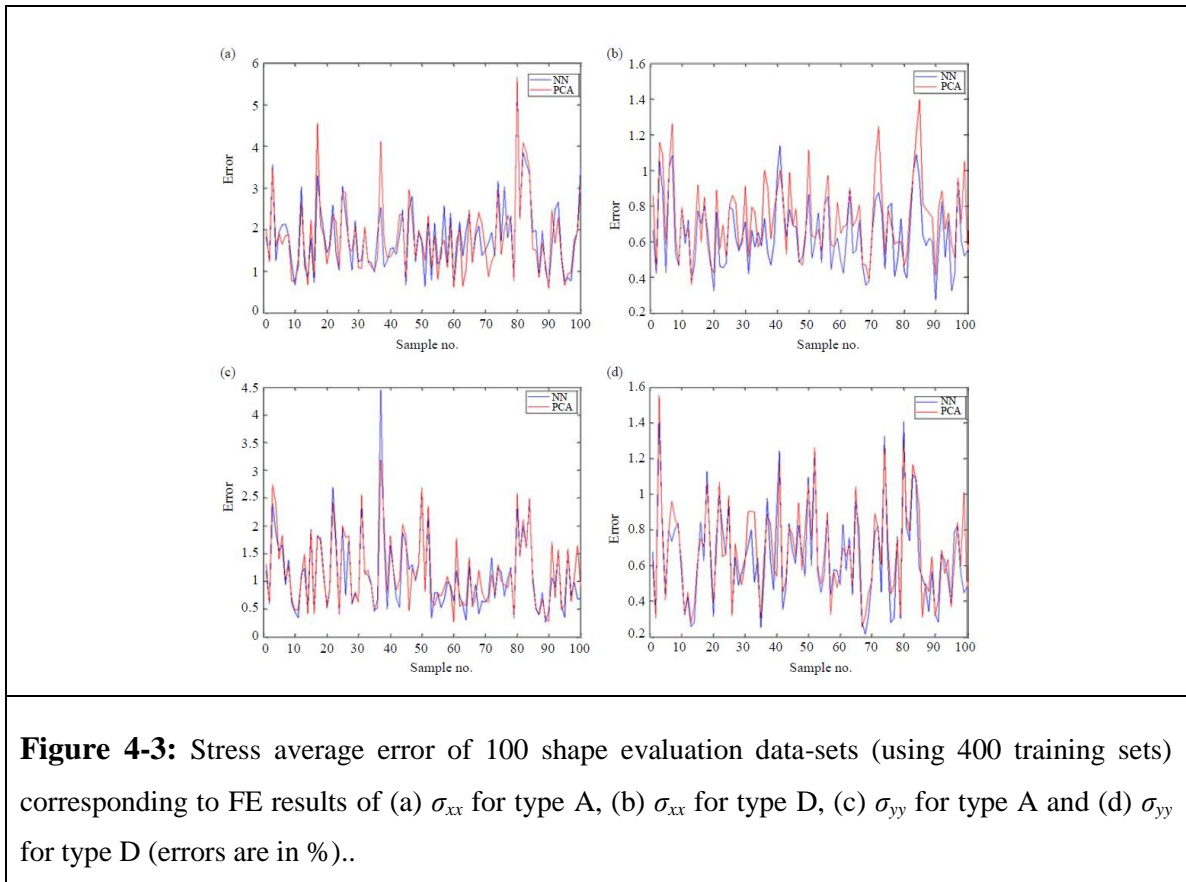


Table 4-1: Mean and max average of values of u_x errors per node for 100 shape evaluation data.

Type of Analysis	Mean \pm std of average error per node		Max of average error per node	
	NN	PCA	NN	PCA
A	$0.83 \pm 0.31\%$	$0.91 \pm 0.32\%$	1.72%	1.76%
B	$0.57 \pm 0.21\%$	$1.35 \pm 1.50\%$	1.37%	10.46%
C	$0.66 \pm 0.23\%$	$1.24 \pm 0.75\%$	1.55%	4.53%
D	$0.57 \pm 0.24\%$	$0.73 \pm 0.36\%$	1.50%	2.16%

Table 4-2: Mean and max average of values of u_y errors per node for 100 shape evaluation data.

Type of Analysis	Mean \pm std of average error per node		Max of average error per node	
	NN	PCA	NN	PCA
A	0.40 \pm 0.17%	0.53 \pm 0.29%	0.91%	1.9%
B	0.28 \pm 0.10%	0.45 \pm 0.40%	0.57%	2.79%
C	0.53 \pm 0.30%	1.09 \pm 0.73%	1.73%	5.25%
D	0.42 \pm 0.15%	0.47 \pm 0.16%	0.90%	0.96%

Table 4-3: Mean and max average of values of σ_{xx} errors per node for 100 shape evaluation data.

Type of Analysis	Mean \pm std of average error per node		Max of average error per node	
	NN	PCA	NN	PCA
A	1.82 \pm 0.89%	1.80 \pm 0.89%	5.55%	5.66%
B	1.19 \pm 0.52%	1.66 \pm 1.12%	2.70	7.71%
C	1.53 \pm 0.66%	2.15 \pm 0.98%	3.59	5.48%
D	0.64 \pm 0.18%	0.73 \pm 0.21%	1.13	1.39%

Table 4-4: Mean and max average of values of σ_{yy} errors per node for 100 shape evaluation data.

Type of Analysis	Mean \pm std of average error per node		Max of average error per node	
	NN	PCA	NN	PCA
A	1.11 \pm 0.67%	1.16 \pm 0.65%	4.44%	3.18%
B	1.49 \pm 0.84%	1.64 \pm 0.96%	3.70%	5.09%
C	1.29 \pm 0.74%	1.56 \pm 0.77%	3.87%	3.63%
D	0.64 \pm 0.26%	0.68 \pm 0.25%	1.41%	1.55%

To demonstrate the accuracy of the proposed technique, Figures 4.4-4.7 depict the displacement and stress results obtained by SFEM and by ABAQUS for one of the randomly generated shapes with equitable average errors. In these sample results, the displacements are shown for analysis type D; whereas the stresses are shown for analysis type C among the investigated analysis types. According to the difference images, there is a very good agreement between FE field and its counterpart estimated from our method.

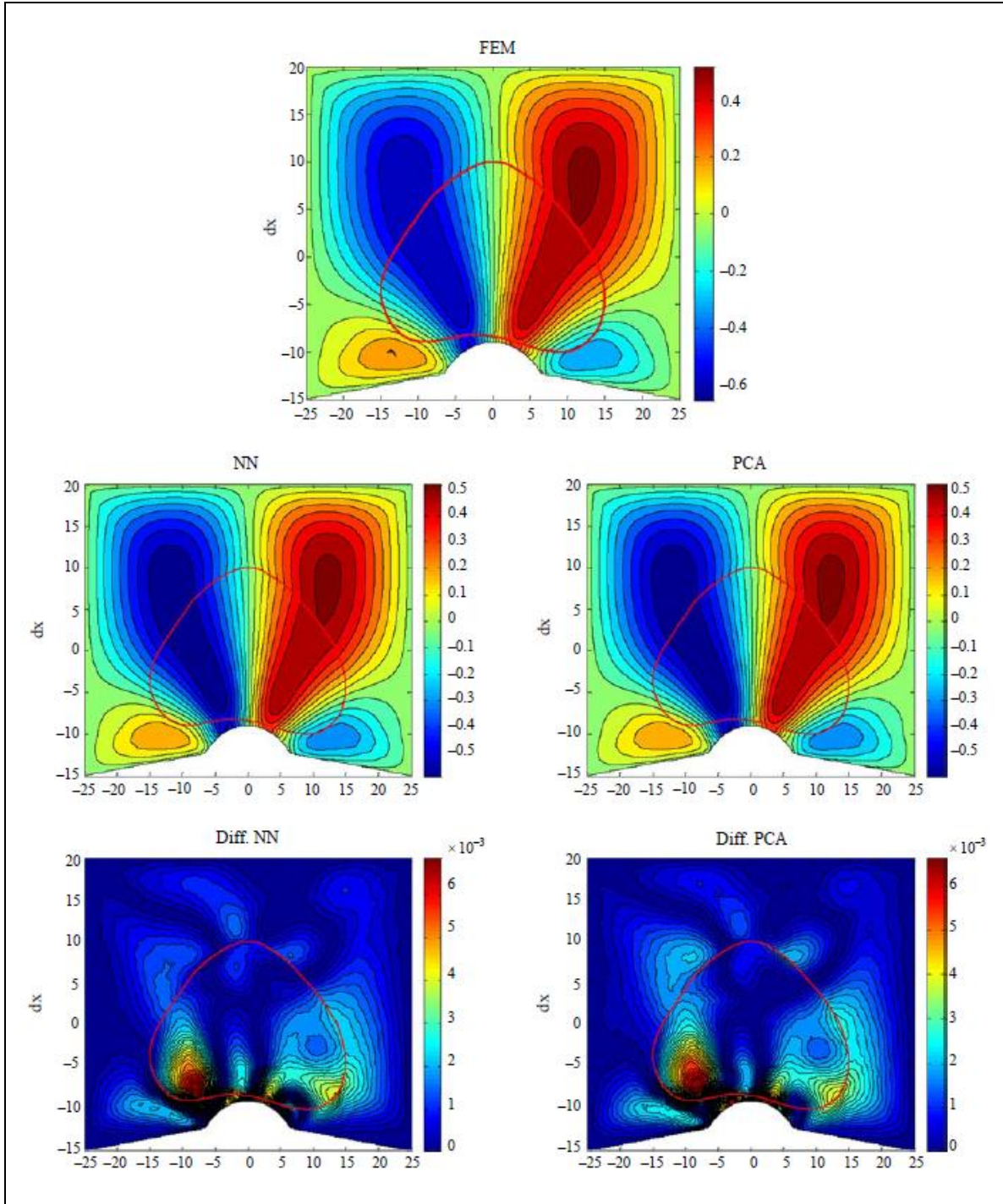


Figure 4-4: u_x field of FEM, NN and PCA and their differences for analysis type D (values of color bar are in mm).

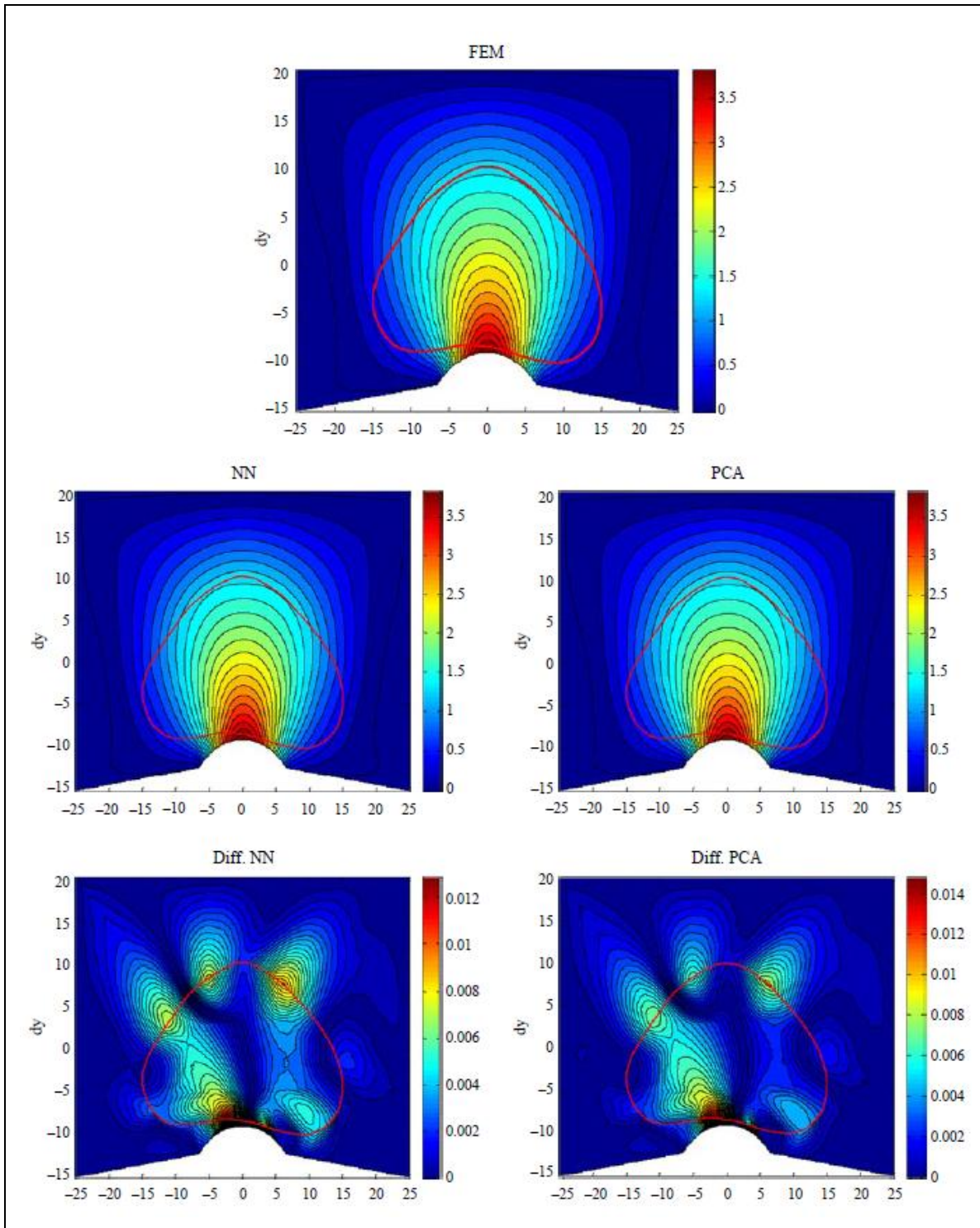
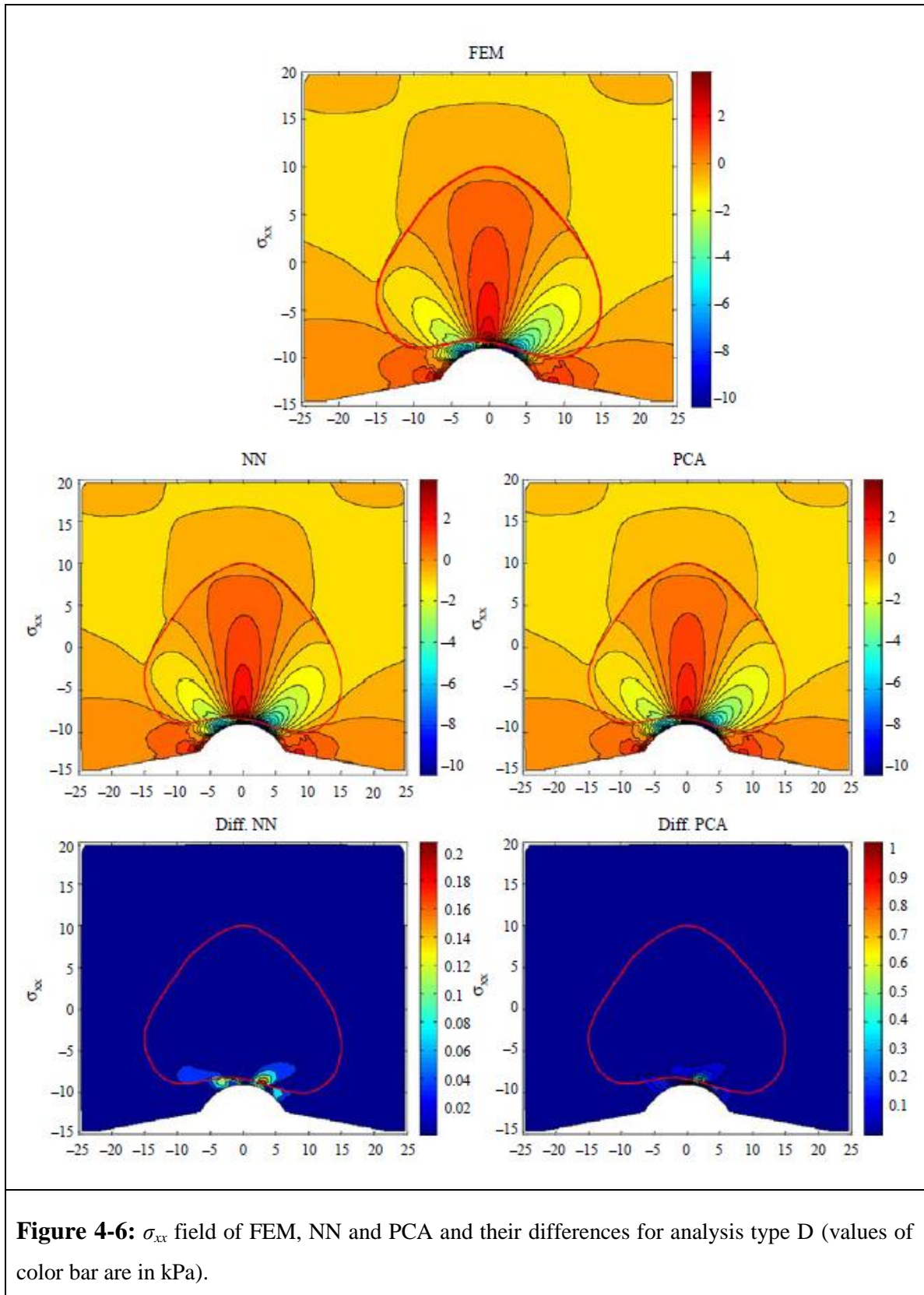


Figure 4-5: u_y field of FEM, NN and PCA and their differences for analysis type D (values of color bar are in mm).



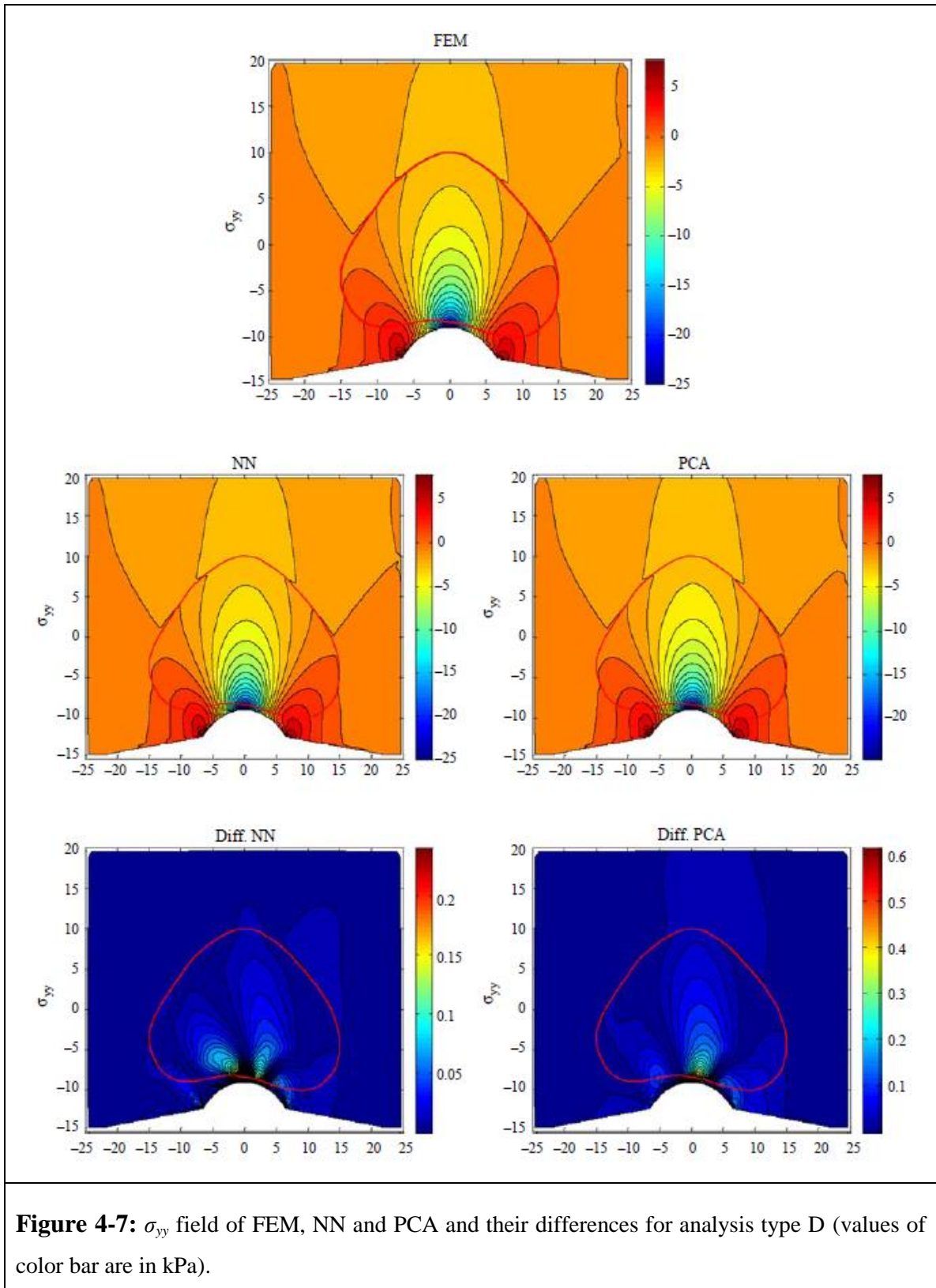


Figure 4-7: σ_{yy} field of FEM, NN and PCA and their differences for analysis type D (values of color bar are in kPa).

In all cases, the SFEM analysis took less than 0.1 s using a regular desktop computer (AMD Athlon 64 X2 dual core processor of 2.4 GHz with 3GB RAM). This implies computation speed ratios of more than 100 corresponding to all analysis types. The ratio of processing time of ABAQUS to the processing time of the proposed SFEM is reported in Table 4.5.

Table 4-5: The ratio of the processing time of ABAQUS to the processing time of SFEM.

Type of Analysis	Ratio of ABAQUS processing time to SFEM processing time
A	$8/0.07 \approx 114$
B	$10/0.07 \approx 143$
C	$12/0.07 \approx 171$
D	$14/0.07 \approx 243$

4.4 Discussion and Conclusions

In this paper, we propose a novel fast FE-based technique (SFEM) for estimating biological tissue deformation under specified loading conditions. The technique combines preprocessed data obtained by accurate FE analysis via PCA and SSM frameworks. The essence of the proposed method is that it establishes an effective interpolation function to relate the two spaces of an organ set geometry and its corresponding FE solutions. Due to the large number of variables required to define the geometry and FE spaces, PCA was employed to reduce the problem dimensions by projecting both the geometry and FE spaces on their respective main basis. The resulting mathematically compact models were then interrelated via a fitting function. Two different fitting functions, namely NN and PCA, were used in this study to demonstrate the effectiveness of the technique in tissue deformation and stress estimation. The proposed approach is very effective for diagnostic and interventional procedures where an organ undergoes a specific clinical procedure.

For example, in prostate TRUS procedure the prostates undergo similar loading characteristics; hence the procedure can be modelled effectively using the proposed technique. In terms of mechanical modelling, models simulating organs undergoing similar procedures typically involve similar boundary and loading conditions. As such, medical images of such organs can be used effectively in conjunction with the proposed SFEM technique to find their deformed shape in real-time. Although the proposed technique is ideal for such cases, it is not limited to situations where the loading characteristics are fully known *a priori*. If loading conditions are not fully known *a priori*, the final deformed shape can be obtained using the superposition principle which combines SFEM analysis results corresponding to a set of unit displacement or force boundary conditions.

PCA is widely utilised in model order reduction techniques. In the study of Davatzikos et al. [22], the principal modes of covariation between shape and possible deformation were found from training data-set, by applying PCA to obtain the most likely deformation of the individual anatomy. Similarly, PCA was used to obtain covariation between shape and forces causing deformation. This was followed by the FE analysis to calculate deformed anatomy of a patient. Although the latter technique outperformed the former, it still required costly FE calculation, which is expected to be extensive especially in three dimensions. Mohamed et al. [23] used PCA to extract the main modes of deformation of a prostate under TRUS probe insertion. A third-degree Bernstein polynomial was then sought to approximate the principal modes of deformation as a function of the probe insertion angles and depth. Apart from sources of errors such as Bernstein polynomial approximation and finite number of deformation modes, shape variability and different material parameters were not considered in their work. In the study by Hu et al. [24], the same procedure was followed while material properties were also included as variable parameters. The deformable gland model was then registered to the target surface points by optimising the weights of the principal modes of variation of the statistical motion model. Again, shape variability was not considered in that approach. He et al. [25] employed PCA on FE simulation of soft tissue deformation due to bone-related effects for different surgical plans. In their approach, they estimated the tissue boundary displacements and incorporated them in FE model to find the tissue's deformed shape.

Once again, this approach only accounts for one patient (one shape) and for any new patient the whole FE analyses must be performed, hence precluding the possibility of adapting it in real-time analysis.

The proposed technique is both very fast and highly accurate for calculating both displacement and stress fields of tissues. Although the proposed technique is very fast (real-time or near real-time), more importantly, its speed does not depend on the complexity of the FE model used in the pre-processing procedure. In other words, after completing the training step, the technique always takes the same amount of time to calculate the displacement and stress fields irrespective of the complexity of the tissue's constitutive law or boundary conditions. With an ordinary desktop computer, it takes less than 0.1 s to perform SFEM and output the displacement or stress field of a typical 2D model. In the pre-processing step, depending on the application, a specific FE model is used with the shape dataset; e.g. linear elastic, hyperelastic and contact problem in conjunction with linear elastic or hyperelastic materials. However, the more nonlinearity involved in the FE analysis, the more complex the fitting function may have to be. The SFEM method also has a good potential to be implemented in applications such as VR environments used for surgery training, computer-assisted surgery and brachytherapy procedures, and elastography where real-time simulation is required. Results obtained from the SFEM analysis of biomechanical problems with various levels of complexity were presented. The application of this technique in an iterative elastography reconstruction technique was demonstrated in [26]. Such applications, where a large number of FE analyses are involved, can benefit tremendously from the proposed SFEM technique to speed up the respective computation process.

The method has been evaluated for four different analyses types, i.e. linear elastic, hyperelastic and contact problem in conjunction with linear elastic and with hyperelastic materials. The highly accurate results obtained for numerically generated 2D shapes are encouraging and indicate the method's excellent potential for application in many biomedical applications such as computer-assisted diagnosis and intervention where real-time tissue deformation calculation is required. Other examples of such applications include the development of VR environments used for training surgeons and radiologists,

surgery planning and elastography reconstruction techniques. Further work is under way for extending this technique to heterogeneous tissues (e.g. organs with tumours). In this case, the tumour tissue has different mechanical properties from those of the organ's normal tissue. Although a 2D implementation of this technique was presented in this study, the technique is general and its 3D implementation follows the same principles and is straightforward. In fact, the value of this technique would be realised even further when applied to 3D cases since the time required to output 3D displacement fields is expected to be in the same order of the ~ 0.1 s that the 2D cases took in this investigation. This implies that the speed ratio of the proposed SFEM to the conventional FE methods is expected to be significantly larger for 3D models.

References

- [1] H. Delingette, "Toward realistic soft-tissue modeling in medical simulation," Proc IEEE, vol. 86, no.3, pp. 512-523, 1998.
- [2] R. M. Satava, "Medical virtual reality. The current status of the future," Stud Health Technol Inform, vol. 29, pp.100-106, 1996.
- [3] A. Nealen, M. Muller, R. Keiser, E. Boxerman and M. Carlson, "Physically based deformable models in computer graphics," Comput Graph Forum, vol. 25, no.4, pp. 809-836, 2006.
- [4] G. Bianchi, B. Solenthaler, G. Szekely and M. Harders, "Simultaneous topology and stiffness identification for mass-spring models based on FEM reference deformations," Lecture Notes in Computer Science, vol. 3217, pp. 293-301, 2004.
- [5] B. A. Lloyd, G. Szekely and M. Harders, "Identification of spring parameters for deformable object simulation," IEEE Trans Visual Comput Graph, vol. 13, no. 5, pp. 1081-1093, 2007.
- [6] M. A. Sagar, D. Bullivant, G. D. Mallinson, P. J. Hunter and I. W. Hunter, "A virtual environment and model of the eye for surgical simulation," Proceedings of the 21st Annual Conference on Computer Graphics and Interactive Techniques, Orlando, FL, USA, pp. 205-212, 1994.
- [7] M. Bro-Nielsen, "Medical image registration and surgery simulation," PhD dissertation, Department of Informatics and Mathematical Modeling, Technical University of Denmark, 1997.
- [8] K. H. Huebner, D. L. Dewhurst, D. E. Smith and T. G. Byrom, The finite element method for engineers, 4th ed., New York (NY): Wiley, 2008.
- [9] M. Bro-Nielsen and S. Cotin, "Real-time volumetric deformable models for

- surgery simulation using finite elements and condensation,” *Comput Graph Forum.*, vol. 15, no. 3, pp.57-66, 1996.
- [10] S. Cotin, H. Delingette and N. Ayache, “Real-time elastic deformations of soft tissues for surgery simulation,” *IEEE Trans Visual Comput Graph*, vol. 5, no. 1, pp. 62-73, 1999.
- [11] S. Cotin, H. Delingette and N. Ayache, “Hybrid elastic model for real-time cutting, deformations, and force feedback for surgery training and simulation,” *Visual Comput.*, vol. 16, no. 8, pp. 437-452, 2000.
- [12] O. Farle, V. Hill, P. Ingelstrom and R. Dyczij-Edlinger, “Multiparameter polynomial order reduction of linear finite element models,” *Math Comput Model Dyn Syst.*, vol. 14, no. 5, pp. 421-434, 2008.
- [13] P. Krysl, S. Lall and J. E. Marsden, “Dimensional model reduction in non-linear finite element dynamics of solids and structures,” *Int J Numer Methods Eng.*, vol. 51, no. 4, pp.479-504, 2001.
- [14] S. Lall, P. Krysl and J. E. Marsden, “Structure-preserving model reduction for mechanical systems,” *Physica D.*, vol. 184, no. 1-4, pp. 304-318, 2003.
- [15] J. Barbic and D. L. James, “Real-time subspace integration for St. Venant-Kirchhoff deformable models,” *ACM Transactions on Graphics*, Los Angeles, California, USA, 2005.
- [16] G. Rozza, D. B. P. Huynh and A. T. Patera, “Reduced basis approximation and a posteriori error estimation for affinely parametrized elliptic coercive partial differential equations-Application to transport and continuum mechanics,” *Arch Comput Methods Eng.*, vol. 15, no. 3, pp.229-275, 2007.
- [17] R. Milani, A. Quarteroni and G. Rozza, “Reduced basis method for linear elasticity problems with many parameters,” *Comput Methods Appl Mech Eng.*, vol. 197, no.51-52, pp. 4812-4829, 2008.
- [18] T. F. Cootes, C. J. Taylor, D. H. Cooper and J. Graham, “Active shape models - their training and application,” *Comput Vis Image Understand*, vol. 61, no. 1, pp. 38-59, 1995.
- [19] P. M. Knupp and S. Steinberg, *Fundamentals of grid generation*, Boca Raton (FL): CRC Press, pp. 18–23, 1993.
- [20] N. Toda, K. I. Funahashi and S. Usui, “Polynomial functions can be realized by finite size multilayer feedforward neural networks,” *IEEE Int Joint Conf Neural Netw*, Singapore, vol. 1, pp.343-348, 1991.
- [21] T. A. Krouskop, T. M. Wheeler, F. Kallel, B. S. Garra and T. Hall, “Elastic moduli of breast and prostate tissues under compression,” *Ultrason Imaging*, vol. 20, no.4, pp.260-274, 1998.
- [22] C. Davatzikos, D. Shen, A. Mohamed and S. K. Kyriacou, “A framework for predictive modeling of anatomical deformations,” *IEEE Trans Med Imaging*,

vol. 20, no. 8, pp.836-843, 2001.

- [23] A. Mohamed, C. Davatzikos and R. Taylor, "A combined statistical and biomechanical model for estimation of intra-operative prostate deformation," MICCAI, vol. 2489, pp.452-460, 2002.
- [24] Y. Hu, D. Morgan, H. U. Ahmed, D. Pendse, M. Sahu, C. Allen, M. Emberton, D. Hawkes and D. Barratt, "A statistical motion model based on biomechanical simulations for data fusion during image-guided prostate interventions," MICCAI, vol. 11, pp. 737-744, 2008.
- [25] Q. He, J. Feng, H. H. S. Ip, J. Xia and X. Cao, "An integration of statistical deformable model and finite element method for bone-related soft tissue prediction in orthognathic surgery planning," LNCS, vol. 5128, pp. 31-39, 2008.
- [26] I. Khalaji, K. Raahemifar and A. Samani, "Accelerated statistical shape model-based technique for tissue deformation estimation," SPIE Med Imag Conf, Florida, USA, 2009.

Chapter 5

Towards Ultrasound Probe Positioning Optimization During Prostate Needle Biopsy Using Pressure Feedback

*The material presented in this chapter has been published in International Journal of Computer Assisted Radiology and Surgery, 8(6):1053-1061 (2013).**

5.1 Introduction

Prostate cancer is the most frequently diagnosed cancer in Canadian males and is the third most common cause of death due to cancer in men (after lung and colorectal cancer) [1]. The earliest and least invasive tests for prostate cancer detection are prostate-specific antigen (PSA) blood test and digital rectal examination (DRE). These methods are known to have low sensitivity and specificity [2]. An alternate imaging method for prostate cancer detection is elastography which utilizes variations in tissue stiffness as contrast mechanism. This method is based on the fact that prostate tissue stiffness alteration is associated with pathology [3, 4]. Several research groups have developed transrectal

* © 2013 Springer. This modified version has been reprinted, with permission, from S. R. Mousavi, K. Raahemifar, S. Pautler and A. Samani, "Towards ultrasound probe positioning optimization during prostate needle biopsy using pressure feedback," International Journal of Computer Assisted Radiology and Surgery, April 2013.

ultrasonography techniques to investigate elastography effectiveness for prostate cancer diagnosis [5–7]. They concluded that elastography can potentially lead to prostate cancer detection and diagnosis with a high sensitivity and specificity. However, the current clinical gold standard for prostate cancer diagnosis is prostate needle biopsy. Prostate needle biopsy is administered if the PSA and or DRE tests lead to prostate cancer suspicion [8]. It involves removing six to eighteen samples from the upper, mid, and lower regions of the prostate capsule including its left and right sides. This is necessary to obtain a representative sample of the gland and determine the degree and extent of prostate cancer [9]. Transrectal Ultrasound (TRUS) is the most commonly used urologic imaging modality which is currently utilized for needle guidance during prostate biopsy. Although TRUS-guided prostate biopsy is a real-time, relatively low cost and easy to use procedure, it only provides limited amount of information to the physician for accurately guiding the needles to suspicious locations within the prostate capsule, leading to low sensitivity of ~60% and very low positive predictive value of only ~25% [10]. This issue leads to excessive number of biopsies that is undesirable since prostate biopsies are associated with discomfort in addition to a number of side effects such as hematuria (blood in urine), hematospermia (blood in semen), rectal bleeding, and infection. Therefore, reducing the number of biopsies is of great interest. In order to improve needle biopsy accuracy, suspicious areas should be determined precisely in advance, and a system should be designed to guide the needle to those areas with high precision. One approach for achieving this is to register preoperative 3D TRUS or MR image, in which tumors and other suspicious areas are visible, to intra-operative 2D TRUS images.

Boris et al. [11] developed a prostate biopsy system that integrates pre-interventional multi-parametric MR imaging with peri-interventional ultrasound. They showed that lesion targeted cores had a significantly higher positivity rate than non-targeted cores. To achieve a similar purpose, De Silva et al. [12] developed a mechanically assisted 3D ultrasound guided prostate biopsy system in which a preoperative 3D ultrasound image was registered to intra-operative 2D ultrasound images. Another clinical application that involves MRI imaging for planning followed by intra-operative ultrasound imaging fused with MRI is prostate brachytherapy which is used to treat prostate cancer [13, 14]. In this application, the radioactive seeds need to be positioned within the prostate capsule

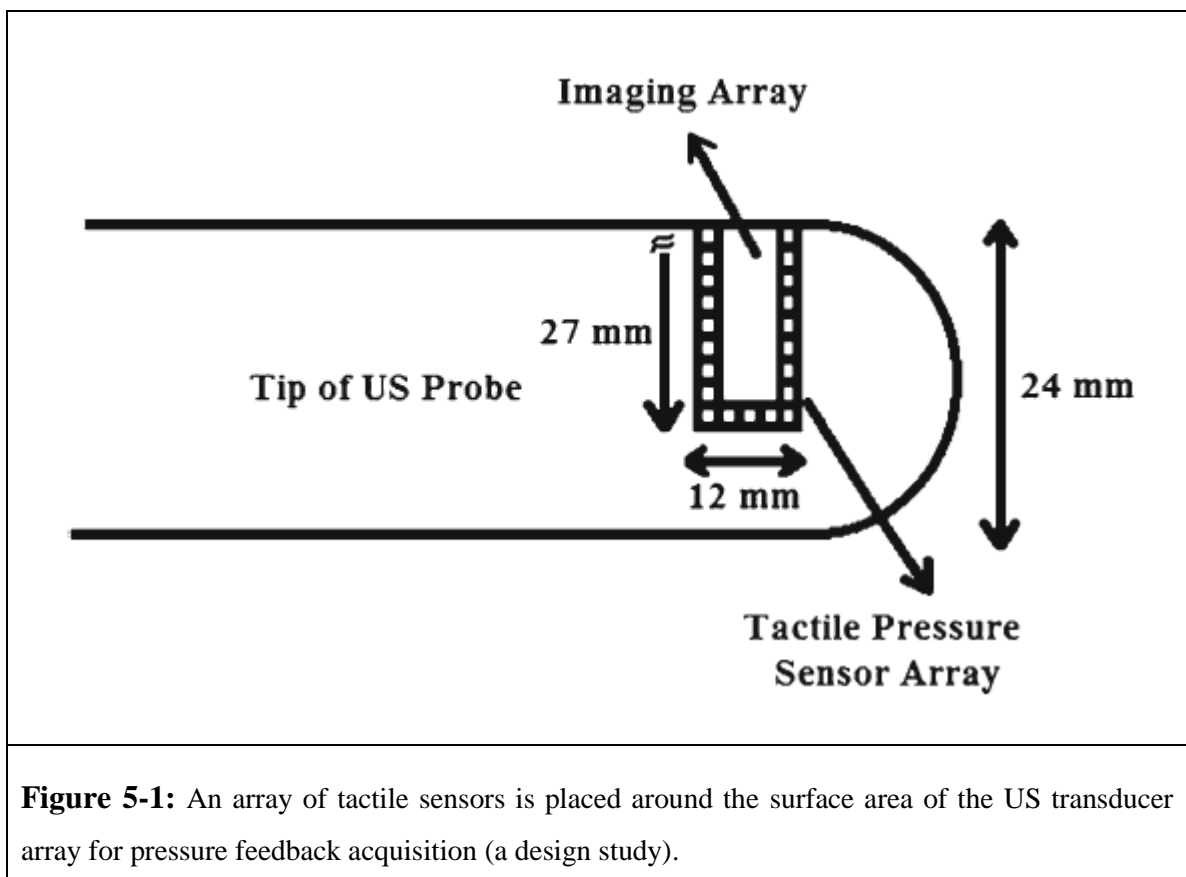
following a distribution map determined by a medical physicist in order to deliver sufficient radiation dose necessary to destroy cancerous cells throughout the prostate gland. To avoid deviation from the planned seed location map, it is necessary to minimize intra-operative prostate tissue deformation relative to the prostate at the preoperative image data acquisition stage. Registration is necessary in these applications because placing and moving the TRUS probe during image data acquisition may cause very significant prostate tissue motion and deformation, leading to significant rigid and deformable misalignment between the preoperative images and intra-operative 2DTRUS images. Based on solid mechanics, with tissue mechanical property parameters (e.g. Young's modulus) known for prostate tissues, significant prostate tissue deformation occurs as a result of applying contact pressure by the probe. Analytical and computational models including our model show a direct correlation between pressure applied by US probe and resulting prostate tissue deformation. It is noteworthy that the TRUS probe compression amount in clinical prostate imaging applications is within a range that leads to small tissue elastic deformation which ensures a linear elasticity, implying a linear relationship between applied pressure and prostate deformation.

Robotic systems allow physician to have control over the orientation of the probe during image acquisition. Thus, one approach is conducting 3D and 2D image acquisition with the probe fixed in a pre-determined position relative to the prostate as an attempt to circumvent image registration necessity at least partially. However, because of unexpected patient motion, the ultrasound probe position relative to the prostate is not fixed during image acquisition. The difference in the relative probe position implies that the prostate is deformed differently, and hence, deformable registration becomes necessary. This registration can be circumvented or at least sped up if the probe is steered such that its orientation relative to the prostate is almost the same during preoperative 3D and intra-operative 2D images acquisition. Positioning the ultrasound probe in similar orientations is not possible by means of image visual feedback only. Visual feedback only guarantees that the whole prostate is within the image's field of view irrespective of the probe's orientation. To ensure having the same orientation, pressure haptic feedback would be helpful. In this study, the application of tactile sensors in robot-assisted TRUS-

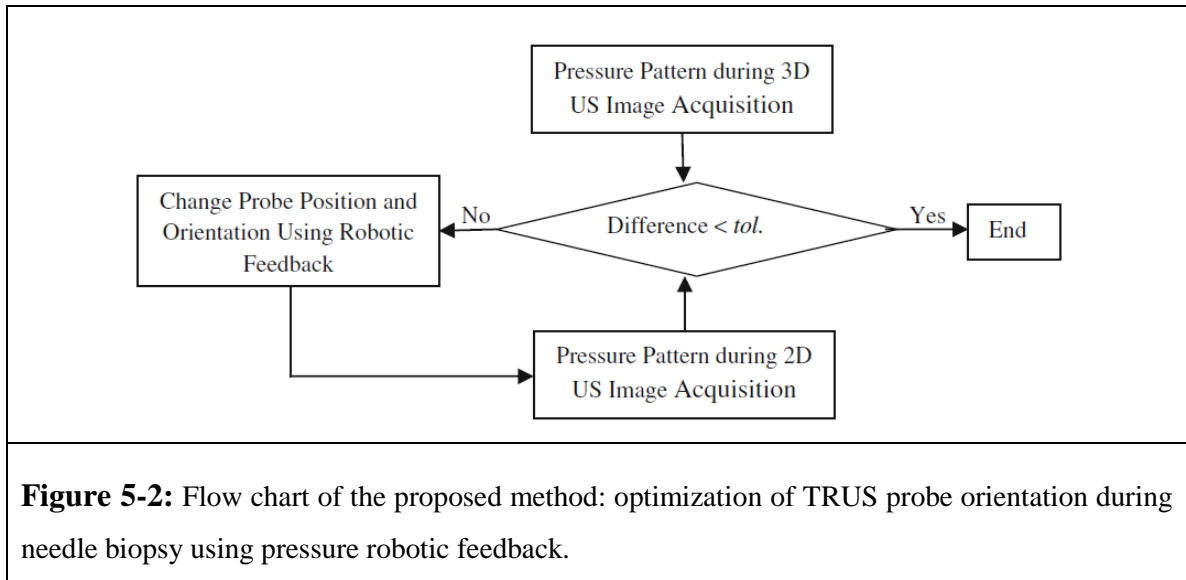
guided prostate biopsy system is investigated. In the next section, we will explain our proposed method, and in the following section, the experimental results will be presented.

5.2 Methods

Pressure feedback can be acquired by mounting a tactile sensor array around the surface area of the imaging array of the ultrasound probe as shown in Figure 5.1. The probe's diameter is 24 mm while the tactile sensor array is in fact a 1D array wrapped around the surface area of the imaging array of $25 \times 10 \text{ mm}^2$. The tactile sensor array consists of 74 ($1 \text{ mm} \times 1 \text{ mm}$) pressure sensors.



The pressure feedback provided by the sensor can provide information about the probe's orientation with respect to the prostate while indicating the extent of the prostate compression. Using the pressure feedback, the robotic system positions the probe such that the pressure pattern of the sensors during 2D image acquisition is similar to the pressure pattern during 3D image acquisition. Figure 5.2 shows a flow chart of the proposed method.



The proposed technique was validated with an *in silico* phantom study. The study contains three stages: defining a model mimicking prostate TRUS imaging, extracting pressure patterns from the model, and finally, applying the optimization algorithm.

5.2.1 Modeling

In order to simulate TRUS imaging, finite element modeling (FEM) can be used which requires the geometry, biomechanical properties of the tissue and boundary conditions. Analyzing this model using FE analysis provides the pressure pattern resulting from contact between the TRUS probe and rectal wall. Our model is a tissue block of size 160 mm × 120 mm × 100 mm containing a hollow cylinder mimicking the rectum. The prostate is located inside the block close to the rectal wall. Rectal wall (interior sphincter) tissue and a thin layer of fatty tissue lie between the probe and the prostate. The prostate position relative to the rectum in the FE model was determined based on MRI data shown in Figure 5.3a. A rigid probe-shaped part is also located inside the hollow cylinder. The diameter of the probe is 24 mm. To delineate the shape of the prostate, a 3D prostate MR image was segmented. For this purpose, the prostate border was delineated from 12 radial slices of the prostate as shown in Figure 5.3a. This was followed by fitting a surface to these borders to obtain the prostate surface (Figure 5.3b). This surface was then input into 3D Slicer software package [15] to obtain a cloud of points suitable for FE mesh generation (Figure 5.3c).

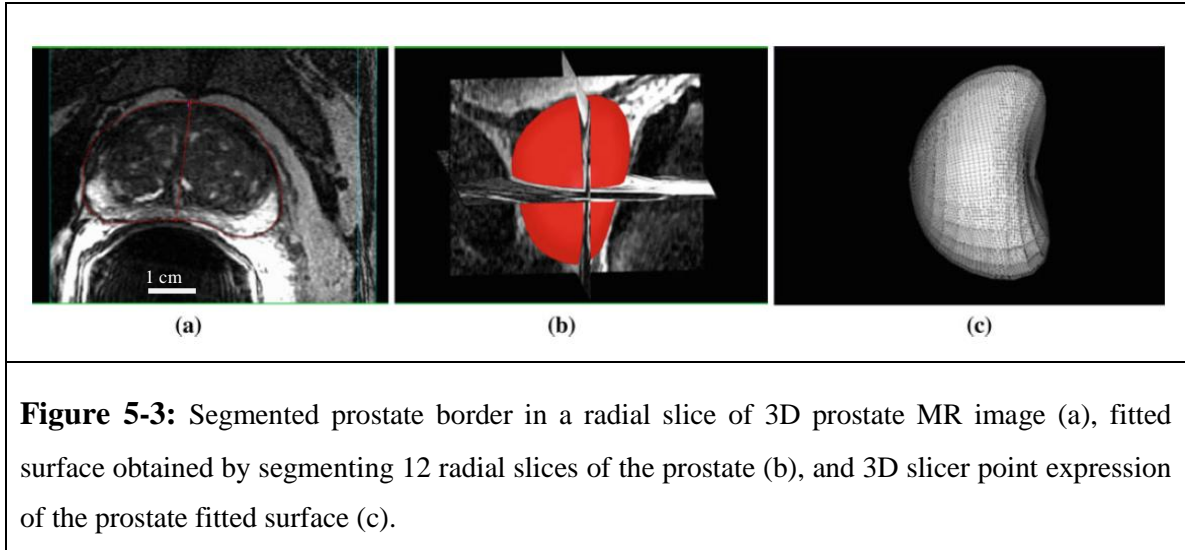


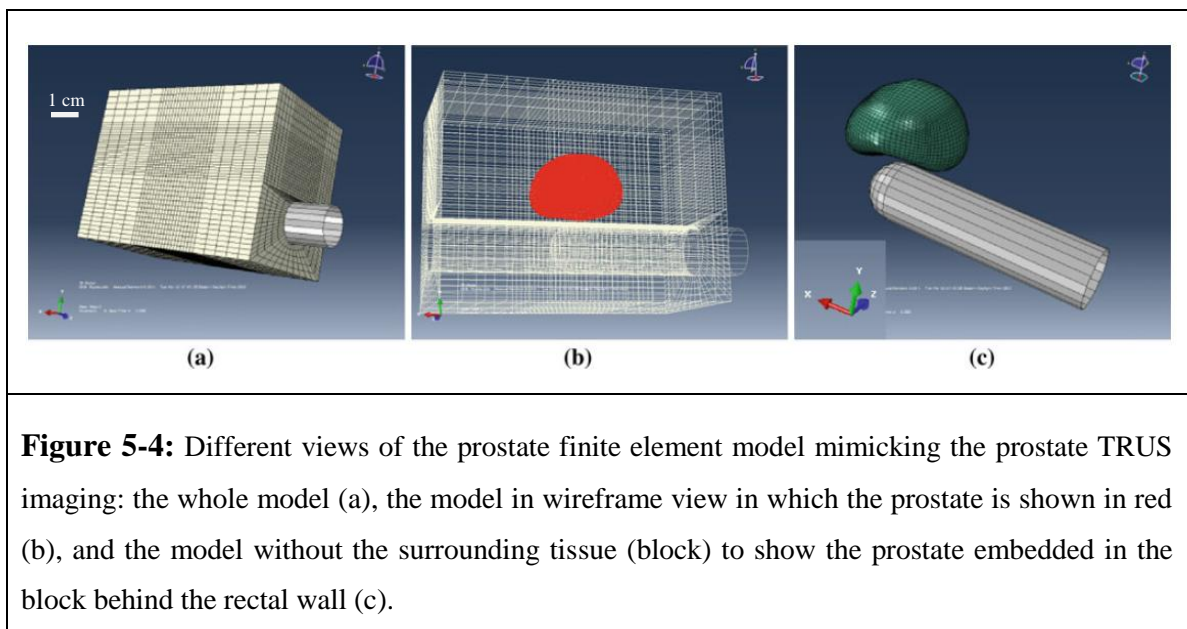
Figure 5-3: Segmented prostate border in a radial slice of 3D prostate MR image (a), fitted surface obtained by segmenting 12 radial slices of the prostate (b), and 3D slicer point expression of the prostate fitted surface (c).

After obtaining the FE mesh of each part including the prostate, the whole model was assembled into a FE mesh required for finite element analysis. The model depicted in Figure 5.4 shows different views of the model after meshing. It contains 33,000 elements with variable element size depending on anticipated stress concentration. Smaller elements were employed near the loading area in order to capture expected higher displacements gradients accurately in that area where high stress concentration is anticipated. Larger elements were employed to mesh tissue volumes far from the loading area as small displacement variations are expected. Largest element size is $11.4\text{mm} \times 5.4\text{mm} \times 5\text{mm}$ while the smallest element size is $2.85\text{ mm} \times 0.78\text{ mm} \times 2.65\text{ mm}$. All nodes of the model are free to move except the nodes on the top side of the box. This side contains fixed points which mimic the pubic bone.

5.2.2 Pressure Pattern Extraction

The pressure pattern arises from contact between the probe and the rectal wall attached to the prostate. Hence, the problem is modeled as a contact problem simulated using FEM. The size of the block is chosen such that the effect of probe insertion is insignificant near the outer surfaces of the block. Young's modulus values of 65 and 50 kPa were assigned to the prostate and its surrounding tissue, respectively [16]. The tip of the probe is considered as the origin of the coordinate system. The probe is considered to be free to move along X , Y , and Z axes (dx , dy and dz) while it is also unconstrained to rotate around all of these axes ($d\theta_x$, $d\theta_y$, $d\theta_z$) based on the coordinate system shown on the left

bottom corner of Fig. 5.4c. The model was then analyzed using ABAQUS commercial FE software package (Dassault Systèmes Simulia Corp, USA). Figure 5.5a shows the pressure on the rectal wall as a result of probe stimulation. This pressure is the normal component of the contact stress of the probe with the rectal wall. The pressure pattern over the contact area including the pressure sensor array elements is enlarged for better view. This area consists of 27×12 elements to be consistent with the sensor array pattern. The pressure values of 74 elements in contact with the pressure sensor array on the probe (Figure 5.5b) are concatenated to form the simulated tactile array pressure pattern that is used in the optimization stage.



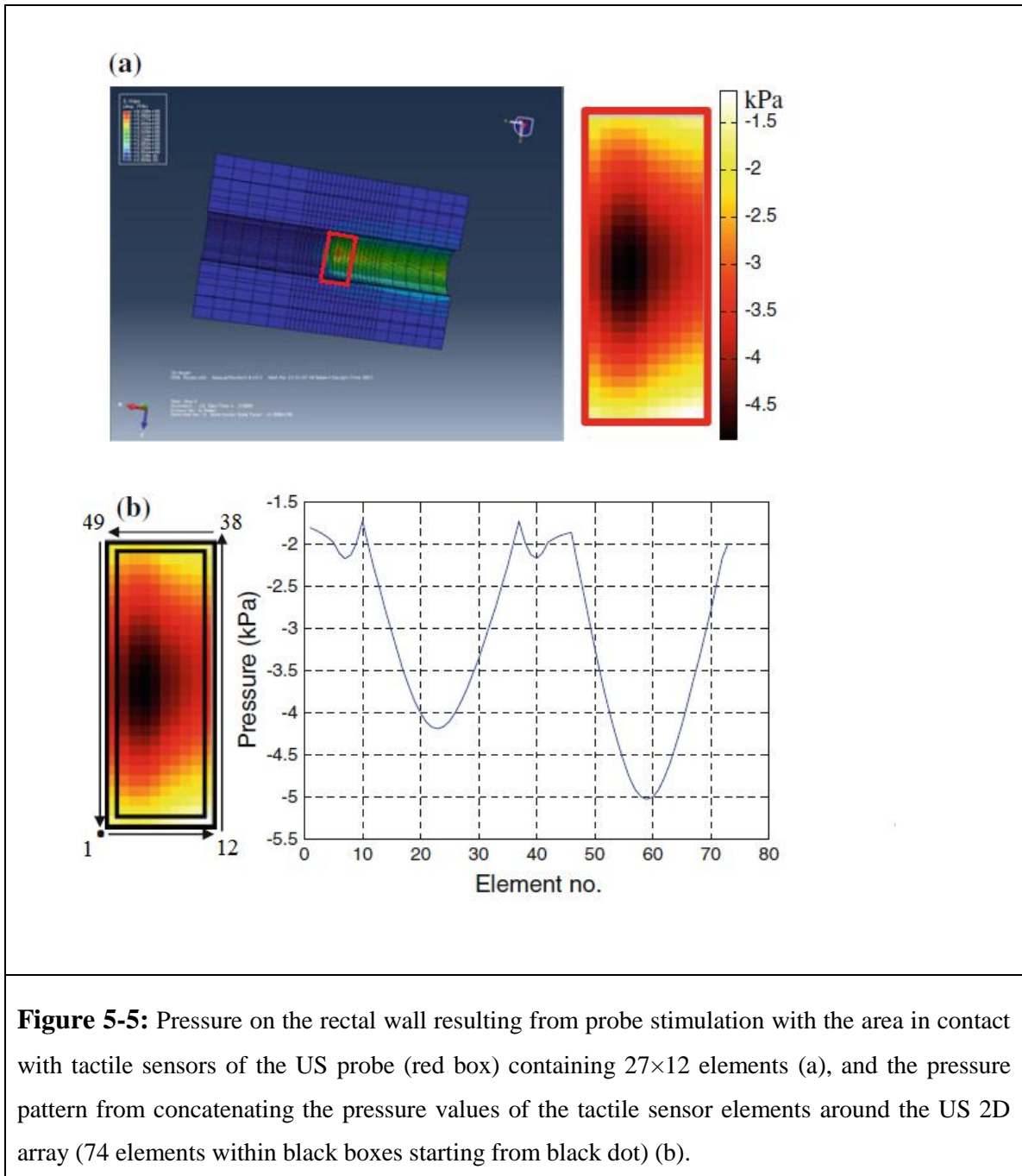


Figure 5-5: Pressure on the rectal wall resulting from probe stimulation with the area in contact with tactile sensors of the US probe (red box) containing 27×12 elements (a), and the pressure pattern from concatenating the pressure values of the tactile sensor elements around the US 2D array (74 elements within black boxes starting from black dot) (b).

5.2.3 Optimization

Having a pressure pattern P_{3D} obtained from 3D image acquisition and acquiring pressure pattern P_{2D} corresponding to a probe position during 2D image acquisition, the proper probe position for 2D image acquisition can be found by minimizing the following cost function:

$$Cost\ Function = \sum_{i=1}^{74} (P_i^{3D} - P_i^{2D})^2 \quad (5.1)$$

where P_i^{3D} is the pressure sensed by element i of the sensor array in the 3D imaging session and P_i^{2D} is the pressure sensed by element i of the sensor array in the 2D imaging session. Hence, the optimum probe orientation can be computed as follows:

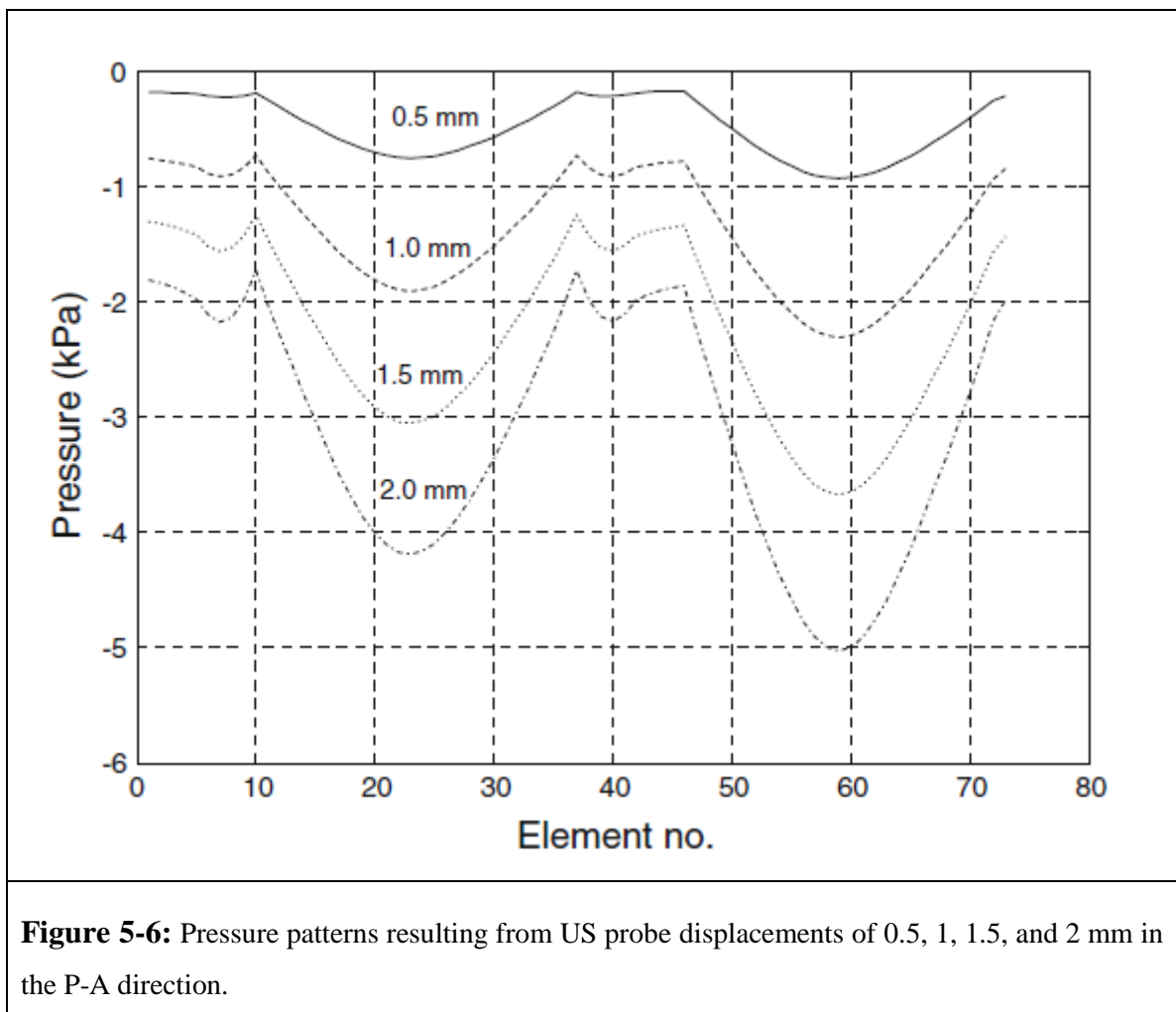
$$Optimum\ Probe\ Orientation = \arg\ min_{dx, dy, dz, d\theta_x, d\theta_y, d\theta_z} \sum_{i=1}^{74} (P_i^{3D} - P_i^{2D})^2 \quad (5.2)$$

The iterative Nelder-Mead Simplex optimization method was used in this study. This method is commonly used for nonlinear optimization problems. It is suitable for multidimensional unconstrained optimization where cost function does not include derivatives [17]. It is also widely used to solve parameter estimation problems where the function values are associated with uncertainties or they are subject to noise. The method is implemented in MATLAB where a function is available which is called *fminsearch*. This function performs a fully automated search to determine the optimal point. It is noteworthy that this function was utilized to provide a proof of principle of the proposed concept. More efficient optimization algorithms can be used that require fewer iterations and less computation overhead in developing a system prototype.

5.3 Results

In order to evaluate the proposed method, first, a sensitivity analysis of the pressure measurements to probe displacement was conducted. In other words, it was determined how much the pressure pattern changes as the probe is moved in small increments. For this purpose, the probe was pressed toward the prostate incrementally with 0.5 mm increments. The pressure pattern of each case was then recorded. Figure 5.6 indicates the pressure patterns of each case. As pressure sensors with 0.1 psi (~0.6 kPa) sensitivity are commercially available [18], this analysis shows that the system can detect displacements of 0.5 mm. After conducting this analysis, a test was conducted to determine whether the system can find the probe's original position while there is no relative body motion between the two imaging sessions. Hence, in one experiment, the probe was placed at the

origin and was allowed to move in the P-A direction for 3 mm ($dy = 3\text{ mm}$). The pressure pattern on the rectal wall was extracted for this case. Then, starting from an arbitrary probe position of ($dx = 1\text{ mm}$, $dy = 0\text{ mm}$, $dz = 0\text{ mm}$, $d\theta_x = 0\text{ rad}$, $d\theta_y = 0\text{ rad}$ and $d\theta_z = 0.05\text{ rad}$), the optimization algorithm was applied, which led to the exact location corresponding to $dy = 3\text{ mm}$. For different initial positions, the system converged to the same optimal probe position. More experiments with more probe displacement combinations were also conducted, which again led to the probe position and orientation accurately.



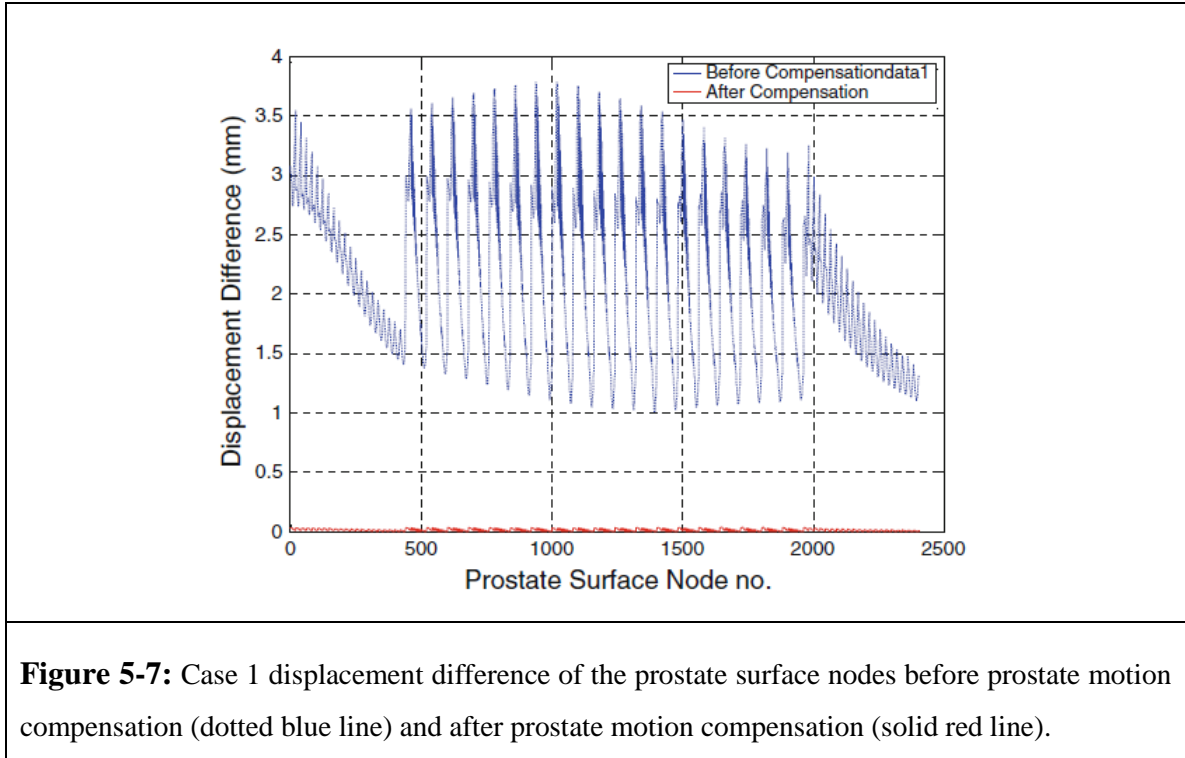
A second set of simulation experiment of more realistic cases, where body motion was considered, was conducted. In these experiments, it was assumed that probe insertion and body motion are the most significant factors influencing the prostate deformation. These

experiments include both translational and rotational patient movement. In these experiments, the probe was first placed at a given position corresponding to the first imaging session and the pressure pattern was recorded. In this case, the optimization algorithm was used while the phantom rigidly moved to simulate relative body motion in the second imaging session. Hence, the probe's position parameters were systematically changed until optimal parameters were found. In case 1, the phantom was rigidly moved 5 mm along y direction. Starting from different initial positions, the system converged approximately to the same optimal probe position. Results of two different initializations are summarized in Table 5.1.

To validate the method more quantitatively, prostate deformations before and after motion compensation were compared to each other. For this purpose, displacements of the prostate surface nodes of each case were compared to each other. Figure 5.7 shows the results of this comparison.

Table 5-1: Results of the proposed method for case 1 of the second experiments set where the phantom was moved 5mm along y direction.

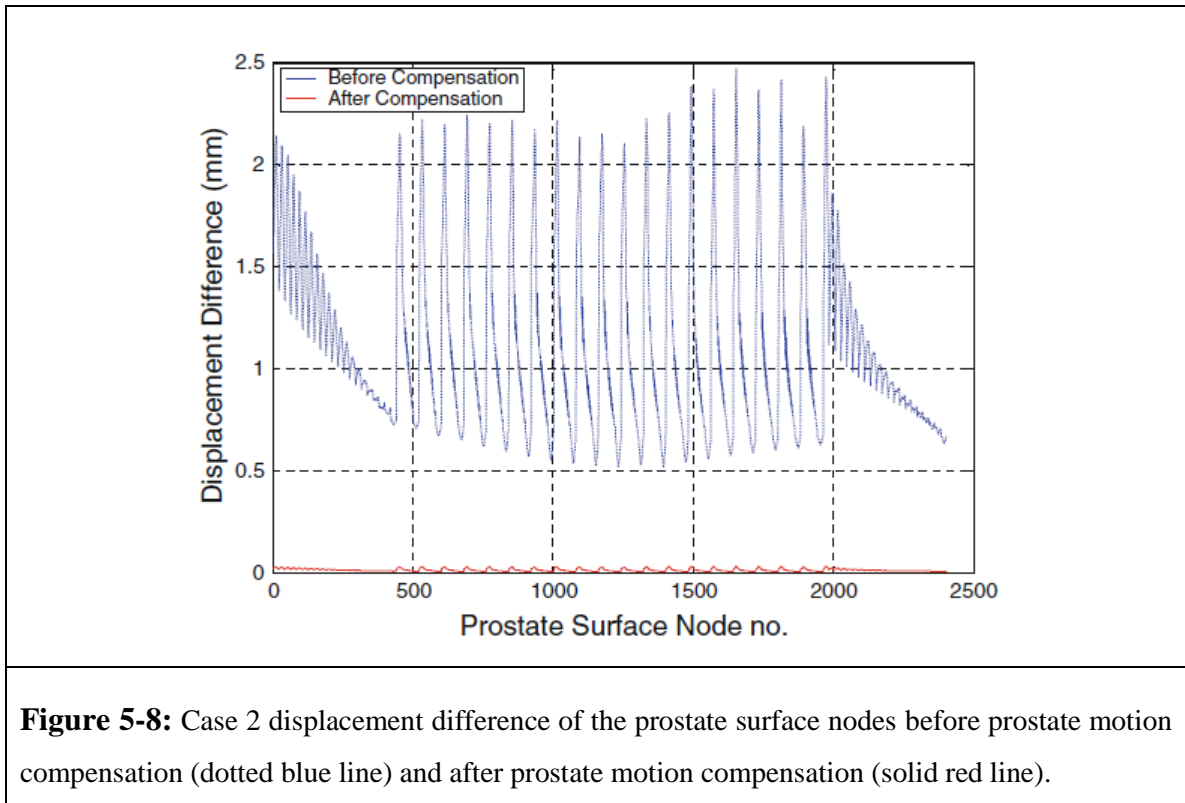
Case		dx (mm)	dy (mm)	dz (mm)	dθx (rad)	dθy (rad)	dθz (rad)	# of iterations
1	The Original Probe Position	0	1	0	0	0	0	
	Body Displacement	0	-5	0	0	0	0	
	First Initial Guess for the Probe Position	0	1	0	0	0	0	113
	Optimized Probe Position for the New Body Position	0	-3.97	0.02	-0.004	0.001	0.003	
	Second Initial Guess for the Probe Position	1	2	1	0	0.01	0	124
	Optimized Probe Position for the New Body Position	-0.02	-4.04	0.01	0.003	0	-0.008	



In case 2, the numerical phantom was rigidly moved 5 mm along z direction. Results of two different initializations are summarized in Table 5.2. Figure 5.8 shows results of displacement difference between states of pre- and post-motion compensation.

Table 5-2: Results of the proposed method for case 2 of the second experiments set where the phantom was moved 5 mm along z direction.

Case		dx (mm)	dy (mm)	dz (mm)	dθx (rad)	dθy (rad)	dθz (rad)	# of iterations
2	The Original Probe Position	0	1	0	0	0	0	
	Body Displacement	0	0	5	0	0	0	
	First Initial Guess for the Probe Position	0	1	0	0	0	0	136
	Optimized Probe Position for the New Body Position	0.03	1.02	4.89	-0.005	0.001	0	
	Second Initial Guess for the Probe Position	2	-3	-1	-0.02	0	0	108
	Optimized Probe Position for the New Body Position	-0.01	1.04	5.07	0.003	0.002	-0.006	



In case 3, the phantom was rigidly rotated 5° around the x axis. Results of two different initializations are summarized in Table 5.3. Also, Fig. 5.9 shows the results of displacement difference between the two states of pre- and post-motion compensation.

Table 5-3: Results of the proposed method for case 3 of the second experiments set where the phantom was rotated 5° around the x axis.

Case		dx (mm)	dy (mm)	dz (mm)	dθx (rad)	dθy (rad)	dθz (rad)	# of iterations
3	The Original Probe Position	0	1	0	0	0	0	
	Body Displacement	0	0	0	0.087	0	0	
	First Initial Guess for the Probe Position	0	1	0	0	0	0	127
	Optimized Probe Position for the New Body Position	0.02	0.98	0.11	0.092	-0.002	0	
	Second Initial Guess for the Probe Position	1	1	1	0.1	0.1	0.1	149
	Optimized Probe Position for the New Body Position	-0.01	1.01	0.08	0.084	0.005	-0.001	

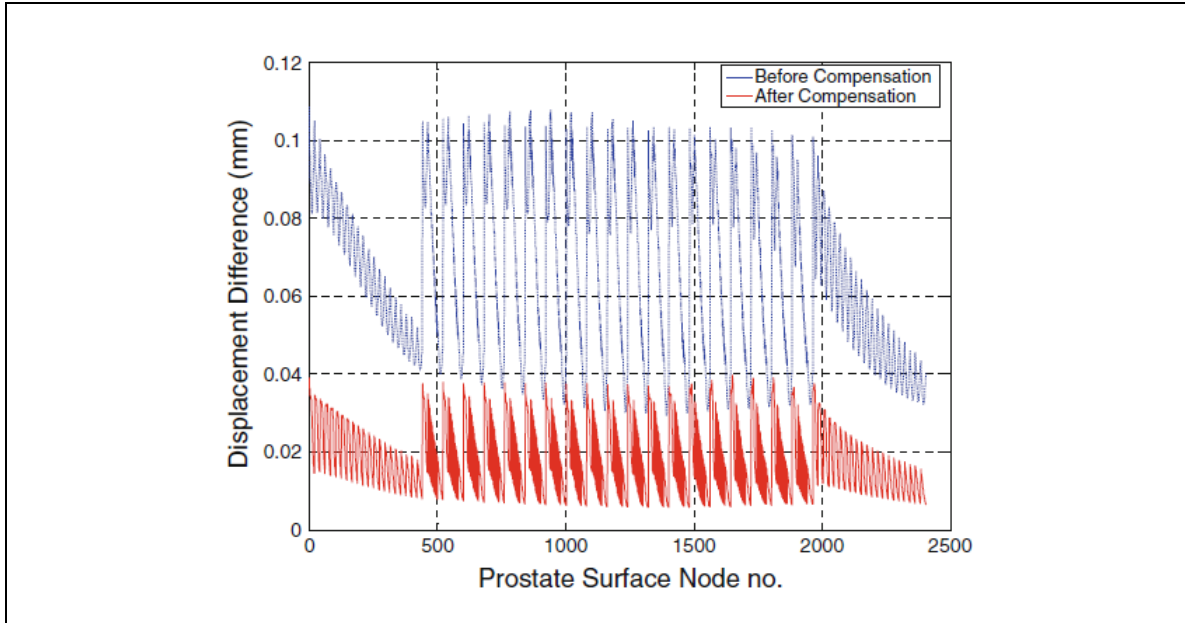
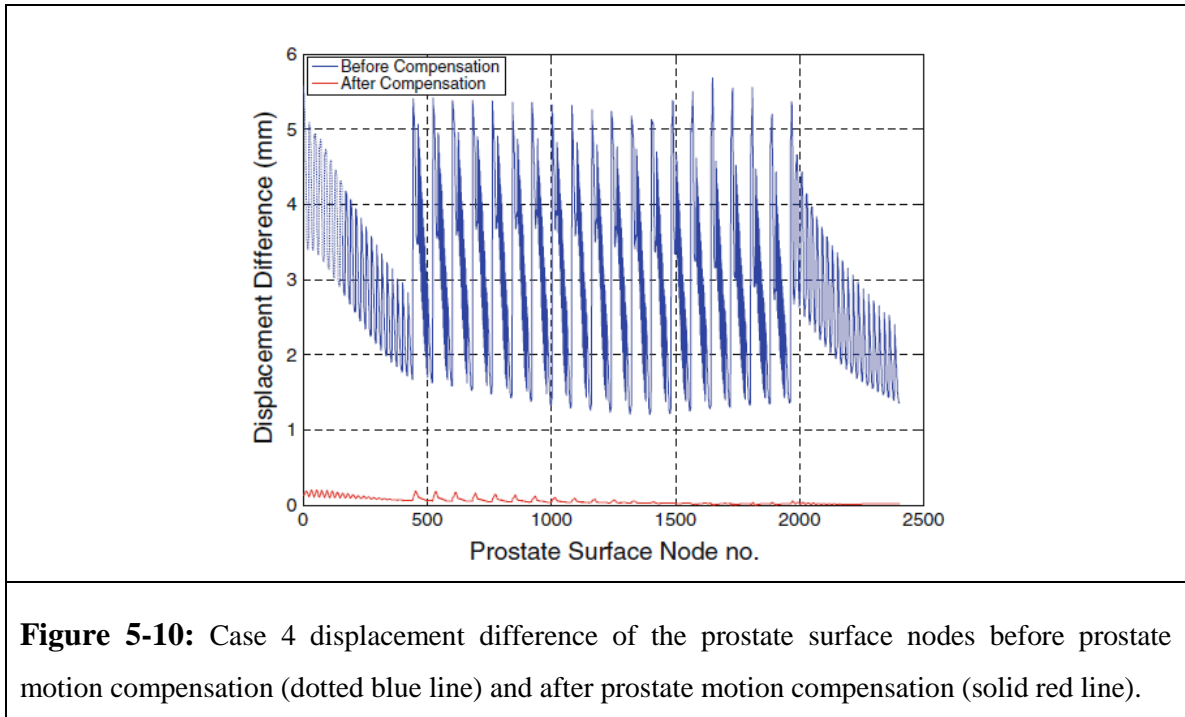


Figure 5-9: Case 3 displacement difference of the prostate surface nodes before prostate motion compensation (dotted blue line) and after prostate motion compensation (solid red line).

A more complex body movement was tested in case 4 where the phantom motion consisted of 5 mm along the y and z directions and a rotation of 5° around the x axis. Results of two different initiations are given in Table 5.4 while Figure 5.10 shows displacement difference between the states of pre- and post-motion compensation. This figure shows remarkable reduction in the prostate deformation discrepancy with using the pressure feedback system.

Table 5-4: Results of the proposed method for case 4 of the second experiments where the phantom was moved 5mm along both the y and z directions and rotated 5° around the x axis.

Case		dx (mm)	dy (mm)	dz (mm)	dθx (rad)	dθy (rad)	dθz (rad)	# of iterations
4	The Original Probe Position	0	1	0	0	0	0	
	Body Displacement	0	-5	-5	-0.087	0	0	
	First Initial Guess for the Probe Position	0	1	0	0	0	0	151
	Optimized Probe Position for the New Body Position	-0.04	-4.05	-4.91	-0.079	0.003	0.001	
	Second Initial Guess for the Probe Position	0	-1	-3	0.1	-0.1	0.1	129
	Optimized Probe Position for the New Body Position	0.02	-4.01	-4.93	-0.080	-0.002	0.007	



5.4 Discussion and Conclusions

In this work, we presented a method for optimizing the orientation of ultrasound (US) probe during prostate needle biopsy using pressure feedback. The algorithm uses the Nelder-Mead Simplex method for optimization. The fact that starting from an arbitrary probe position, the original orientation of the probe can be reached using this optimization method shows that this optimization method is suitable for this problem. Also, based on the results, the optimization algorithm drives the US probe such that the prostate motion and deformation are compensated for. The computational study presented in this work shows a very good potential of using the proposed algorithm in combination with a robotic system to alleviate the necessity of deformable image registration between intra-operative 2D ultrasound images and high quality 3D ultrasound images of the prostate, leading to more accurate prostate biopsy. Incorporating pressure feedback as described in the proposed technique can also be applied in combination with prostate intra-operative US images to ensure more effective MRI/US data fusion in the technique proposed by Hadaschik et al. [11] to achieve more accurate prostate biopsy outcome. In the numerical experiments conducted in this investigation, it was assumed that probe

insertion and body motion are the most significant factors influencing the prostate deformation. Prostate deformation due to other factors such as prostate and bowel movement, pelvic muscle construction, and bladder filling were assumed to have second-order effects compared to probe insertion. The other factor that may change the prostate position relative to the rectum and deform it significantly is the gravity. The gravity may cause significant prostate motion relative to the rectum if the patient's body rotates significantly. Significant body rotation between positions during 3D and 2D TRUS image acquisition, however, is expected to be small, leading to only insignificant prostate motion relative to the rectum.

There are multiple methods for 3DUS acquisition, including using different TRUS probe (2D probe versus real-time 3D probe), and also using location (left–right) or pulling (backward–forward) of a 2D US probe for scanning the 3D data. In this work, it was assumed that TRUS probe with similar geometry is used at the time of both intra-operative 2D TRUS and pre-operative 3D US image acquisition. As such, the proposed technique is limited to this scenario. It is noteworthy that relative tissue deformation due to using a different type of TRUS probe can be modeled and compensated for efficiently using the prostate FE model. In the presented phantom study the anatomy was idealized using approximate geometries. For example, the rectum was idealized as a cylinder while the surrounding tissue was idealized as a rectangular block.

Marks et al. [19] presented a review of image guided prostate biopsy systems that utilize, among other modalities, MRI-US image data fusion. In general, these systems have shown very good potential of improved cancer detection. These systems involve rigid and deformable image registration in order to facilitate image data fusion. Among them, the Urostation (Koelis, Grenoble, France) system utilizes real-time TRUS to TRUS image registration while efforts are under way to equip the Artemis (Eigen, Grass Valley, CA) with rigid and deformable image registration software necessary for fast and accurate registration necessary for image data fusion. Image registration algorithms involved in the latter are challenging as accurate deformable image registration algorithms are time-consuming. In other words, there is always a trade-off between accuracy and computation time. As suggested earlier, our proposed concept of ensuring

the application of similar probe contact pressure to the prostate maybe incorporated in these systems to minimize the necessity for image registration or at least to justify using less time demanding image registration algorithms consistent with small deformation prior to data fusion.

A major issue that has prevented broad tactile technology utility in medical robotic systems is the cost associated with pressure feedback. This study demonstrates clear benefit of such a system which justifies the cost of incorporating pressure feedback system in medical robots. The next stage of this project will involve constructing the proposed US probe with pressure sensors and incorporate it into a medical robotic system. This will pave the way for testing the proposed method first with tissue mimicking phantoms followed by in vivo study.

References

- [1] Canadian Cancer Society, Prostate Cancer Statistics: www.cancer.ca. Accessed 10 January 2013.
- [2] G. Salomon, J. Kollerman, I. Thederan, F. K. H. Chun, L. Budaus, T. Schlomm, H. Isbarn, H. Heinzer, H. Huland and M. Graefen, "Evaluation of prostate cancer detection with ultrasound real-time elastography: a comparison with step section pathological analysis after radical prostatectomy," *J Eur Urol*, vol. 54, pp.1354-1362, 2008.
- [3] Y. C. Fung, *Biomechanical properties of living tissue*, Springer, New York, 1981.
- [4] W. A. D. Anderson, *Pathology*, C. V. Mosby Co., St. Louis, 1953.
- [5] N. Miyanaga, H. Akaza, M. Yamakawa, T. Oikawa, N. Sekido, S. Hinotsu, K. Kawai, T. Shimazui and T. Shiina, "Tissue elasticity imaging for diagnosis of prostate cancer: a preliminary report," *J Urol*, vol. 13, no.12, pp.1514-1518, 2006.
- [6] L. Pallwein, M. Mitterberger, J. Gradl, F. Aigner, W. Horninger, H. Strasser, G. Bartsch, D. Zur Nedden and F. Frauscher, "Value of contrast-enhanced ultrasound and elastography in imaging of prostate cancer," *Curr Opin Urol*, vol. 17, no.1, pp. 39-47, 2007.
- [7] Y. Zhang, J. Tang, Y. Li, X. Fei, E. He, Q. Li and H. Shi, "The contribution of strain patterns in characterization of prostate peripheral zone lesions at transrectal ultrasonography," *Acta Radiologica*, vol. 53, no. 1, pp.119-126, 2012.
- [8] J. C. Presti, "Prostate cancer: assessment of risk using digital rectal examination,

- tumor grade, prostate-specific antigen, and systematic biopsy,” *Radiologic Clin North Am*, vol. 38, no.1, pp. 49-58, 2000.
- [9] T. Loch, “Urologic imaging for localized prostate cancer in 2007,” *World J Urol*, vol. 25, pp.121-129, 2007.
- [10] S. Song, N. B. Cho, I. I. Iordachita, P. Guion, G. Fichtinger and L. L. Whitcomb, “A study of needle image article localization in confirmation imaging of MRI-guided robotic prostate biopsy,” *IEEE international conference on robotics and automation*, 2011.
- [11] A. Boris, B. A. Hadaschik, T. H. Kuru, C. Tulea, P. Rieker, I. V. Popeneciu, T. Simpfendörfer, J. Huber, P. Zogal, D. Teber, S. Pahernik, M. Roethke, P. Zamecnik, W. Roth, G. Sakas, H. P. Schlemmer ad M. A. Hohenfellner, “Novel stereotactic prostate biopsy system integrating pre-interventional magnetic resonance imaging and live ultrasound fusion,” *JURO*, vol. 186, no. 6, pp. 2214-2220, 2011.
- [12] T. De Silva, J. Bax, A. Fenster, J. Samarabandu and A. D. Ward, “Quantification of prostate deformation due to needle insertion during TRUS-guided biopsy: comparison of hand-held and mechanically stabilized systems,” *SPIE Proceedings*, 2011.
- [13] C. Reynier, J. Troccaz, P. Fournieret, A. Dusserre, C. Gay-Jeune, J. Descotes, M. Bolla and J. Giraud, “MRI/TRUS data fusion for prostate brachytherapy. Preliminary results,” *Med Phys*, vol. 31, pp.1568-1575, 2004.
- [14] Z. Wei, G. Wan, L. Gardi, G. Mills, D. Downey and A. Fenster, “Robot-assisted 3D-TRUS guided prostate brachytherapy: system integration and validation,” *Med Phys*, vol. 31, no. 3, pp.539-548, 2004.
- [15] S. Pieper, M. Halle and R. Kikinis, “3D SLICER,” *Proceedings of the 1st IEEE international symposium on biomedical imaging: from nano to Macro*, pp 632-635, 2004.
- [16] T. A. Krouskop, T. M. Wheeler, F. Kallel, B. S. Garra and T. Hall, “Elastic moduli of breast and prostate tissues under compression,” *Ultrason Imaging*, vol. 20, no.4, pp.260-274, 1998.
- [17] J. A. Nelder and R. Mead, “A simplex method for function minimization,” *Comput J*, vol. 7, pp. 308–313, 1965.
- [18] Pressure Profiles Systems, Inc. Tactile Sensor Imaging Solutions in Medical Devices. www.pressureprofile.com/index-medical.php. Accessed 10 Jan 2013.
- [19] L. Marks, S. Young and S. Natarajan, “MRI-ultrasound fusion for guidance of targeted prostate biopsy,” *Curr Opin Urol*, vol. 23, no. 1, pp. 43–50, 2013.

Chapter 6

Conclusions and Future Work

6.1 Conclusions

In this investigation, two ultrasound elastography methods were introduced and thoroughly investigated for prostate cancer early detection and specification. These techniques are based on the premise that tissue stiffness changes as a result of cancer. This research also included a preliminary study of the concept of using a pressure feedback system for improving the current clinical 3D ultrasound guided prostate needle biopsy. Application of the concept relies on the assumption that prostate tissue pressure profiles collected from the surface of the rectum is a representative of prostate deformation. As described in Chapter 1, the motivation behind these studies was to develop clinically acceptable techniques that can be used as simple add-ons easily incorporated into the current available prostate cancer assessment systems without introducing significant expenses and excessive inconveniency for the patient. These proposed techniques utilize tissue biomechanics principles to provide valuable information that can be used solely or in combinations of other clinical data within a multi-parametric imaging system, leading to improved accuracy of prostate cancer detection through imaging or image guided needle biopsy. The investigations conducted in this research were presented in four chapters. The main research contributions and results explained in each chapter are summarized below.

6.1.1 Chapter 2: A Fast Shape-Similarity-Based Ultrasound Elastography Technique for Prostate Cancer Diagnosis

In this chapter, a novel prostate elastography technique was presented. This technique requires only two sets of prostate TRUS B-mode images that are acquired under pre- and post-compression states. As such, the elastography system which incorporates this technique only requires a conventional US imaging scanner to conduct elasticity imaging, i.e. no additional hardware or software is required for tissue displacement data acquisition. The reconstruction technique used in the proposed method is a constrained technique as it assumes that each tissue type is homogenous throughout its volume. As such, it requires a priori knowledge about the geometry of the tumor and normal tissues, which means that the algorithm relies on tumor detection prior to elastography. While incapable of tumor detection, the proposed technique can separate malignant tumors from benign ones. An *in silico* phantom study including four prostate phantom cases with variable tumor locations and Young's modulus values was conducted. This was followed by a tissue mimicking phantom study which was conducted to further assess the merits of the proposed method. Results of these studies indicated that the proposed method can reconstruct the mechanical properties of the tumor, prostate and its surrounding tissue with a reasonable accuracy. The results also indicated that the method is robust as it is not significantly sensitive to segmentation errors, especially when a weighted cost function is used. In the weighted cost function, larger weight was assigned to the prostate capsule as it can be segmented relatively accurately in ultrasound images while a smaller weight was assigned to tumor boundary which is associated with higher segmentation uncertainty. The method was also accelerated with SFEM for near real-time elasticity reconstruction. Using SFEM did not introduce further significant errors to the reconstructed Young's modulus values while it accelerated the reconstruction process such that the computation speed was two orders of magnitude higher.

6.1.2 Chapter 3: Towards Clinical Prostate Ultrasound Elastography Using Full Inversion Approach

In this Chapter, a full inversion quasi-static US elastography technique was introduced. The method was structured based on a mathematical framework that takes into account

realistic boundary conditions and stress non-uniformity, leading to more reliable YM reconstruction. The proposed elastography technique only requires RF data acquired under two prostate states of pre-compression and TRUS induced post-compression. These data can be acquired using any clinical ultrasound imaging system which allows access to RF data while no additional hardware attachment is necessary. The quantitative elastography method proposed in this chapter is capable of tumor classification while it can be also used for tumor detection and localizations it does not require image segmentation. This feature of not requiring image segmentation is highly desirable, particularly with US elastography, as B-mode or strain images frequently lack enough sensitivity and SNR necessary for segmenting tumors and sometimes even the prostate capsule. The proposed prostate US elastography method was validated using *in silico* and unifocal and bifocal tissue mimicking phantom studies and the results indicated the reasonably high accuracy of the reconstructed YM ratios and its robustness to noise. It was also validated using a small patient study where patients involved in the study had prostatectomy after undergoing the US elastography procedure. Histopathology images of prostate slices indicated good agreement with the reconstructed Young's modulus images. The drawback of the developed reconstruction algorithm is that it is computationally complex, hence is not suitable for real-time applications unless parallel computing using GPU programming or accelerated FEM techniques is used.

6.1.3 Chapter 4: Statistical finite element method for real-time tissue mechanics analysis

In this chapter, SFEM which is a novel fast FE-based technique was proposed for estimating biological tissue deformation and stress under specified loading conditions. The technique utilized preprocessed data obtained by accurate FE analysis to develop effective interpolation functions to relate the organ geometry space to its corresponding FE solution including displacement and stress fields. Two different fitting functions, namely NN and PCA, were used in this study to develop the mapping functions between geometry and FE fields. Due to the large number of variables required to define the geometry and FE spaces, PCA was employed to reduce the feature dimensions by projecting both the geometry and FE spaces on their respective main bases. The proposed

technique was validated with an *in silico* phantom study. This study included four different analysis types, i.e. prescribed displacement boundary condition and contact problem in conjunction with linear elastic and hyperelastic materials. The results obtained for numerically generated 2D shapes proved that the method is both very fast and highly accurate for calculating both displacement and stress fields of prostate tissues. These encouraging results indicate the method's excellent potential for application in many biomedical applications. As an example, SFEM was used to accelerate the constrained elastography method proposed in chapter 2. The validated phantom study explained in that chapter confirmed the suitability of this method for computer-assisted diagnosis and intervention applications where real-time tissue deformation calculation is required.

6.1.4 Chapter 5: Towards ultrasound probe positioning optimization during prostate needle biopsy using pressure feedback

In this chapter, a method for optimizing the orientation of ultrasound probe during prostate needle biopsy was presented. The method utilizes a tissue pressure feedback system for this optimization. It is founded on the assumption that similar pressure patterns of the surface of an organ under similar loading conditions reflect similar tissue deformation. Hence, in the context of TRUS guided needle biopsy, the proposed system was driven by the pressure feedback as a function of the TRUS probe position such that the pressure pattern acquired using pressure sensors during 2D imaging is similar to its pressure pattern counterpart acquired during 3D TRUS imaging. In this work, it was assumed that TRUS probe with similar geometry is used at the time of both intra-operative 2D TRUS and pre-operative 3D US image acquisition. The pressure feedback required in the proposed technique can be acquired by mounting a 1D tactile sensor array wrapped around the imaging 2D array of the ultrasound probe. The method was validated with a computational study, and based on the obtained results, the probe position was optimized in such a way that the prostate motion and deformation were compensated. This computational study showed the potential of using the proposed algorithm in conjunction with a robotic system to alleviate the necessity of deformable image registration between intra-operative 2D ultrasound images and high quality 3D ultrasound images of the prostate, leading to more efficient and accurate prostate needle biopsy.

6.2 Future Directions

The constrained elastography method is capable of prostate tumor classification in real-time using SFEM. However, it requires that the tumor is clearly visible in the image. Although in some cases nodules appear as hypo-intensive regions in ultrasound images, such cases are rare as discussed in chapter 1. There is an ongoing project in our lab to apply the same concept with T2-weighted MR images where the objective is to increase the MR images specificity. It is noteworthy that prostate nodules are frequently more visible in T2-weighted images, hence, can be segmented more reliably. In this research project, mechanical stimulation is applied by inflating the prostate RF coil balloon. As the proposed method is capable of obtaining the prostate tissue elastic moduli *in vivo*, it can be used for applications where biomechanical simulation of the prostate is involved. To be reliable, such applications require reasonably accurate tissues' elastic moduli. Examples of such applications include virtual reality (VR) systems of prostate surgery and computer-aided prostate medical intervention.

As stated earlier, the unconstrained elastography technique proposed in this thesis has the potential for tumor detection and localization. As discussed in chapter 3, comparing the histopathology images with the reconstructed elasticity images indicates imperfect matches between tumor location and geometry in some cases. This lack of perfect matching can be attributed to factors which contribute to image artifacts through the image reconstruction process. It can also be attributed to the fact that the histopathology sections are deformed significantly compared to the corresponding *in vivo* prostate sections and that histopathology sections often do not exactly match the position and orientations of US scan sections. Assessing the capability of the proposed unconstrained elastography method for tumor localization requires accurate registration of ultrasound images to histopathology images.

A potential future work for continuing this research is to assess the method's sensitivity and specificity which requires a clinical study. To this end, a relatively number of clinical cases with different tumor size and location scenarios are required. An interesting future study that may follow sensitivity and specificity assessment can be

testing an important hypothesis of correlation between tumor stiffness and its level of invasiveness.

In this research, the SFEM method was used to accelerate the constrained elastography technique. Except elastography, this method can be implemented in applications such as VR environments used for surgery training, computer-assisted surgery and brachytherapy where real-time simulation is required. As discussed in chapter 4, the important feature of the method is that its speed does not depend on the complexity of the FE model used in the pre-processing procedure. However, the more nonlinearity involved in the FE analysis, the more complex the fitting function may have to be, which may influence its accuracy. An interesting future study can be applying the SFEM should on 3D models to test the complexity of the mapping functions and their accuracy. Another concern about the method is that in some cases, loading conditions are not fully known a priori. In such case, the final deformed shape can be obtained using the superposition principle which combines SFEM analysis results corresponding to a set of unit displacement or force boundary conditions. As a future work, these cases should be considered to have a more generalized mapping.

The pressure feedback system explained in chapter 5 was a preliminary study to prove the concept of using pressure feedback to improve the prostate needle biopsy outcome. In the numerical experiments conducted in this investigation, it was assumed that probe insertion and body motion are the most significant factors influencing the prostate deformation. Prostate deformation due to other factors such as prostate and bowel movement, pelvic muscle contraction, and bladder filling were assumed to have second-order effects compared to probe insertion. Further experiments should be done to test the effect of these factors. Optimizing the size and location of the pressure sensor based on the model is the other goal that can be pursued in the future.

6.3 Closing Remarks

Different types of imaging modalities can be used for prostate cancer assessment. These modalities would help for early detection of prostate cancer with higher accuracy, tumor localization and classification and consequently prostate cancer accurate diagnosis. So far, no sole single modality imaging has been developed which is capable of providing comprehensive data necessary for reliable prostate cancer assessment. Such assessment often requires data obtainable from other tests and imaging modalities. For clinical viability of a technique to be included in a multi-parametric framework, the technique needs to be inexpensive, convenient for patients and clinically acceptable. The methods proposed in this thesis for prostate cancer assessment are steps towards development of such techniques. They rely on technologies currently used in the clinic with the aim of improving prostate cancer diagnosis accuracy without introducing significant cost and inconvenience to patients. However, further investigations involving clinical studies are required for assessing the reliability and accuracy of the proposed techniques in clinical setting as suggested in this Chapter.

Appendices

Appendix 1: Permission to reproduce the papers, which has been published under AAMP copyright, in this thesis.



American Association of Physicists in Medicine

One Physics Ellipse
College Park, MD 20740-3846
(301) 209-3350
Fax (301) 209-0862
<http://www.aapm.org>

Office of the Executive Director

DATE OF REQUEST: 02/28/14

FROM:

Seyed Reza Mousavi
Department of Electrical and Computer Engineering, Western University, London, Ontario N6A 5B9, Canada

EMAIL ADDRESS: [REDACTED]

1. Permission is granted to:

Seyed Reza Mousavi

2. Permission is requested to use the following material:

Seyed Reza Mousavi, Ali Sadeghi-Naini, Gregory J. Czarnota and Abbas Samani, "Towards clinical prostate ultrasound elastography using full inversion approach." *Medical Physics* 41(3), 033501 (2014), <http://dx.doi.org/10.1118/1.4864476>.

3. For what purpose:

I am writing to get your permission for including this paper I authored and was published under AAPM copyright in *Medical Physics* as a chapter in my thesis. This thesis is to be submitted in partial fulfillment of the requirements for the degree of Doctor of Philosophy to The School of Graduate and Postdoctoral Studies, Western University

Authors seeking permission must also notify the first author of the article from which permission is being sought.

Permission is hereby granted:

[REDACTED]
Signature

March 7, 2014
Date

Appendix 2: Permission to reproduce the paper, which has been published under Taylor & Francis (AAPM) copyright, in this thesis.

Our Ref: LA/GCMB/P624

28 March 2014

Dear Seyed Reza Mousavi,

Thank you for your email requesting permission to reproduce the below article in your thesis entitled 'Biomechanical Modeling and Inverse Problem-based Elasticity Imaging for Prostate Cancer' to be published by Western University.

Material Requested: "Statistical finite element method for real-time tissue mechanics analysis" by Seyed Reza Mousavi, Iman Khalaji, Ali Sadeghi Naini, Kaamran Raahemifar, Abbas Samani, published in Computer Methods in Biomechanics and Biomedical Engineering, Vol15:6, 595-608(2012)

We will be pleased to grant entirely free permission on the condition that you acknowledge the original source of publication and insert a reference to the Journal's web site: <http://www.tandfonline.com>

We are happy for you to post the preprint version on the Western University website.

As you are the author of the above article, we will be pleased to grant entirely free permission on the condition that you make the following acknowledgement:

This is an electronic version of an article published in in Computer Methods in Biomechanics and Biomedical Engineering © 2012 Copyright Taylor & Francis; in Computer Methods in Biomechanics and Biomedical Engineering is available online at www.tandfonline.com [with the open URL of the article] <http://www.tandfonline.com/doi/full/10.1080/10255842.2010.550889#>

Thank you for your interest in our Journals.

Yours sincerely



Appendix 3: Permission to reproduce the paper, which has been published under Springer copyright, in this thesis.

**SPRINGER LICENSE
TERMS AND CONDITIONS**

Mar 11, 2014

This is a License Agreement between Seyed Reza Mousavi ("You") and Springer ("Springer") provided by Copyright Clearance Center ("CCC"). The license consists of your order details, the terms and conditions provided by Springer, and the payment terms and conditions.

All payments must be made in full to CCC. For payment instructions, please see information listed at the bottom of this form.

License Number	3326570306782
License date	Feb 12, 2014
Licensed content publisher	Springer
Licensed content publication	International Journal of Computer Assisted Radiology and Surgery
Licensed content title	Towards ultrasound probe positioning optimization during prostate needle biopsy using pressure feedback
Licensed content author	Seyed Reza Mousavi
Licensed content date	Jan 1, 2013
Volume number	8
Issue number	6
Type of Use	Thesis/Dissertation
Portion	Full text
Number of copies	1
Author of this Springer article	Yes and you are the sole author of the new work
Order reference number	
Title of your thesis / dissertation	Biomechanical Modeling and Inverse Problem-based Elasticity Imaging for Prostate Cancer Diagnosis
Expected completion date	Feb 2014
Estimated size(pages)	100
Total	0.00 CAD

Curriculum Vitae

Name	Seyed Reza Mousavi
Post-secondary Education and Degrees	<p>Western University London, Ontario, Canada 2010-2014, Ph.D., Electrical and Computer Engineering, Biomedical Systems</p> <p>Tehran University Tehran, Tehran, IRAN 2004-2006, M.Sc., Electrical and Computer Engineering, Bioelectric</p> <p>Sharif University of Technology Tehran, Tehran, IRAN 1999-2004, B.Sc., Electrical Engineering, Electronics</p>
Honors and Awards	<p><u>Research Awards:</u></p> <ul style="list-style-type: none"> ▪ SPIE best paper award finalist 2014 ▪ German Research Foundation (DFG) Scholarship 2013 ▪ Queen Elizabeth II Graduate Scholarship 2013 ▪ SPIE best paper award finalist 2013 ▪ SPIE Cum Laude Poster Award 2012 ▪ Graduate Thesis Research Award 2011
Related Work Experience	<p><u>Research Experiences</u></p> <ul style="list-style-type: none"> ▪ Graduate Research Assistant (GRA) 2010 - 2014 Biomedical Systems Group, Department of Electrical and Computer Engineering, The University of Western Ontario, London, Ontario, CANADA, January ▪ CAMI NSERC- CREATE Scholar 2011 - 2013 <p><u>Teaching Experiences</u></p> <ul style="list-style-type: none"> ▪ Graduate Teaching Assistant (GTA) Department of Electrical and Computer Engineering, Western University ▪ Introduction to Signal Processing 2013 ▪ Electric Circuits and Electro-mechanics 2012,2013 ▪ Introductory Engineering Design and Innovation Studio 2012 ▪ Programming Fundamentals 2010,2011

Publications

Selected Journal Papers

- **S. R. Mousavi**, A. Sadeghi Naini, G. Czarnota and A. Samani, "Towards Clinical Prostate Ultrasound Elastography Using Full Inversion Approach," *Journal of Medical Physics*; 41(3): 033501, 2014. **(featured article and cover of the issue)**
- **S. R. Mousavi**, K. Raahemifar, S. Pautler and A. Samani, "Towards ultrasound probe positioning optimization during prostate needle biopsy using pressure feedback," *Int J Comput Assist Radiol Surg.*; 8(6):1053-61, 2013.
- **S. R. Mousavi**, I. Khalaji , A. Sadeghi Naini, K. Raahemifar and A. Samani., "Statistical finite element method for real-time tissue mechanics analysis," *Comput Methods Biomech Biomed Engin.*;15(6):595-608, 2011.
- **S. R. Mousavi**, A. Fehlnr, K.J. Streitberger, J. Braun, A. Samani and I. Sack, "Measurement of in vivo cerebral volumetric strain induced by the Valsalva maneuver," In Press, *Journal of Biomechanics*; 47(7):1652-1657, 2014.

Selected Conference Papers

- **S. R. Mousavi** and A. Samani, "Prostate clinical study of a full inversion unconstrained ultrasound elastography technique," *SPIE Medical Imaging*, San Diego, USA, 2014 **(Podium)**
- **S. R. Mousavi** and A. Samani, "A full inversion unconstrained ultrasound elastography technique for prostate cancer assessment," *SPIE Medical Imaging*, Florida, USA, 2013 **(Podium)**
- **S. R. Mousavi** and A. Samani, "Novel real-time prostate ultrasound elastography technique: phantom study, " 26th International Congress and Exhibition on Computer Assisted Radiology and Surgery (CARS), Italy, 2012 **(Podium)**
- H. Wang, **S. R. Mousavi** and A. Samani, "A novel shape similarity based elastography system for prostate cancer assessment," *SPIE Medical Imaging*, San Diego, USA, 2012 **(Poster)**
- **S. R. Mousavi** and A. Samani, "Realtime Ultrasound Prostate Young's Modulus Reconstruction Using a Full Inversion Approach," *ASME International Mechanical Engineering Congress & Exposition*, Vancouver, 2010 **(Podium)**